# Detectors for the Atacama Cosmology Telescope

Tobias A. Marriage

A Dissertation
Presented to the Faculty
of Princeton University
in Candidacy for the Degree
of Doctor of Philosophy

Recommended for Acceptance
by the Department of
Physics

November, 2006

# Abstract

The Atacama Cosmology Telescope (ACT) will make measurements of the brightness temperature anisotropy in the Cosmic Microwave Background (CMB) on degree to arcminute angular scales. The ACT observing site is located 5200 m near the top of Cerro Toco in the Atacama Desert of northern Chile. This thesis presents research on the detectors which capture the image of the CMB formed at ACT's focal plane. In the first chapter, the primary brightness temperature fluctuations in the Cosmic Microwave Background are reviewed. In Chapter 2, a calculation shows how the CMB brightness is translated by ACT to an input power to the detectors. Chapter 3 describes the ACT detectors in detail and presents the response and sensitivity of the detectors to the input power computed in Chapter 2. Chapter 4 describes the detector fabrication at NASA Goddard Space Flight Center. Chapter 5 summarizes experiments which characterize the ACT detector performance.

# Acknowledgements

I am indebted to Princeton University and the Physics Department who have supported me throughout my graduate career. I am particularly grateful for the support that I received during my parents' illnesses. Among the faculty at the Physics Department I am closest to Lyman Page who has been my academic advisor since I arrived as an undergraduate in 1996. He and his family are like kin. Suzanne Staggs, who leads the ACT detector research, is a long time friend and advisor, and has always believed in my work. Norman Jarosik made the research in this thesis possible by designing and assembling the detector testbed. Norm is a fount of experimental know-how from whom I have learned much, most often by example. I have had the privilege of working with Joseph Fowler on both the MINT and ACT campaigns, from the roof tops of Jadwin to the Atacama. Among the graduate students, my direct work on detectors with Rolando Dunner, Judy Lau, Michael Niemack and Adam Hincks over the past years has been an adventure full of new experimental and theoretical challenges. Asad Aboobaker, Eric Switzer, and Ryan Fisher have been fine labmates. Asad in particular worked with me on MINT in Chile. Jay Chervenak, Harvey Moseley, and colleagues at NASA Goddard are responsible for the fabrication of the ACT detectors and have provided guidance on their characterization. Randy Doriese, Kent Irwin, and colleagues at NIST Boulder have been a great help, providing the SQUID amplifiers as well as detector insights. Among the staff at Jadwin, Bert Harrop has been our wirebonding guru and has begun taking a more significant role in detector

packaging. Bob Margolis is the project manager for ACT. I'm indebted to Bill Dix, Mike Peloso and others in the machine shop. I'm grateful to all in purchasing and receiving, especially Claude Champagne. Helena Gleskova and Joe Palmer at PRISM lab were most helpful in getting our new detector silicon packaging scheme off the ground.

The most fundamental contributor to my well-being over the past years has been my wife, Hyeseung. I love her dearly.

My research at Princeton has been supported by several fellowships: the NSF Graduate Research Fellowship, the Princeton Graduate School Centennial Fellowship, and the Harold W. Dodds Fellowship have provided me with academic financial support for all but one year of my graduate studies.

# Contents

# List of Figures

1.4 **The Temperature Power Spectrum of the CMB.** The WMAP data show the first and second peaks in the power spectrum at $\ell = 220$ and 550, respectively [17, 18]. ACBAR and CBI data show the damping tail and a potential increase in power at high $\ell$ [20, 30]. Some low $\ell$ data from ACBAR and CBI have been excluded from the plot for clarity. An approximate correspondence between multipole $\ell$ and angular scale $\theta$ is $\theta \approx 180^\circ/\ell$. Plotted through the data is a spectrum corresponding to a flat cosmogony dominated by dark energy and dark matter [39]. The power spectrum is given in terms of $\ell(\ell+1)C_\ell/2\pi$ which is the temperature variance per logarithmic interval in $\ell$ for $\ell \gg 1$. 10

1.5 **Linear Brightness Temperature Spectrum of Primary CMB Anisotropies.** The linear spectrum in terms of a multipole moment $\ell$ (left) can readily be used to estimate power in a given range of $\ell$. For instance, in the range $\ell = 0$ to 400, the spectrum level is $\sim 5$ $\mu$K. The corresponding RMS variation is roughly $5\mu\text{K} \times 400^{1/2} = 100$ $\mu$K consistent with the RMS fluctuation level in the CMB temperature map of Figure 1.3. The linear spectrum in terms of angular scale $\theta$ (right) may be obtained from the multipole function by the approximate transformation $\theta$=180/$\ell$. To estimate the RMS temperature variation in patches of sky of a given range of angular sizes, multiply the spectrum level by the square root of the range. For instance, between 0.06° and 0.07°, the fluctuations are at an average level of $25\ \mu\text{K/deg}^{1/2} \times (0.01^\circ)^{1/2} \approx 2.5\ \mu$K. . . . . 12

5.2 **SQUID Flux-Locked Loop.** The open loop voltage response of the SQUID amplifier has sinusoidal dependence on the magnetic flux coupled to the junction loop by the input inductor L. In the flux locked configuration, the output of the SQUID is preamplified ($G_1$) and fed into a differencing amplifier (G). The differencing amplifier output is then transduced back to the SQUID as a feedback flux which, in the limit of high gain G, cancels any fluctuations in flux from the input. Therefore, in a high gain system, the total flux $\Phi$ into the SQUID does not change and the output of the SQUID $V_{SQ}$ is kept in the linear regime at $V_{SET}$. Input current fluctuations are reflected in the feedback current as $\delta I_{IN} = M_{FB}\delta I_{FB} \ / \ M_{IN}$. An important note is that the FLL is stable on any positive slope of the SQUID voltage response, corresponding to a multiplicity of FLL setpoints shown in circles. If follows that the SQUID current measurement is only a relative measurement of device current. Section 5.6 describes a way to calibrate the SQUIDs such that the absolute value of the current may be derived. 81

# List of Tables

5.2 **Model Fit Parameters for Noise and Complex Impedance Data.** This table shows the model parameters describing the circuit in Figure 5.1 as fit to the X.3-2.01 data in Figure 5.7. The data are listed for the five operating points shown in the $I_o$-$V_o$ curve at the top of Figure 5.1 and listed at the top of the table. As expected, the temperatures of the absorber, lattice and TES are nearly the same because the the on-pixel thermal conductivities $G_{ep}$ and $G_a$ are much larger than the thermal conductivity of the narrow silicon legs $G_o$. The heat capacities $C_o$, $C_l$, and $C_a$ are reasonable for the TES electron, the pixel phonons, and the absorber electrons, respectively. The jump in $\alpha$ between the 17 m$\Omega$ and 12 m$\Omega$ operating pionts is consistent with the "clumping" of the data in Figure 5.1, and indicates that the transition of the MoAu bilayer is not smooth. At low frequencies ($\leq$ 10 Hz), the bolometer acts as a lumped thermal mass with heat capacity $C_o$ + $C_l$ + $C_a$ and a thermal link to the bath of $G_o$. The model fit parameters for X.3-2.01 are provided by Rolando Dunner. . . . . 96

# Chapter 1

# The Cosmic Microwave Background

## 1.1 Introduction

The cosmologist ventures to use the light in the sky to verify a physical theory of the shape, content, and evolution of the universe. This chapter explores the language cosmologists use to classify sky brightness and delves into the character of one particular source of light: the Cosmic Microwave Background (CMB).

## 1.2 Quantifying Sky Brightness

In order to characterize the light in the sky, a brightness measure must be established. Brightness may be specified in terms of intensity – the power flux from a given solid angle of the sky at a given frequency. Integrated over a source's solid angle, the intensity becomes a flux density, the standard unit of which is the Jansky (1 Jy $=10^{-26}$ W m$^{-2}$ Hz$^{-1}$) – the flux scale for most radio sources. A common way of expressing intensity is in terms of equivalent black body temperature. A black body

at temperature T has a specific intensity of

$$B_\nu(T) = \frac{2h\nu^3}{c^2}\frac{1}{e^{h\nu/kT}-1}, \tag{1.1}$$

where k is Boltzmann's constant, h is Planck's constant, and c is the speed of light. Given an intensity $S_\nu$, the corresponding equivalent black body temperature is

$$T_b = B_\nu^{-1}(S_\nu). \tag{1.2}$$

$T_b$ is called the brightness temperature of the source. In the Rayleigh-Jeans limit where $kT \gg h\nu$, the black body spectrum is approximately $B_\nu \approx 2kT\nu^2/c^2$. From this approximation, the Rayleigh-Jeans temperature is defined

$$T_{RJ} = \frac{c^2}{2k\nu^2}S_\nu. \tag{1.3}$$

The Rayleigh-Jeans temperature has the advantage of being linear with intensity. It has the disadvantage of being an inaccurate proxy for brightness temperatures when the frequency $\nu$ (GHz) approaches 20 T (K). Finally, if a brightness temperature fluctuation $\delta T_b$ is specified, then the corresponding fluctuation in intensity is well approximated by

$$\delta S_\nu = \frac{dB_\nu(T)}{dT}\delta T_b = \frac{2h^2\nu^4}{kT^2c^2}\frac{e^{h\nu/kT}}{(e^{h\nu/kT}-1)^2}\delta T_b. \tag{1.4}$$

## 1.3 The Cosmic Microwave Background

In the early 1960s, A. A. Penzias and R. W. Wilson of Bell Laboratories operated a telescope sensitive to a frequency $\nu_\circ = 4.080$ GHz ($\lambda_\circ = 7.353$ cm). At whatever point Penzias and Wilson pointed their telescope in the sky, they detected radiation with a brightness temperature of 3.5 K $\pm$ 1.0 K. This isotropic radiation, which dominated other cosmic sources in the microwave band, was reported in their 1965 letter to the Astrophysical Journal "A measurement of excess antenna temperature at 4080 Mc/s".

Seeking an explanation for the 3.5 K excess, the Bell Lab scientists contacted R. H. Dicke and colleagues at Princeton University. The Princeton physicists had already theorized the existence of an isotropic background of microwave radiation from the Big Bang consistent with the measurements at Bell Labs. Alongside Penzias and Wilson's letter, Dicke and colleagues published a letter entitled "Cosmic Black-Body Radiation" which offered the cosmological interpretation of the Bell Labs scientists' measurement. Experiments by D. T. Wilkinson and colleagues at Princeton soon verified the 3K background radiation of Penzias and Wilson at different frequencies and improved upper limits on its anisotropy. The 3K radiation became known as the Cosmic Microwave Background (CMB) and gave credence to the theory of the universe as expanding from a hot big bang. For their discovery of the CMB, Penzias and Wilson received the 1978 Nobel Prize in Physics.

The CMB may be described as the backlight to the universe as Figure 1.1 illustrates. In an expanding universe, the intensity of radiation is higher in the past when the photons are packed in a smaller space. So at very early times, the radiation temperature was high enough such that neutral atoms, when formed, would be immediately broken into their proton and electron consituents by high energy photons. The CMB was emitted when the intensity of radiation in the early universe was low enough that atoms could form. With all the protons and electrons bound in neutral atoms, photons could travel relatively unimpeded by charged particles through to today. Because the photons electromagnetically decoupled from matter, this point in the universe is called decoupling. Before decoupling, the universe was a black body, the mean free photon path length being negligibly small due to charged particles scattering off. It follows that the CMB, emitted from the early opaque universe, should be characterized by a black body spectrum. Because the photons, electrons, and protons were tightly coupled in a plasma state before emission of the CMB, any brightness

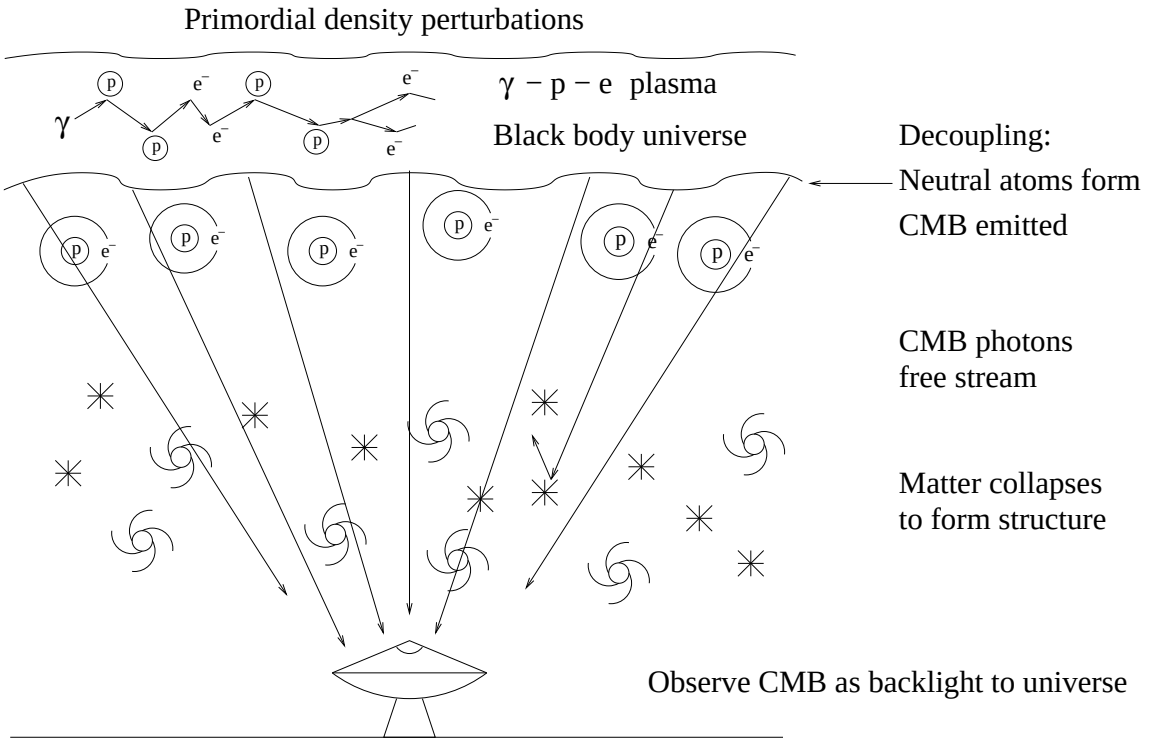


Figure 1.1: **CMB as a Backlight to the Universe.** The CMB was emitted when the intensity of radiation in the universe was low enough that atoms could form. Before this time, protons and electrons which formed atoms would be immediately separated by collisions with photons, and conversely the photon mean free path between scatters was negligibly small. It follows that the early universe was a black body, and thus the CMB, being emitted by the early universe, bears a black body spectrum. It also follows that any fluctuations in the brightness of the CMB reflect density fluctuations in charged matter at decoupling. Such fluctuations were seeded at the beginning of the universe, so study of the CMB gives information on the physical method by the which the universe, as we know it, was created. After the decoupling of radiation from matter, the CMB photons for the most part stream freely through the universe. The matter, no longer tied to the photons by the electromagnetic force, clumps gravitationally and forms the structures observed today.

fluctuations in the primarily isotropic CMB reflect density fluctuations in the charged matter of the universe at decoupling. A third substantial player at decoupling was dark matter which, having no electromagnetic interactions, interacted with the primordial plasma of photons, protons, and electrons through gravity. At decoupling, the protons and electrons, in the form of neutral atoms no longer perturbed by collisions with photons, were able to gravitationally collapse along with the dark matter into the structures observed in the universe today. Therefore, by studying both the CMB and the large scale structure of matter today, much can be learned about the universe's shape, energy content, and evolution. To date, observations have elucidated the universe's geometry, energy content, age, ionization history, and expansion rate, among other attributes [39]. In addition to providing information about the universe at the time of decoupling, the fluctuations in the CMB are also indicators of physics before decoupling. In particular, the CMB can give us information about the seed perturbations in energy and space that were in place at the very beginning of the universe and therefore provide essential clues as to the physical means by which the universe, as we know it, was created. This primordial aspect of the CMB has only begun to be addressed by observations and remains a primary motivation of current cosmological investigations.

Thirty years after the discovery of the CMB, the Far Infrared Absolute Spectrophotometer (FIRAS) aboard the Cosmic Background Explorer (COBE) definitively measured the CMB brightness temperature to be 2.725 K $\pm$ 0.002 K from 60-600 GHz [10]. Figure 1.2 shows the FIRAS measurement alongside the original result from Penzias and Wilson.

While FIRAS made an absolute temperature measurement of the CMB, another instrument aboard COBE, the Differential Microwave Radiometer (DMR), measured differences in brightness temperature between points on the sky separated by 60° at

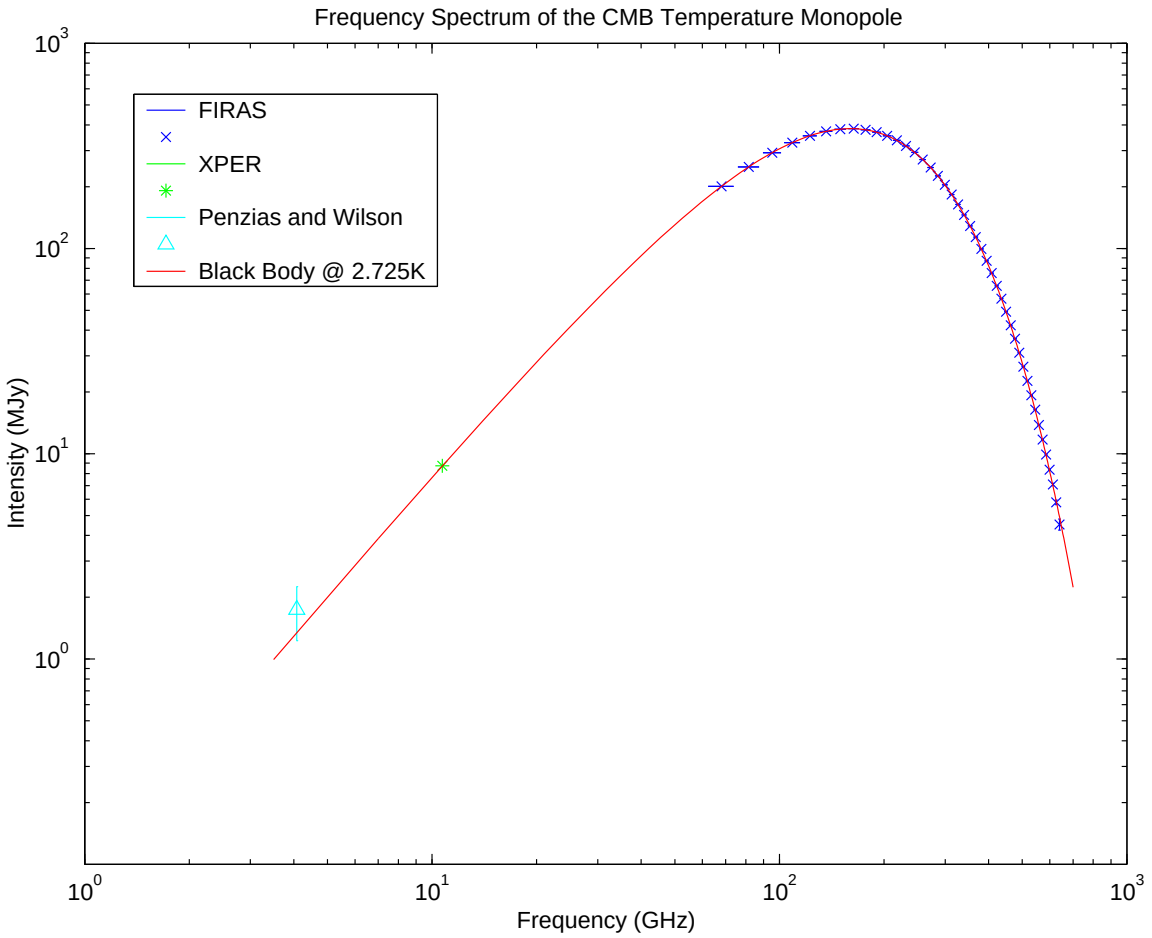


Figure 1.2: **The Frequency Spectrum of the CMB Temperature Monopole.** Thirty years after Penzias and Wilson measured an unexpected 3.5 K ± 1.0 K isotropic background at 4.080 GHz, the FIRAS aboard COBE measured the CMB brightness temperature to be 2.725 K ± 0.002K in the frequency range 60-600 GHz [35, 10]. Other experiments, such as XPER, have measured intermediate points [40, 11]. Reference [11] provides a tabulation of other frequency spectrum measurements. The y-axis unit is intensity given in Janskys per steradian.

31.5, 53, and 90 GHz. With its seven degree resolution, COBE DMR was the first experiment to detect the brightness temperature anisotropy in the CMB at a level of $\approx$ 30 $\mu$K. Beyond detecting the anisotropy, COBE DMR made a full sky map of the CMB temperature variation [2]. About ten years later, another satellite, the Wilkinson Microwave Anisotropy Probe (WMAP), measured the anisotropy over the entire sky at 23, 33, 41, 61, and 94 GHz with subdegree resolution [3]. Figure 1.3 shows maps of the CMB temperature anisotropy from COBE and WMAP.

A useful characterization of the CMB temperature maps is the angular power spectrum which measures the variation in the CMB temperature at a given angular scale. Because the CMB temperature field is described in spherical coordinates, the temperature anisotropies are analyzed in terms of spherical harmonics $Y_{lm}(\vec{n})$ where $\vec{n}$ is a unit vector encoding angular coordinates. The temperature fluctuations $\Delta T(\vec{n})$ can then be described by the equation

$$\Delta T(\vec{n}) = \sum_{l=1}^{\infty} \sum_{m=-\ell}^{m=\ell} a_{lm} Y_{\ell m}(\vec{n}). \tag{1.5}$$

The Fourier coefficients $a_{\ell m}$ are given by the mapping

$$a_{lm} = \int d\Omega Y^*_{\ell m}(\vec{n}) \Delta T(\vec{n}). \tag{1.6}$$

If $\Delta T(\vec{n})$ is a Gaussian random variable, then the Fourier coefficient amplitudes are also Gaussian distributed with zero mean and variance described by

$$\langle a_{\ell m} a^*_{\ell' m'} \rangle = C_\ell \delta_{\ell \ell'} \delta m m', \tag{1.7}$$

where the brackets denote an ensemble average given a parent distribution. The variance $C_\ell$ is assumed independent of the Fourier index 'm' because the physical mechanisms producing temperature anisotropies on a given angular scale have no preferred direction. For Fourier coefficients derived from a measurement of the Cosmic Microwave Background, the power spectrum at a given $\ell$ is the average over the

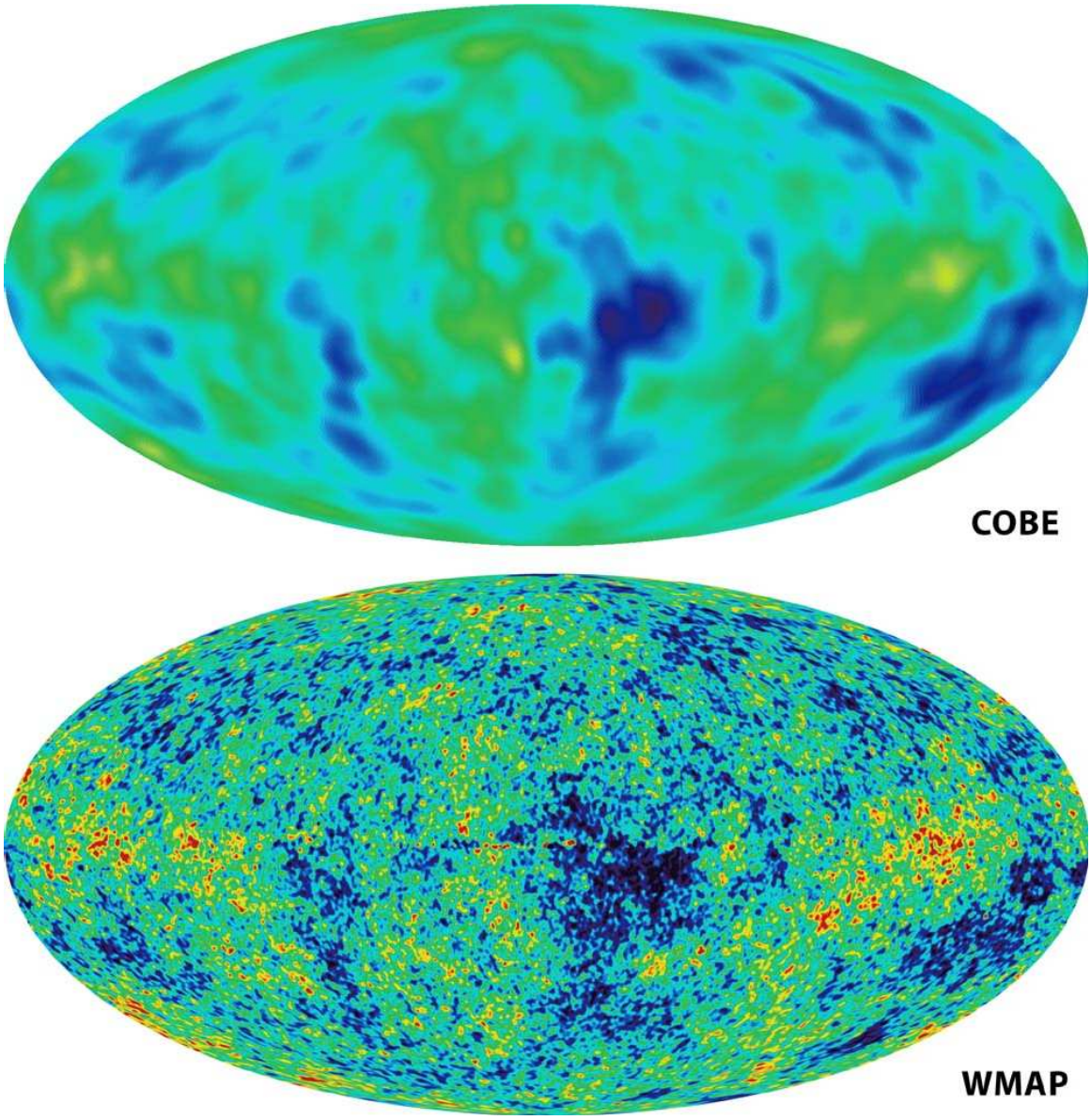


Figure 1.3: **Sky Maps of the CMB Brightness Temperature Anisotropy.** The brightness temperature of the CMB is anisotropic at the level of one part in $10^5$. In the maps, the dipole anisotrophy due to the earth's motion has been removed. COBE DMR was the first instrument to detect the anisotropy and produced a full sky map with seven degree resolution [2]. Ten years later, WMAP remapped the anisotropy at subdegree resolution and over more frequencies [3, 18]. The maps shown above are synthesized from the first year of WMAP multifrequency data and are presented in Mollweide projection in Galactic coordinates. The color scale ranges from -200 $\mu$K (dark blue) to 200 $\mu$K (red). The images are provided by the NASA/WMAP science team from the WMAP mission website.

corresponding $2\ell + 1$ Fourier coefficients:

$$C_\ell^{meas} = \frac{1}{2\ell + 1} \sum_{m=-\ell}^{\ell} |a_{\ell m}|^2. \tag{1.8}$$

Because the number of multipoles corresponding to a given $\ell$ is limited, the measurement of power in Equation 1.8 has a fundamental precision limit due to "cosmic variance" which decreases with multipole moment as $1/(2\ell + 1)^{1/2}$. Figure 1.4 shows power spectrum measurements from WMAP, the Arcminute Cosmology Bolometer Array Receiver (ACBAR), and the Cosmic Background Imager (CBI). The WMAP data, which is cosmic variance limited through $\ell \approx 400$, shows a prominent peak at $\ell = 220$ and a secondary peak at $\ell = 530$ [17, 18]. ACBAR and CBI show that the anisotropies dampen beyond the first peaks with a possible rise in power at higher multipoles ($\ell \geq 2000$) [20, 30]. Using the approximation $\theta \approx 180°/\ell$ to translate from multipole $\ell$ to degrees, the first peak in the spectrum corresponds to temperature variation at the degree scale after which damping sets in with a potential upturn in power on angular scales smaller than ten arcminutes.

The power spectrum in Figure 1.4 is plotted in the conventional units of $\ell(2\ell + 2)C_\ell/4\pi$ ($\mu$K$^2$). To good approximation, this normalization gives the brightness temperature angular power spectrum for logarithmic intervals in $\ell$. Additionally, the normalization is chosen to emphasize the peaks of the spectrum. The first factor of $\ell$ converts the temperature spectrum to $\log(\ell)$ space ($d\ell/d(\log(\ell)) = \ell$). Next considering the $1/4\pi$ factor, the $Y_{lm}$ functions, by virtue of their unit normalization, have physical units of sr$^{-1/2}$. It follows then from Equation 1.6 that $a_{lm}$ has units of $\mu$K-sr$^{1/2}$, and so $C_\ell$ has units of $\mu$K$^2$-sr. Therefore, $C_\ell$ gives a measure of the power flux from $4\pi$ steradians, and the $1/4\pi$ factor converts the $C_\ell$ into an intensity. Finally, from Equation 1.8, the total brightness temperature density at a given multipole would be $(2\ell + 1)C_\ell/4\pi$. The factor $(2\ell + 2)$ is used instead of $(2\ell + 1)$ for historical consistency. For high multipoles, $(2\ell + 2) \sim (2\ell + 1)$.

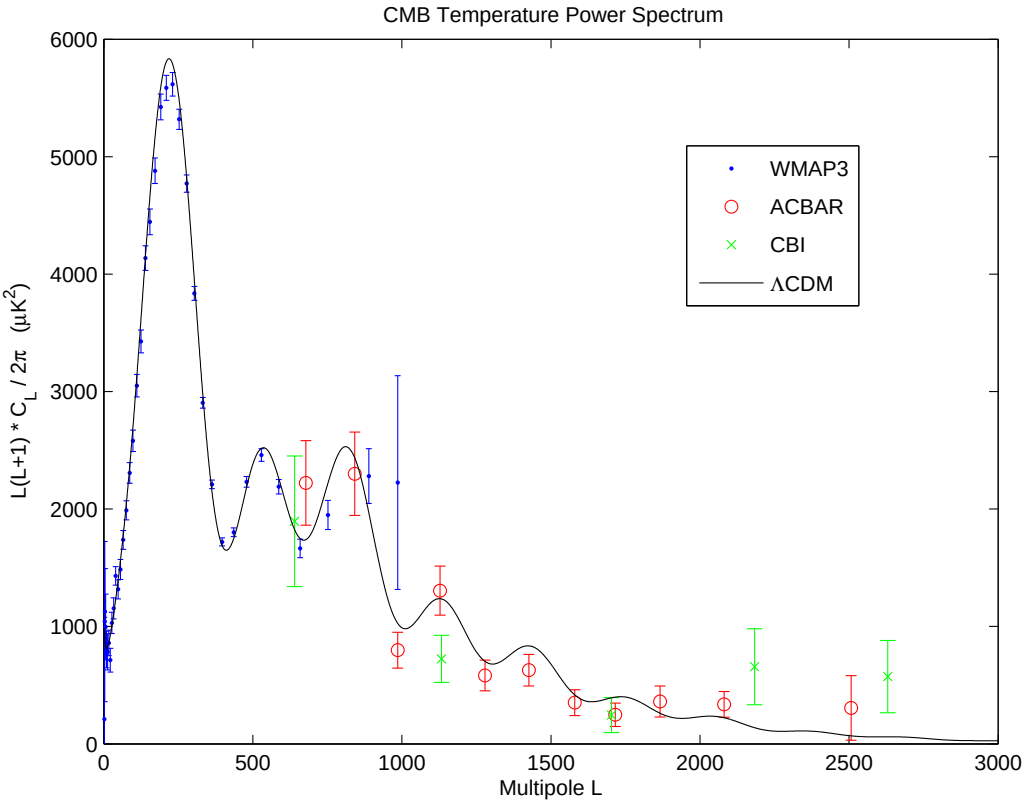


Figure 1.4: **The Temperature Power Spectrum of the CMB.** The WMAP data show the first and second peaks in the power spectrum at $\ell = 220$ and 550, respectively [17, 18]. ACBAR and CBI data show the damping tail and a potential increase in power at high $\ell$ [20, 30]. Some low $\ell$ data from ACBAR and CBI have been excluded from the plot for clarity. An approximate correspondence between multipole $\ell$ and angular scale $\theta$ is $\theta \approx 180^\circ/\ell$. Plotted through the data is a spectrum corresponding to a flat cosmogony dominated by dark energy and dark matter [39]. The power spectrum is given in terms of $\ell(\ell+1)C_\ell/2\pi$ which is the temperature variance per logarithmic interval in $\ell$ for $\ell \gg 1$.

It follows from the discussion of spectrum normalization in the previous paragraph that the linear temperature angular spectrum as a density in $\ell$ (not $\log(\ell)$) space is

$$\sqrt{\frac{(2\ell+1)C_\ell}{4\pi}}. \tag{1.9}$$

Using the approximation $\ell = 180/\theta$, the linear spectrum can be expressed in degree-unit $\theta$ space as

$$\sqrt{\frac{(360/\theta+1)C_{\ell=180/\theta}}{4\pi} \times \frac{180}{\theta^2}}, \tag{1.10}$$

where the factor $180/\theta^2$ is the Jacobian for the $\ell \rightarrow \theta$ transformation. Figure 1.5 shows a plot of the linear brightness temperature spectra as given in Equations 1.9 and 1.10. Using the graph of the linear spectrum versus angular scale $\theta$, one can estimate the temperature sensitivity necessary to resolve CMB anisotropies among adjacent patches of sky within a range of solid angles. For instance, between 0.06° and and 0.07°, the linear spectrum averages $\sim 25\ \mu\text{K/deg}^{1/2}$. To convert this level to an RMS temperature difference between adjacent $\sim 0.065°$ size patches, one multiplies 25 $\mu$K by the square root of the angular size of the patch, $25\ \mu\text{K/deg}^{1/2} \times (0.01)^{1/2} = 2.5\ \mu$K level.

## 1.4 Discussion

Much of the cosmological significance in measurements of the CMB lies in the power spectrum. For instance, the location of the first peak in the CMB is a strong indicator of the geometry of the universe, and the relative heights of the peaks and troughs encode information on the mean density of protons and electrons in the universe [32]. Of particular interest to scientists today is the overall spectral tilt of the CMB anisotrophies which bears the signature of the initial perturbations present when the universe as we know it began evolving. To best determine the spectral tilt, future experiments must complement the WMAP CMB anisotropy measurements at low $\ell$

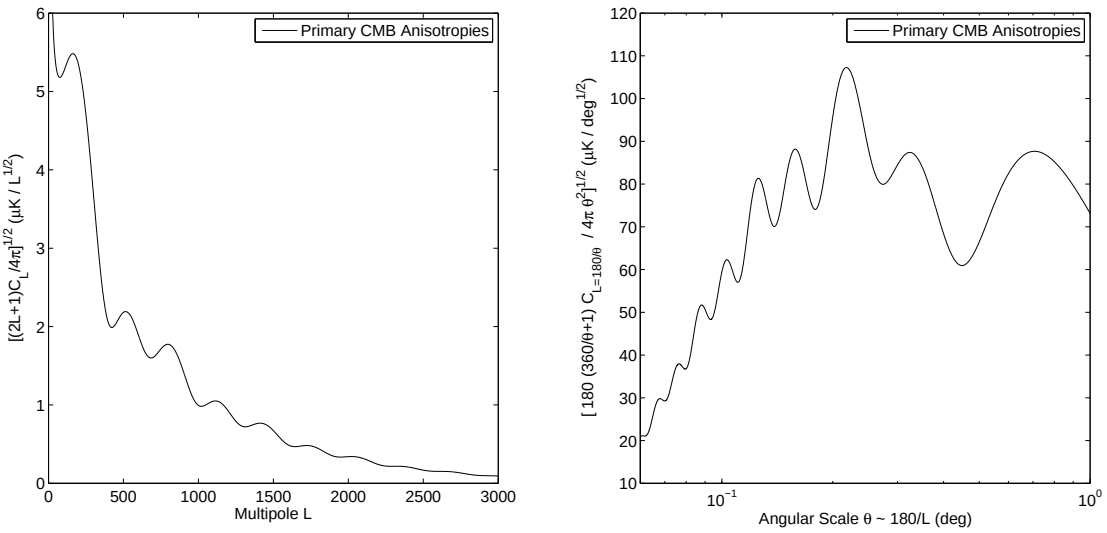


Figure 1.5: **Linear Brightness Temperature Spectrum of Primary CMB Anisotropies.** The linear spectrum in terms of a multipole moment $\ell$ (left) can readily be used to estimate power in a given range of $\ell$. For instance, in the range $\ell = 0$ to 400, the spectrum level is $\sim 5$ $\mu$K. The corresponding RMS variation is roughly $5\mu\text{K} \times 400^{1/2} = 100$ $\mu$K consistent with the RMS fluctuation level in the CMB temperature map of Figure 1.3. The linear spectrum in terms of angular scale $\theta$ (right) may be obtained from the multipole function by the approximate transformation $\theta$=180/$\ell$. To estimate the RMS temperature variation in patches of sky of a given range of angular sizes, multiply the spectrum level by the square root of the range. For instance, between 0.06° and 0.07°, the fluctuations are at an average level of 25 $\mu\text{K}/\text{deg}^{1/2} \times (0.01°)^{1/2} \approx 2.5$ $\mu$K.

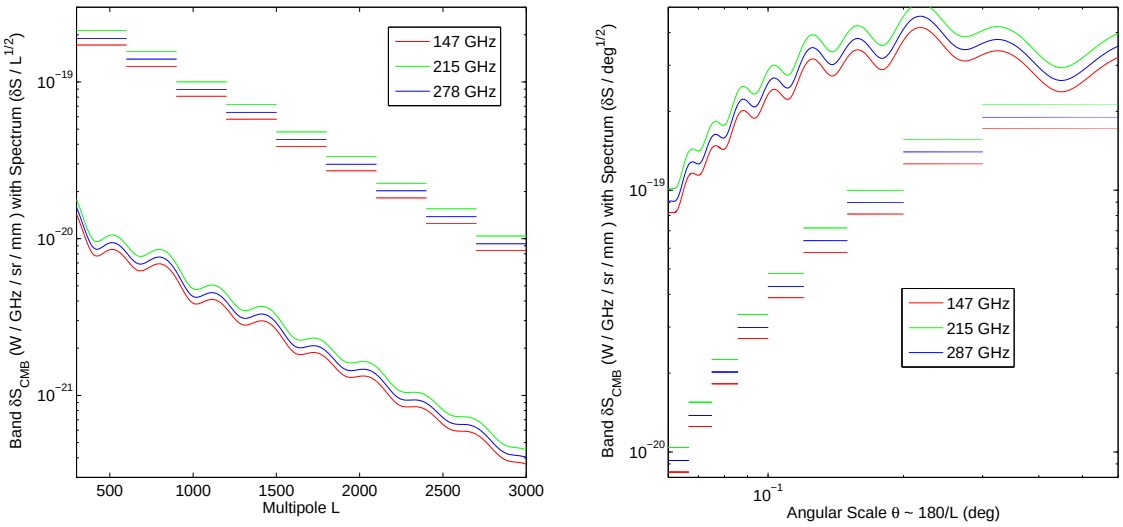


Figure 1.6: **CMB Intensities for ACT.** The continuous red, green, and blue curves are CMB linear intensity spectra at 147, 215, and 278 GHz, respectively. These frequencies correspond to the centers of the ACT signal bands. The red, green, and blue level sections show the RMS intensity fluctuation expected in the range of multipoles (left) or angular sizes (right) spanned by the sections. For instance, in multipole space, the RMS intensity fluctuations result from integration of the spectrum over sections 300 multipoles wide from $\ell$ = 300-3000. The intensity is expressed in terms of W/sr/GHz/mm$^2$, which is a natural unit given ACT's gigahertz wide bands and millimeter sized detectors. The spectrum Table 1.1 lists the values for the integrated intensities.

with measurements of anisotropy at high $\ell$ , corresponding to angular scales from roughly a degree down to a few arcminutes. As discussed in the previous section, this means measuring brightness temperatures between $\sim$ 80 $\mu$K at the degree scale to $\sim$ 2.5 $\mu$K at the scale of arcminutes.

Anticipating the next chapter, Figure 1.6 shows a plot of the RMS intensity level of CMB fluctuations for frequencies 147 GHz, 215 GHz, and 278 GHz in spatial frequency bands spanning $\ell$ = 300-3000. These frequencies correspond to the signal band centers of the Atacama Cosmology Telescope (ACT), which is the topic of

| $\Delta\ell$ | $\Delta\Theta$ (deg) | $\delta T_b$ ($\mu$K) | $\delta S_{147}$ | $\delta S_{215}$ | $\delta S_{278}$ |
|---|---|---|---|---|---|
| | | | (W / GHz / mm$^2$ / sr) | | |
| 300-600 | 0.60-0.30 | 44.0 | 1.72E-19 | 2.13E-19 | 1.90E-19 |
| 600-900 | 0.30-0.20 | 32.4 | 1.26E-19 | 1.56E-19 | 1.40E-19 |
| 900-1200 | 0.2-0.15 | 20.8 | 8.11E-20 | 1.00E-19 | 8.97E-20 |
| 1200-1500 | 0.15-0.12 | 14.8 | 5.79E-20 | 7.17E-20 | 6.41E-20 |
| 1500-1800 | 0.12-0.10 | 9.9 | 3.88E-20 | 4.80E-20 | 4.29E-20 |
| 1800-2100 | 0.10-0.086 | 6.9 | 2.71E-20 | 3.35E-20 | 2.99E-20 |
| 2100-2400 | 0.086-0.075 | 4.7 | 1.82E-20 | 2.26E-20 | 2.02E-20 |
| 2400-2700 | 0.075-0.067 | 3.2 | 1.25E-20 | 1.55E-20 | 1.38E-20 |
| 2700-3000 | 0.067-0.06 | 2.15 | 8.38E-21 | 1.04E-20 | 9.27E-21 |

Table 1.1: **Temperatures and Intensities from Primary CMB Anisotropies.** Listed in the table are the RMS levels of brightness temperature and intensity fluctuations derived by integrating the CMB temperature power spectrum over the specified ranges in $\ell$ or $\Theta$. For instance, the last row in the table gives the RMS temperature and intensity fluctuations that one expects to see between adjacent spots of angular width $\sim$ 4 arcminutes. The frequencies for which intensities are chosen correspond to the centers of the ACT signal bands. Figure 1.6 is a plot of the intensity spectra for the ACT bandcenters along the derived RMS intensities listed in this table. The units of intensity are W/sr/GHz/mm$^2$. In Chapter 2, a study of the atmosphere and telescope relates these intensities to power absorbed by the ACT detectors.

Chapter 2. The next chapter discusses how ACT collects power from the intensity fluctuations (see Figure 1.6) and delivers that power to the detectors in the telescope's focal plane.

## 1.5 Acknowledgements

The treatment of the CMB temperature anisotropy spectrum benefitted from discussions with Lyman Page, Norman Jarosik, and Michael Nolta.

# Chapter 2

# The Atacama Cosmology Telescope

## 2.1 Introduction: Focusing Sky Brightness onto Detectors

The Atacama Cosmology Telescope (ACT) will observe the CMB in approximately two-hundred square degrees of sky from its site in the Atacama Desert in the Andes of Northern Chile. Observations will be made simultaneously in three frequency bands centered on 147.2 GHz, 215 GHz, and 278.7 GHz. The site, Cerro Toco, is chosen for its high altitude (5200m) and low precipitable water vapor, a major contributor to absorption and brightness in ACT's three bands. Due to the telescope's large six-meter primary mirror, ACT will effectively probe the CMB anisotropy from half-degree scales down to arcminutes. The full optics, from the primary mirror on the telescope to the final cryogenic lens in the receiver, effectively image a wide field ($\sim 30$ arcminutes) onto 1000 detectors. Simultaneous observing with 1000 detectors drastically increases the telescope's sensitivity, enabling the detection of the arcminute-scale CMB over the large 100°+ ACT mapping region.

This chapter investigates how ACT delivers light to a single detector. The aim

of the chapter is two-fold. First, a study of the emission from the atmosphere and telescope optics quantifies the level to which the detectors are loaded by background radiation. The background radiation is generally 10-50 times brighter than the 3 K CMB, so that the amplitude of the CMB anisotropies are less than one part in $10^6$ of the total loading. The second goal of the chapter is to account for the absorption and reflection of the cosmic signal by the atmosphere and telescope optics. Such an account of absorption and reflection reveals the efficiency with which the cosmic signal is delivered to the detectors.

## 2.2 Observations

From -23° latitude and 68° longitude, ACT will perform scans at fixed elevation centered at two points on either side of the arc between the southern celestial pole (SCP) and the zenith. One scan under consideration is 5° wide in azimuth with scan centers at azimuths of 210.5° and 149.5° [12], where north is 0° azimuth. The scan elevation is 48°. As the sky rotates, a strip 2.1° wide on the sky is scanned around the SCP at a declination of 55° (35° from the SCP). The area of the strip is approximately 245 square degrees. Figure 2.1 illustrates the scan.

There are two major advantages from the proposed ACT scan pattern. First, scans at constant elevation sweep through a constant atmospheric airmass. The atmosphere both absorbs cosmic signals and radiates as a gray body. In fact, the atmosphere is the brightest source seen by the detectors (see Section 2.3). Therefore, scanning through a constant airmass avoids scan-synchronous modulation of both the system gain (cosmic signal absorption) and the background power (gray body emission). Chapter 3 will explain how changes in background power can also produce unwanted changes in the detector responsivity and noise. Second, by performing two scans which mirror one another across the arc between the SCP and zenith, the observed strip of sky will be

scanned in two different crosslinked directions (see Figure 2.1). By scanning the strip in more than one orientation, unwanted systematics associated with a unidirectional scan (i.e.,"striping") can be removed during analysis of the sky maps. The ACT scan strategy has not yet been determined; the final strategy, however, will undoubtedly include crosslinked scans at constant elevation.

## 2.3 Atmospheric Characterization at Cerro Toco

The mountain of Cerro Toco overlooks the Chajnantor plain, which is home to the CBI, the Atacam Pathfinder Experiment (APEX), and the future Atacama Large Millimeter Array (ALMA) telescopes. It also served as the site for the TOCO and MINT telescopes [31, 14]. Accessible by paved highway and mountain roads, the Toco site is approximately fifty kilometers from the nearest town. Logistical challenges include telescope assembly, remote operation, and maintenance of ACT at altitude.

The suitability of Cerro Toco and Chajnantor for astronomy derives from the excellent millimeter and submillimeter atmospheric transparency afforded by the high altitude desert atmosphere. Chajnantor's atmospheric opacity at 225 GHz has been monitored since the early 1990s by the National Radio Astronomy Observatory (NRAO) in collaboration with the European Southern Observatory (ESO) as part of the ALMA project [27, 38, 37]. In addition to the 225 GHz opacities, the NRAO/ESO monitors temperature, winds, and pressure using both radiosondes and ground weather stations. All the NRAO/ESO site characterization data are available through their website. The following reviews a study by the author of the atmospheric brightness temperature at Chajnantor/Cerro Toco [28]. In this study, an atmospheric modeling program, Atmospheric Transmission at Microwaves (ATM), is used to extrapolate the NRAO/ESO 225 GHz opacity data to the ACT observing bands [33].

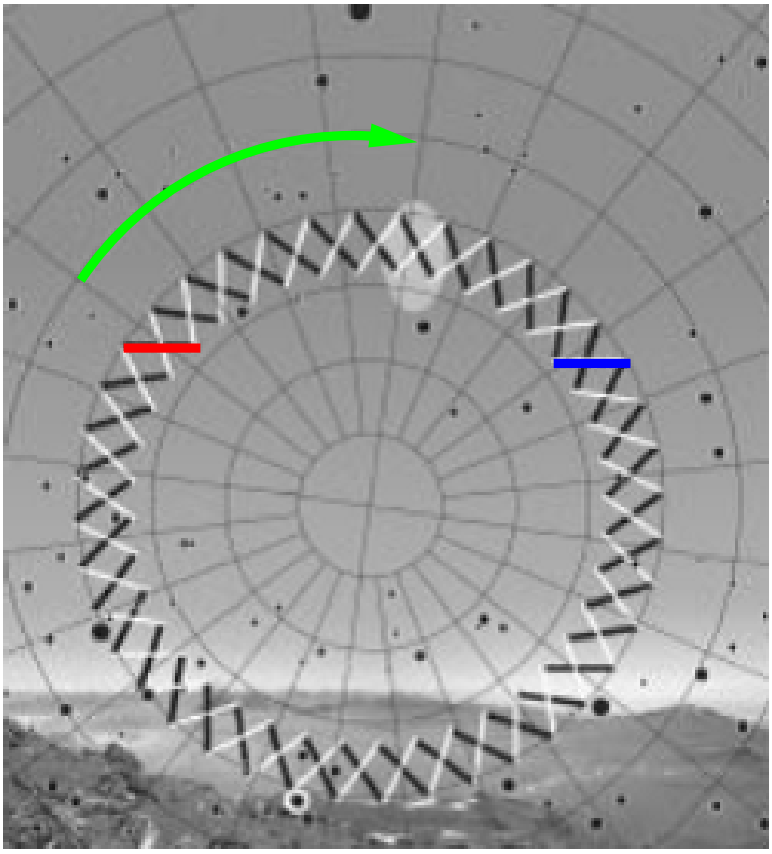

Figure 2.1: **Example ACT Scan Pattern.** ACT will face south over the Chajnantor plain. The SCP (the center of the celestial over-grid) is 23° above the southern horizon. ACT will alternatively point and scan along two stripes of constant elevation (e.g., 48°), illustrated here by bold red and blue lines. As the sky rotates (green arrow), the scans will cover a strip approximately two degrees wide around the SCP. Stripes generated by scanning at the blue (red) location appear white (black) around the strip. By scanning the strip in cross-linked (black-white) directions, systematic defects associated with a unidirectional scan can be removed from sky maps in the analysis. The width of the strip is exaggerated in this figure. The grayscale figure, which is not to scale, was provided by Jeff Klein.

The opacity (or optical depth) $\tau$ encodes how the atmosphere attentuates transmitted signals and radiates as a gray body. The specific intensity $S(\nu)$ of a cosmic signal transmitted through the atmosphere is decreased to $S'(\nu)$:

$$S'(\nu) = S(\nu)\exp(-\tau A), \tag{2.1}$$

where A is the airmass. The airmass is one for observations at zenith and $\sec(z)$ for zenith angles away from the horizon (z=90°). The atmosphere radiates as a gray body according to

$$S_{atm}(\nu) = B(\nu, T_{atm})(1 - \exp(-\tau A)), \tag{2.2}$$

where $B(\nu, T_{atm})$ is the specific intensity of a black body with the effective atmospheric temperature $T_{atm}$.

NRAO/ESO use Equation 2.2 as a model to determine $\tau$ from measurements of $S_{atm}$(225 GHz) at various airmasses. Figure 2.2 shows the opacities measured by the ALMA site characterization team throughout the year. During the austral summer, prevalent easterly winds blow water vapor from the Amazon basin into the Atacama. Evening winds are also in general easterly and likewise bring moisture. Because water vapor in the atmosphere is the dominant absorber at millimeter wavelengths, atmospheric transparency for CMB observations is generally better in the morning and during the winter. In this analysis, the year is divided between winter (June - November) and summer (December - May). The day is divided between morning (5:00–17:00 UTC) and evening (17:00–5:00 UTC).

Opacity quartiles at 225 GHz were calculated for winter (morning, night) and summer (morning, night) from the ALMA site characterization data. Values for PWV can then be fit to the 225 GHz opacities using the ATM atmospheric modeling program. ATM also provides opacities and brightness temperatures for frequencies in the ACT bands. Figure 2.3 shows the ATM-derived median RJ brightness temperatures throughout the year for frequences in and around the ACT bands. The

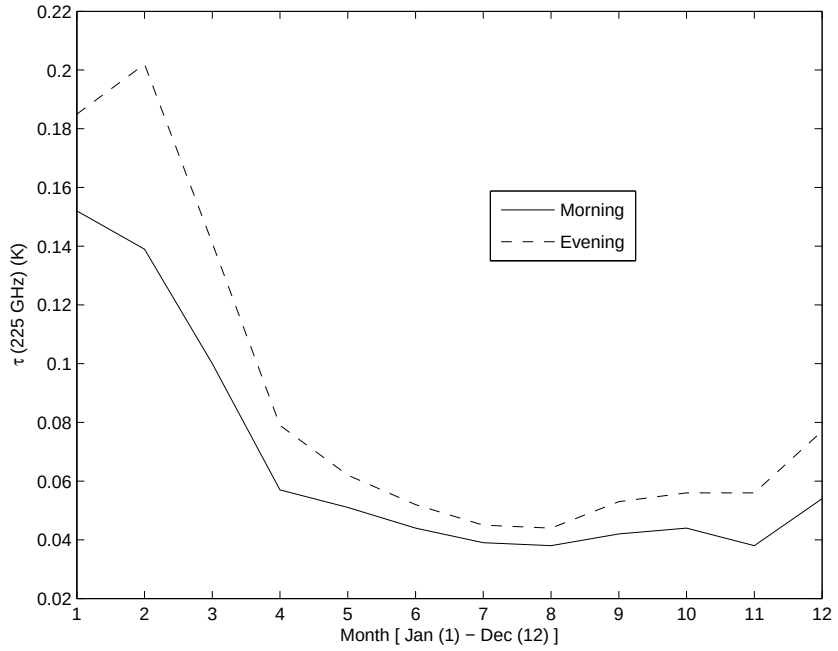


Figure 2.2: **Temporal Trends in the Median Atmospheric Opacity at Chajnantor at 225 GHz** The dominant contributor to opacity at Chajnantor (adjacent to the ACT site) is precipitable water vapor (PWV). Easterly winds in the austral summer and in the evenings bring moisture from the Amazon basin which enhances the PWV. Thus, atmospheric transparency is better in the morning and during the winter. For this study we define mornings as 5:00 – 17:00 UTC and winter as June – November. The data for the figure were taken by the ALMA site characterization team between April 1995 and January 2004 [38]. The data are available on the ALMA site characterization website.

most significant features in the atmospheric brightness spectrum are due to radiation interacting with water in the atmosphere. In particular, the continuum brightness is due to a large water resonance in the terahertz regime. Since the ACT bands mostly lie in parts of the spectrum dominated by the continuum, it follows that the atmosphere transmission and absorption as seen by ACT will fluctuate in proportion to the amount of PWV. Table 2.1 lists quartiles of PWV for Summer/Winter and Day/Night observing times. Included with each PWV in Table 2.1 are the corresponding brightness temperatures and opacities derived by averaging the ATM model spectra across the ACT bands. Other atmospheric parameters, less variable and less significant than PWV, are water vapor height scale (2.00 km), site altitude (5.0 km), and ground temperature (270 K).

## 2.4 Telescope and Receiver

Like the atmosphere, the optics of the telescope and the receiver both attenuate the cosmic signal and add their own radiation to the light ultimately absorbed at the detector. This section gives a systematic accounting of the brightness contribution and filtering due to the major telescope and receiver elements as seen by the detectors.

Figure 2.4 shows the basic optical layout of the receiver. Light from the sky reflects off of the aluminum primary and secondary mirrors, and then passes into the receiver cryostat through a polyethylene window. Once inside the receiver, the light traverses a number of filters, some which are absorbitive (neutral density filters) and others which are reflective (metal mesh). In addition to the filters, the light passes through three antireflection coated silicon lenses. After passing through the final lens, the light is focused onto the detectors.

The world as viewed from the detectors is relatively simple. Four classes of rays extend from the detectors to the cryostat or to the sky. Examples of each class are

| Quartile | Summer Evening | | | |
|---|---|---|---|---|
| | $T_{RJ}/\tau$ 147 GHz (K/nepers) | $T_{RJ}/\tau$ 215 GHz (K/nepers) | $T_{RJ}/\tau$ 278 GHz (K/nepers) | PWV (mm) |
| 25% | 11.1/0.044 | 19.9/0.082 | 33.5/0.146 | 1.10 |
| 50% | 18.1/0.072 | 34.9/0.148 | 56.5/0.256 | 2.15 |
| 75% | 33.3/0.138 | 65.9/0.299 | 101.0/0.510 | 4.42 |
| # of data | 65292 | | | |
| Quartile | Summer Morning | | | |
| | $T_{RJ}/\tau$ 148 GHz (K/nepers) | $T_{RJ}/\tau$ 215 GHz (K/nepers) | $T_{RJ}/\tau$ 278 GHz (K/nepers) | PWV (mm) |
| 25% | 8.5/0.033 | 14.0/0.057 | 24.1/0.105 | 0.69 |
| 50% | 14.1/0.056 | 26.5/0.110 | 43.5/0.193 | 1.55 |
| 75% | 27.1/0.111 | 53.6/0.236 | 83.8/0.405 | 3.50 |
| # of data | 64646 | | | |
| Quartile | Winter Evening | | | |
| | $T_{RJ}/\tau$ 148 GHz (K/nepers) | $T_{RJ}/\tau$ 215 GHz (K/nepers) | $T_{RJ}/\tau$ 278 GHz (K/nepers) | PWV (mm) |
| 25% | 7.8/0.030 | 12.4/0.050 | 21.6/0.094 | 0.58 |
| 50% | 10.1/0.039 | 17.6/0.072 | 29.8/0.130 | 0.94 |
| 75% | 14.4/0.057 | 27.0/0.112 | 44.4/0.197 | 1.59 |
| # of data | 66015 | | | |
| Quartile | Winter Morning | | | |
| | $T_{RJ}/\tau$ 148 GHz (K/nepers) | $T_{RJ}/\tau$ 215 GHz (K/nepers) | $T_{RJ}/\tau$ 278 GHz (K/nepers) | PWV (mm) |
| 25% | 6.7/0.026 | 10.1/0.041 | 17.8/0.078 | 0.42 |
| 50% | 8.5/0.033 | 14.0/0.057 | 24.1/0.105 | 0.69 |
| 75% | 12.5/0.049 | 23.0/0.095 | 38.2/0.168 | 1.31 |
| # of data | 65812 | | | |

Table 2.1: **Atmospheric Brightness Temperature, Opacity, and PWV at Chajnantor.** Quartiles of Rayleigh-Jeans brightness temperatures and opacities at 45° elevation (Airmass=1.414) are given averaged over the ACT bands. The corresponding PWV in a column towards zenith is also shown. The frequencies listed in the heading of each category are the band centers shown in Figure 2.3. The results in the table are based on opacity measurements by the ALMA group and atmospheric modeling with ATM [33, 38].

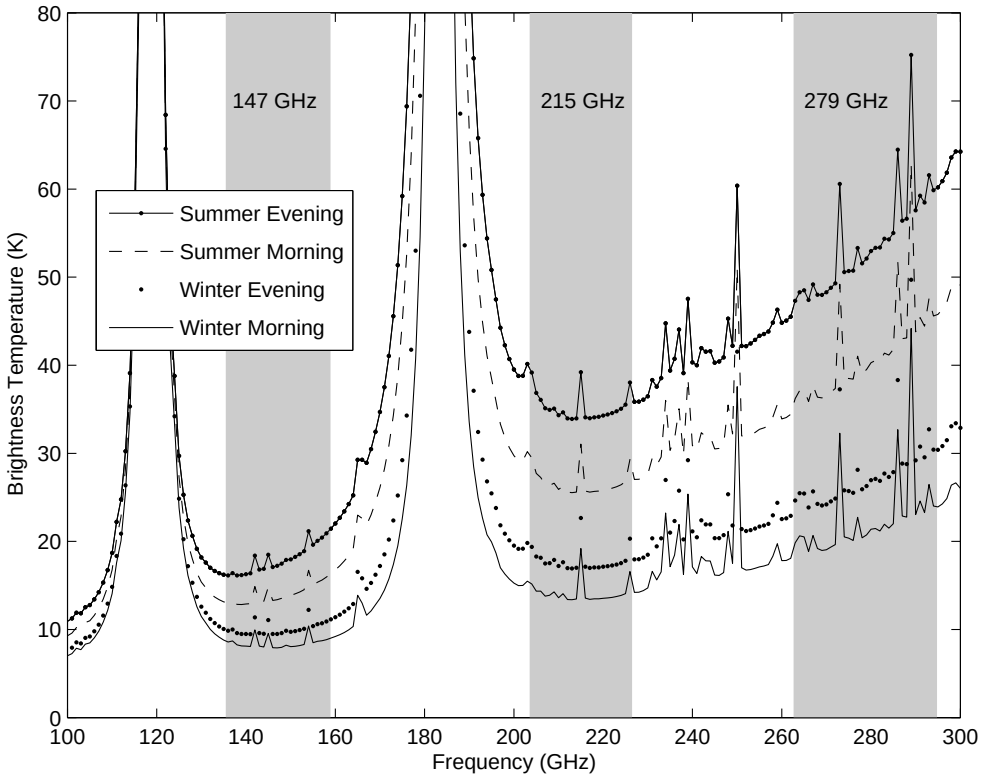


Figure 2.3: **Median Atmospheric Brightness Temperature Spectra at the ACT Site.** Rayleigh-Jeans brightness temperature spectra are shown for a observations at 45° elevation. Winters and mornings feature lower brightnesses. Winter is June to November. Morning is 5:00 to 17:00 UTC. The line at 117 GHz is due to excitation of molecular oxygen. The smaller lines are for the most part due to ozone. The line at 183 GHz is due to water. The continuum brightness comes from the wings of strong water lines at higher frequencies. The primary source of atmospheric brightness is water vapor. Seasonal and diurnal changes in the precipitable water vapor cause corresponding changes in the continuum brightness and the pictured water lines (e.g., at 183 GHz). Lines due to molecules besides water (e.g., at 117 GHz) do not change substantially. The specific intensity can be derived from the RJ brightness temperature as $2k_B\nu^2T_b/c^2$. ACT observing bands are shown shaded. Bands centered at 147.2 GHz, 215 GHz, and 278.7 GHz have bandwidths of 23.2 GHz, 22.7 GHz, and 31.9 GHz, respectively [13].

drawn and labeled one to four in Figure 2.4. Rays from the first class exit the receiver, passing through all optical elements along the way and terminating on the sky. Rays from the second class terminate at 1 K anywhere from the Lyot stop to the edge of the last lens. Rays in the third class terminate on the 0.3K detector baffling, and fourth class rays go backwards from the detector into a 1K cavity. Only the first class rays are a substantial load for the detector. This may be seen by considering the next most significant source: the fourth class rays. On a 1 mm $\times$ 1mm detector pixel area, a hemisphere of 1K black body deposits 0.06 pW. As will be shown, this is a small fraction of the overall loading and may be neglected, along with loading from second and third class rays, for the purposes of this work.

The radiation loading from the sky, the atmosphere, and all the elements of the telescope and receiver along the optical path can be expressed in terms of an overall intensity $S_{det}(\nu)$ seen by the detectors. If all the sources seen by the detector were numbered from one to N, where one corresponds to the CMB and N to the final lens, then the overall intensity can be calculated as

$$S_{det}(\nu) = S_N(\nu) + \sum_{i=1}^{N-1} S_i(\nu) \prod_{k=i+1}^{N} T_k(\nu) \tag{2.3}$$

where $S_i$ and $T_i$ are the intensity and transmission coefficient, respectively, for the $i^{th}$ element. The transmission coefficient in this equation accounts for both absorption and reflection. The intensity is viewed by the detector through a solid angle with a half opening of 35°. Finally, calculations suggest that the detector absorption efficiency $\eta_{det}$ can be as high as 90%.

It remains to determine $S_i$ and $T_i$ for each element in the optical chain shown in Figure 2.4. The mirrors, window and lenses can be considered thermal sources characterized by a gray body spectrum with opacity $\tau$ such that

$$S(\nu) = B_\nu(T)(1 - \exp(-\tau(\nu)) \tag{2.4}$$

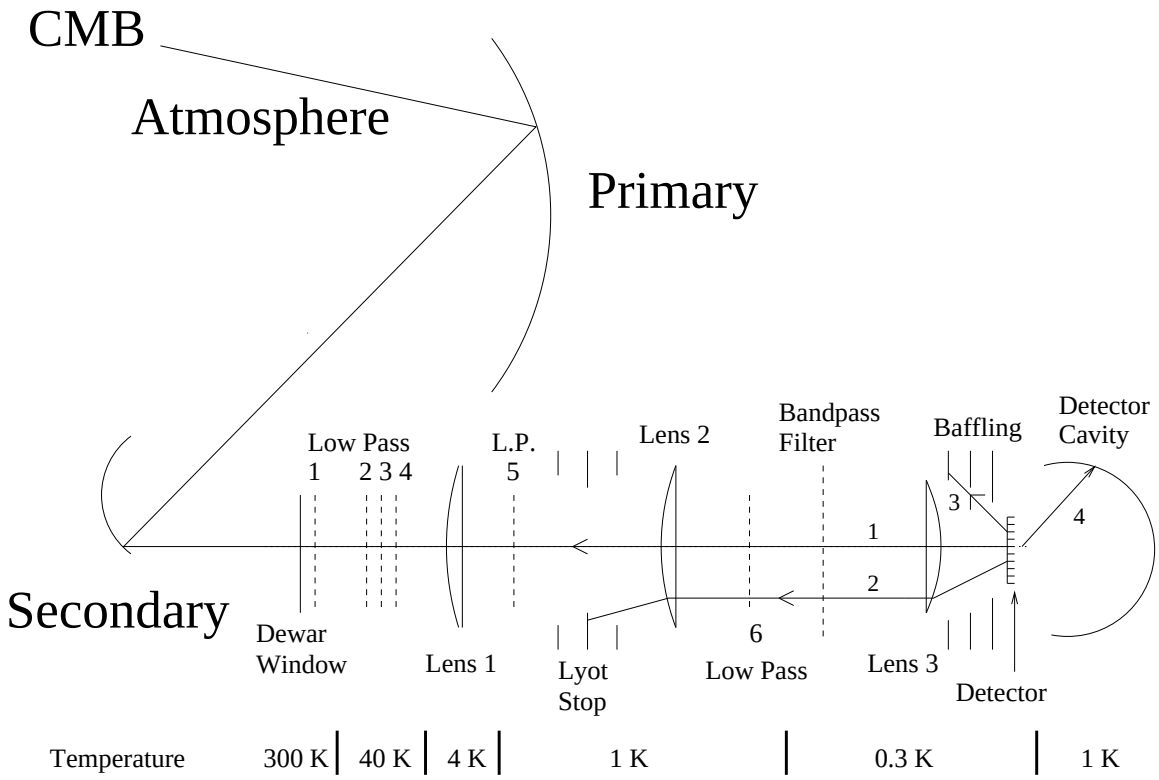


Figure 2.4: **ACT Optical Schematic.** Once through the atmosphere, the cosmic signal is focused by ACT's primary and secondary mirrors into the receiver. The signal traverses various levels of cryogenic optics until it is finally focused on the ACT receiver. Temperatures listed at the bottom of the figure indicate the cryogenic temperature stage at which each optical element sits, from the 300 K receiver window to the final 0.3 K lens. Elements marked Low Pass or L.P. are low pass optical filters. The rays drawn emanating from the detector represent the four unique lines of site from the detector to the outside world or the cryostat. Only rays which pass through the cryostat and terminate on the sky (e.g., ray number one) contribute significantly to radiation loading on the detector.

and

$$T(\nu) = \exp(-\tau(\nu)). \tag{2.5}$$

For the aluminum mirrors the opacity is given by

$$\tau(\nu) = 4\sqrt{\frac{\pi\epsilon_o\nu}{\sigma}}, \tag{2.6}$$

where $\epsilon_o$ is the permitivity of free space, and the conductivity $\sigma$ of aluminum is taken to be $1.5 \times 10^7$ S/m [21]. For the window and lenses, the opacity is described by that of a dielectric:

$$\tau(\nu) = \frac{2\pi t}{\lambda'} \tan\delta, \tag{2.7}$$

where $\lambda'$ is the wavelength of light in the dielectric, $\tan\delta$ is the loss tangent, and t is the thickness of the material. For the 3.2 mm thick polyethylene window, the index of refraction n is 1.52, and the loss tangent is taken to be 0.0004 (based on measurements at 300K) [21]. The silicon lenses are composite structures. A 0.25 mm layer of polyimide film is attached to each silicon lens by 20 $\mu$m of epoxy. Measurements of the index of refraction and loss tangent have been made for all three materials at room temperature as reported in [22]. The findings are shown in Table 2.2. Measurements of silicon's optical properties at cryogenic temperatures find the loss tangent to be much less than its room temperature value [34]. For this reason, the present study estimates the loss tangent of silicon at the cryogenic lens temperatures to be $0.0001(\nu/150\text{GHz})^{-1}$ – a factor of two lower than the value measured at room temperature. The layer of polyimide on the silicon lenses acts as an antireflection coating which limits reflected power to less than 1.5% [22]. The receiver window thickness will be tuned to minimize reflections at similarly low levels.

The final optical elements to consider are the filters. Low pass filters one, two, and four are neutral density filters having better than 99.5% transmission to $\sim$ 10 THz. The remaining three low pass filters are reflective, have cut-offs which approach

| Material | Thickness t (mm) | Refraction Index n | Loss tangent $\tan\delta$ |
|---|---|---|---|
| Polyethylene (Window) | 3.2 | 1.52 | 0.0004 |
| Polyimide (Lens AR Layer) | 0.25 | 1.84 | $0.008(\nu/150)^{0.52}$ |
| Epoxy (AR Adhesive) | 0.02 | 1.68 | $0.023(\nu/150)^{0.52}$ |
| Silicon (Lens 1, 2, 3) | 12.0, 9.5, 16.0 | 3.42 | $0.00022(\nu/150)^{-1}$ (0.0001) |

Table 2.2: **Dielectric properties of ACT Optics.** Polyethylene is the receiver window material. The ACT silicon lenses are coated on both sides by a 0.25 mm antireflection (AR) layer of polyimide attached by 20 $\mu$m thick epoxy. The multiple thicknesses for silicon are listed from left to right for lenses 1, 2, and 3, respectively. All properties are quoted for room temperature. Because it has been shown that absorption of microwaves in silicon decreases strongly with temperature, the loading calculation for the cryogenic lenses assumes the loss tangent to be $0.0001(\nu/150\text{GHz})^{-1}$ [34]. The frequency $\nu$ in the expressions for loss tangent is in terms of gigahertz. The measurement of the dielectric properties of the lens materials is reported in [22]. The properties of polyethylene (and many other dielectrics) are collected in [21].

the signal band, and reject in-band radiation at the 5% level. The band pass filters are reflective and ultimately define the signal band. In the signal band, the band pass filters are 75-85% transmissive. Based on limited knowledge of the filter's material properties, it will be assumed that the filters do not radiate appreciably in the signal band. Table 2.3 tabulates the Rayleigh-Jeans Temperatures and transmission coefficients for all the ACT Optics.

Table 2.3 shows that no appreciable loading comes from the cryogenic optics inside the receiver. Besides the atmosphere and the cosmic signal, the only non-negligible contributors to the overall radiation load are the telescope mirrors and the dewar window. This result suggests that the total intensity $S_{det}$ seen by the detector can be well approximated by

$$S_{det} \approx T_{Rx}(S_{CMB}T_{atm} + S_{atm} + S_{tel} + S_{win}), \tag{2.8}$$

where $T_{Rx}$ is the combined transmission of all cryogenic receiver optics, $T_{atm}$ is the atmospheric transmission, and $S_{CMB}$, $S_{atm}$, $S_{tel}$, and $S_{win}$ are the intensities of the

| Source | Transmission | | | $T_{RJ}$ (K) | | |
|---|---|---|---|---|---|---|
| | 147 GHz | 215 GHz | 278 GHz | 147 GHz | 215 GHz | 278 GHz |
| CMB | 0 | 0 | 0 | 0.57 | 0.24 | 0.1 |
| Atmosphere | 0.96 | 0.93 | 0.88 | 8.5 | 17.6 | 29.8 |
| Primary | 1.00 | 1.00 | 1.00 | 0.55 | 0.65 | 0.75 |
| Secondary | 1.00 | 1.00 | 1.00 | 0.55 | 0.65 | 0.75 |
| Window | 0.995 | 0.99 | 0.99 | 1.6 | 2.3 | 3.0 |
| LP1 | 1.00 | 1.00 | 1.00 | 0.0 | 0.0 | 0.0 |
| LP2 | 1.00 | 1.00 | 1.00 | 0.0 | 0.0 | 0.0 |
| LP3 | 0.97 | 0.95 | 0.94 | 0.0 | 0.0 | 0.0 |
| LP4 | 1.00 | 1.00 | 1.00 | 0.0 | 0.0 | 0.0 |
| Lens 1 | 0.96 | 0.93 | 0.915 | 0.05 | 0.05 | 0.05 |
| LP5 | 0.97 | 0.95 | 0.94 | 0.0 | 0.0 | 0.0 |
| Lens 2 | 0.96 | 0.93 | 0.915 | 0.0 | 0.0 | 0.0 |
| LP6 | 0.97 | 0.95 | 0.94 | 0.0 | 0.0 | 0.0 |
| BP | 0.85 | 0.75 | 0.78 | 0.0 | 0.0 | 0.0 |
| Lens 3 | 0.96 | 0.93 | 0.915 | 0.0 | 0.0 | 0.0 |
| Totals | 0.65 | 0.49 | 0.43 | 13.4 | 21.5 | 34.4 |

Table 2.3: **Transmission and RJ Brightness of ACT Sources and Optics.** Listed in the table are the emitted intensity, in terms of Rayleigh-Jeans brightnesses and the transmission efficiency of each element in the ACT optical chain shown (Figure 2.4). All values listed as zero are either assumed to be zero (e.g., filter emission) or are zero when rounded to the indicated precision. Totals may not exactly equal the sum of the elements listed in the corresponding column due to round-off error. Of particular significance is the result that no appreciable amount of radiation seen by the detector comes from the cryogenic optics. In this way, the receiver optics may be treated purely as a filter. The only significant sources of loading are the atmosphere, the receiver window, the telescope mirrors, and the CMB, in order of prevalence. The atmospheric brightness corresponds to the median loading as experienced on winter evenings. Even considering the lowest level of atmospheric loading during winter mornings, the atmosphere would dominate emission from the telescope and receiver in all signal bands. It follows that the CMB intensity will be attenuated by approximately 50% by the atmosphere and optics. An additional detector absorption efficiency factor will increase the effective attenuation. Achievable detector efficiencies have been calculated near the 90% level.

CMB, atmosphere, telescope mirrors, and the receiver window, respectively. The overall transmission of the cryogenic receiver optics is dominated by reflection from filters and absorption in the lenses. Given $S_{det}$, the total radiated power absorbed by pixel with area A is

$$P_\gamma = \eta_{det} \times S_{det} \times \Delta\nu \times A \times 2\pi \int_0^{\theta_o} d\theta \sin(\theta)\cos(\theta), \tag{2.9}$$

where $\eta_{det}$ is the detector absorption efficiency, $\Delta\nu$ is the bandwidth, and $\theta_o$ is the characteristic maximum angle, taken as 35°, by which rays from the sky reach the detectors. The factor of $\cos(\theta)$ in the integrand for $P_\gamma$ accounts for the projected area of the pixel ($A\cos(\theta)$) for light striking away from the pixel normal. Besides the total power $P_\gamma$ absorbed by a pixel, another important parameter is the conversion factor translating cosmic intensities to power at the detector, the telescope response:

$$\frac{\Delta P_\gamma}{\Delta S_{CMB}} = \frac{\Delta P_\gamma}{\Delta S_{det}} \frac{\Delta S_{det}}{\Delta S_{CMB}} \approx T_{Rx} T_{atm} \times \eta_{det} \times \Delta\nu \times A \times 2\pi \int_0^{\theta_o} d\theta \sin(\theta)\cos(\theta). \tag{2.10}$$

Table 2.4 lists all the parameter values involved in solving for $S_{det}$, $P_\gamma$, and $\Delta P_\gamma/\Delta S_{CMB}$ in the three ACT bands. Table 2.5 gives $P_\gamma$, and $\Delta P_\gamma/\Delta S_{CMB}$ under the atmospheric loading conditions encountered in the Atacama throughout the year.

## 2.5 Discussion

By knowing the telescope response to intensities on the sky (Table 2.5), one can compute the RMS signal power on a single detector due to the CMB anisotropies compiled in Table 2.6. The result is shown in Figure 2.5. In the next chapter, it is shown how these signal powers are converted by the detectors into electric current and how the noise power in the detectors compares to the CMB signal. Table 2.6 lists the anisotropy signal levels graphed in Figure 2.5. The signals in Figure 2.5 and Table 2.6 were computed for the median atmospheric opacity in the winter evenings

| Parameter | Band | | |
|---|---|---|---|
| | 147 GHz | 215 GHz | 278 GHz |
| $S_{CMB}$ (pW/GHz/sr/mm$^2$) | 0.0038 | 0.0034 | 0.0024 |
| $T_{atm}$ | 0.96 | 0.93 | 0.88 |
| $S_{atm}$ (pW/GHz/sr/mm$^2$) | 0.07 | 0.25 | 0.74 |
| $S_{tel+win}$ (pW/GHz/sr/mm$^2$) | 0.02 | 0.05 | 0.1 |
| $T_{Rx}$ ($T_{filt}$) | 0.68 (0.78) | 0.52 (0.64) | 0.49 (0.66) |
| $S_{det}$ (pW/GHz/sr/mm$^2$) | 0.06 | 0.16 | 0.42 |
| A (mm$^2$) | 1.1 | 1.1 | 1.1 |
| $\Delta\nu$ (GHz) | 23 | 23 | 30 |
| $\eta_{det}$ | 0.9 | 0.9 | 0.9 |
| $\int$ d$\Omega$ cos$\theta$ (sr) | 0.6 | 0.6 | 0.6 |
| $P_\gamma$ (pW) | 0.8 | 2.1 | 7.1 |
| $\Delta P_\gamma / \Delta S_{CMB}$ (GHz sr mm$^2$) | 8.4 | 6.3 | 7.3 |

Table 2.4: **Essential Band Parameters.** This table compiles the parameters needed to compute the radiation loading ($P_\gamma$) and telescope response ($\Delta P_\gamma / \Delta S_{CMB}$ (GHz sr mm$^2$) from Equations 2.9 and 2.10, respectively. The telescope response is the change in radiation power for a change in cosmic intensity. The atmospheric conditions used for the calculation correspond to the median conditions on winter nights as listed in Table 2.1. The various transmission coefficients and emission intensities are from Table 2.3. The pixel area is for square pixels 1.05 mm on a side. The angular integral is over a solid angle with a 35° half opening. The cos$\theta$ factor in the integral accounts for the diminished area of the pixel for radiation striking the detector away from the normal. Finally, the fraction of radiation incident on the detector pixel which is absorbed as thermal power is given by the detector efficiency $\eta_{det}$. This fraction has been calculated to be in the neighborhood of the value listed $\sim 0.9$. The loading and response computed for all atmospheric conditions from Table 2.1 are listed in Table 2.5.

| Seasonal and Diurnal Quartiles for Loading $P_\gamma$ and Response $\Delta P_\gamma/\Delta S_{CMB}$ (pW, GHz sr mm$^2$) | | | |
|---|---|---|---|
| Quartile | Summer Evening | | |
| | 147 GHz | 215 GHz | 278 GHz |
| 25% | 0.85 / 8.4 | 2.3 / 6.3 | 7.8 / 7.2 |
| 50% | 1.3 / 8.2 | 3.8 / 5.9 | 12.5 / 6.5 |
| 75% | 2.2 / 7.7 | 6.8 / 5.1 | 22 / 5.0 |
| Quartile | Summer Morning | | |
| | 147 GHz | 215 GHz | 278 GHz |
| 25% | 0.7 / 8.5 | 1.7 / 6.4 | 5.9 / 7.5 |
| 50% | 1.0 / 8.3 | 2.9 / 6.1 | 9.9 / 6.9 |
| 75% | 1.8 / 7.9 | 5.6 / 5.4 | 18 / 5.6 |
| Quartile | Winter Evening | | |
| | 147 GHz | 215 GHz | 278 GHz |
| 25% | 0.65 / 8.5 | 1.6 / 6.5 | 5.4 / 7.6 |
| **50%** | **0.8 / 8.4** | **2.1 / 6.3** | **7.1 / 7.3** |
| 75% | 1.0 / 8.3 | 3.0 / 6.1 | 10 / 6.9 |
| Quartile | Winter Morning | | |
| | 147 GHz | 215 GHz | 278 GHz |
| 25% | 0.6 / 8.6 | 1.4 / 6.6 | 4.6 / 7.7 |
| 50% | 0.7 / 8.5 | 1.7 / 6.4 | 5.9 / 7.5 |
| 75% | 0.9 / 8.4 | 2.6 / 6.2 | 8.8 / 7.1 |

Table 2.5: **Detector Loading and Telescope Response.** The detector loading and telescope response are given for the three ACT bands and for different atmospheric conditions subject to diurnal and seasonal trends. Again, we define mornings as 5:00 – 17:00 UTC and winter as June – November The quartiles into which the season/time-of-day data are subdivided correspond to the distribution of atmospheric opacities at the site (Table 2.1). The detector loading is the sum of the power incident on a single detector pixel from all radiation sources listed in Table 2.3. The telescope response is the change in radiation power absorbed into the pixel for a change in cosmic power (e.g., from sweeping the telescope across anisotropies in the CMB). The radiation loading is seen to be 1-2, 2-4, and 4-12 pW in the 147, 215, 287 GHz bands, respectively. The telescope response is more stable, with not much more than 15% variation around 8.4, 6.3, and 7.3 GHz sr mm$^2$ in the 147, 215, 287 GHz bands, respectively. The median loading and response for winter evenings (in bold) is used in Table 2.4 as an example of how to compute the loading and response from Equations 2.9 and 2.10. The telescope response for mean winter evening conditions are also used to show the signal power from CMB anisotropies in Figure 2.5 and Table 2.6.

as given by Table 2.5. Perusal of Table 2.5 shows that the telescope response to the cosmic intensity does not change by much more than 15% throughout the year within any given band. This is due to the fact that the atmospheric absorption is weak at the telescope site. The receiver acts as *the* bottleneck for cosmic signal transmission: the combination of reflection from filters and absorption in lenses in the receiver results in approximately 50% transmission of the cosmic signal power (Table 2.3) whereas the atmosphere transmits $\sim 90\%$. The receiver transmission should be constant throughout the year; if this were not the case then significant fluctuations in the telescope response would result. The atmospheric transmission, on the other hand, fluctuates by a factor of two or more and would result in substantial telescope response changes but for the desert atmosphere's unparalleled transparency.

A second piece of information critical for understanding the operation of the detectors is the background radiation load throughout the observing year. This is compiled alongside the telescope response in Table 2.5. Besides the temperature of the detector, the background loading power sets the overall noise level and therefore the sensitivity of the detector. There are two reasons for this. First, the flux of photons onto the detector fluctuates statistically to give a noise level ten to one hundred times the signal levels shown in Figure 2.5. Second, the power into the detector from the background radiation requires a thermal link to a heat sink which conducts at least as much heat from the detector as is put on by the background radiation. By setting the scale of the thermal link, the background power establishes the second dominant source of detector noise: fluctuations in the phonon flux (or other thermal carrier flux) down the thermal link. The results from this chapter set the background level for the 147, 215, and 278 GHz bands from 1-2, 2-4, and 4-12 pW, respectively. The significant fluctuation in overall loading follows from the atmosphere being the dominant source of loading even under the most transparent atmospheric observating

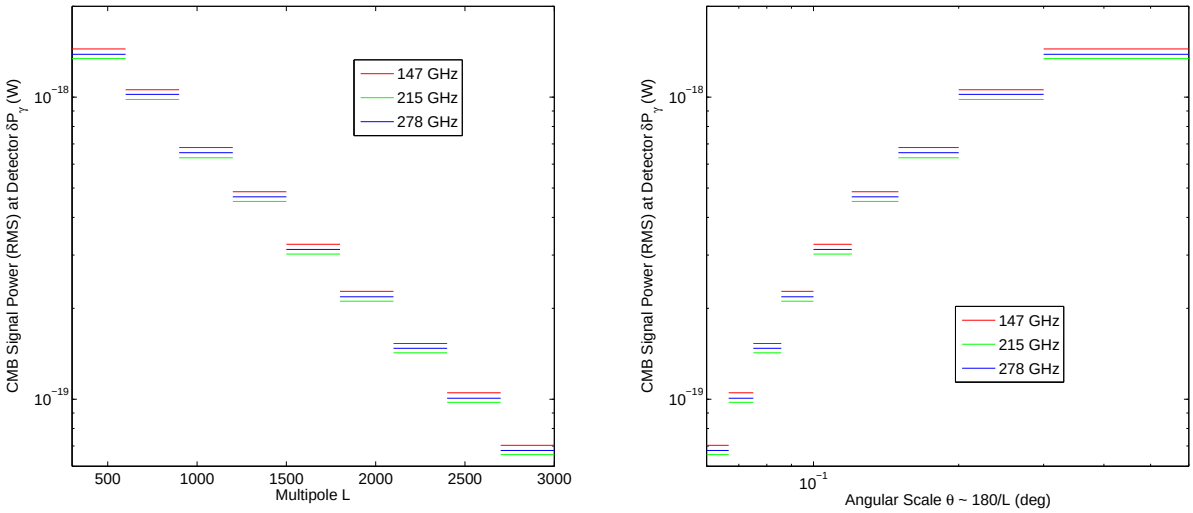


Figure 2.5: **CMB Anisotropy Signal Power at the Detectors.** The telescope response numbers in Table 2.5 convert a given fluctuation in sky intensity into a fluctuation in radiation power absorbed by a single detector. Therefore, the telescope response factors can be used to derive the signal power in a detector from the RMS intensity fluctuation levels of the CMB anisotropy in Figure 1.6 and Table 1.1. The resulting CMB anisotropy RMS signal power is plotted above for the ranges of multipoles $\ell$ and corresponding angular scales $\Delta\Theta$ listed in Table 2.6.

| $\Delta\ell$ | $\Delta\Theta$ (deg) | $\delta P_{\gamma,147}$ (W) | $\delta P_{\gamma,215}$ (W) | $\delta P_{\gamma,278}$ (W) |
|---|---|---|---|---|
| 300-600 | 0.60-0.30 | 1.44E-18 | 1.34E-18 | 1.39E-18 |
| 600-900 | 0.30-0.20 | 1.06E-18 | 9.85E-19 | 1.02E-18 |
| 900-1200 | 0.2-0.15 | 6.82E-19 | 6.33E-19 | 6.55E-19 |
| 1200-1500 | 0.15-0.12 | 4.87E-19 | 4.52E-19 | 4.68E-19 |
| 1500-1800 | 0.12-0.10 | 3.26E-19 | 3.02E-19 | 3.13E-19 |
| 1800-2100 | 0.10-0.086 | 2.27E-19 | 2.11E-19 | 2.19E-19 |
| 2100-2400 | 0.086-0.075 | 1.53E-19 | 1.42E-19 | 1.47E-19 |
| 2400-2700 | 0.075-0.067 | 1.05E-19 | 9.75E-20 | 1.01E-19 |
| 2700-3000 | 0.067-0.06 | 7.04E-20 | 6.53E-20 | 6.77E-20 |

Table 2.6: **Detector RMS Signal Power from Primary CMB Anisotropies.** This table lists the data that are plotted in Figure 2.5. For a given angular scale, the signal power ($\delta P_{\gamma,147}$, $\delta P_{\gamma,215}$, and $\delta P_{\gamma,278}$) gives the difference in detector signal power from adjacent regions of the CMB. For instance, two adjacent regions of the CMB, $\sim 0.065^\circ$ in diameter, should on average load a given detector differently by $7 \times 10^{-20}$ W in the 145 GHz band.

conditions (see Table 2.3). The atmospheric brightness fluctuates by a factor of two or more throughout the year as shown in Figure 2.3 and so follow the fluctuations in overall loading.

## 2.6 Acknowledgements

The loading calculation presented in this chapter is a review and update of original calculations presented in [28]. The work is updated based on conversations with Robert Thornton of University of Pennsylvania, who is in charge of the mechanical design of the receiver optics; Joe Fowler of Princeton, who is the lead scientist for the ACT receiver optics; and Judy Lau of Princeton, who has contributed significantly to both the optical and mechanical design of the entire ACT camera. Suzanne Staggs calculated expected detector absorption efficiencies. The ACT filter bandpasses were measured by Carole Tucker at Cardiff. Sarah Marriage (my sister) helped find the recipe for attaching polyimide film to silicon.

# Chapter 3

# The ACT Detector

## 3.1 Introduction: Converting Radiation to Electric Current

Figure 3.1 shows ACT bolometers configured as a two dimensional array to be positioned in the ACT focal plane. As detailed in the subfigure, each bolometer has a 1.05 mm x 1.05 mm square of 1.4 $\mu$m thick silicon. The silicon has been implanted with ions to make the pixel mildly conductive and therefore able to absorb radiation (Chapter 2). A 75 $\mu$m x 80 $\mu$m thin-film MoAu superconductor is printed atop the silicon.[1] The bolometer is operated at T = 0.525 mK at the film's superconducting transition (i.e., at the critical temperature $T_c$ of the film). On the transition, the film resistance increases from 0 $\Omega$ (superconducting) to 21 m$\Omega$ (normal state resistance) as the temperature increases only a few millikelvin.[2] Therefore, when the temperature of the bolometer fluctuates due to changes in absorbed power from radiation, the resistance of the superconductor fluctuates accordingly. If a voltage is put across the

[1]The dimensions of the MoAu film depend on the superconductor recipe, but the total area of film is similar from recipe to recipe (Chapter 4).

[2]The critical temperature and normal state resistance depend on the MoAu film recipe (Chapter 4).

MoAu film, then the fluctuations in resistance $\delta$R can be measured by the current fluctuation $\delta$I $\propto$ -$\delta$R. Thus, the bolometer is essentially a device for changing fluctuations in power from absorbed radiation into measurable electric currents. Because an ACT bolometer detects radiant power using a superconductor on transition, the device is called a Transition Edge Sensor (TES).

In addition to the current response (gain and bandwidth) of the detector to radiant power, two other important bolometer attributes are the device noise and negative electro-thermal feedback. The device noise power and noise power from absorbed radiation – the Noise Equivalent Power (NEP) – obscure the cosmic signal. The instrument's sensitivity to the cosmic signal is thus increased by choosing a bolometer with low device noise. The sub-Kelvin operating temperature of the TESs is ultimately what drives down the noise of the detector. The second important attribute, negative electro-thermal feedback (NETF), stabilizes and increases the bandwidth of the bolometer. NETF arises because the slope of the transition dR/dT is positive and the device is voltage-biased such that $P_J$=$V^2$/R (fixed V) is the Joule power dissipated in the biased TES. Given a fluctuation in power $\delta$P (e.g., from radiation or bias power), the device will change temperature $\delta$T $\propto$ $\delta$P. Because dR/dT $>$ 0, the resistance will change $\delta$R $\propto$ $\delta$T, and the Joule power will respond $\delta P_J \propto$ -$\delta$R because of the voltage-bias. Therefore, $\delta P_J \propto$ -$\delta$P and the device self-cools (self-heats) in response to an increase (decrease) in temperature. On the other hand, if the device were current-biased and $P_J$=$I^2$R (fixed I), the Joule power would increase (decrease) with an increase (decrease) in total power on the pixel. This would cause positive electro-thermal feedback, and the unstable bolometer would self-heat or self-cool off the transition. Finally, because the response of Joule heating to a change in thermal power can be much faster than the intrinsic thermal response of the device silicon, the bolometer can respond more quickly to changes in signal power given NETF. In

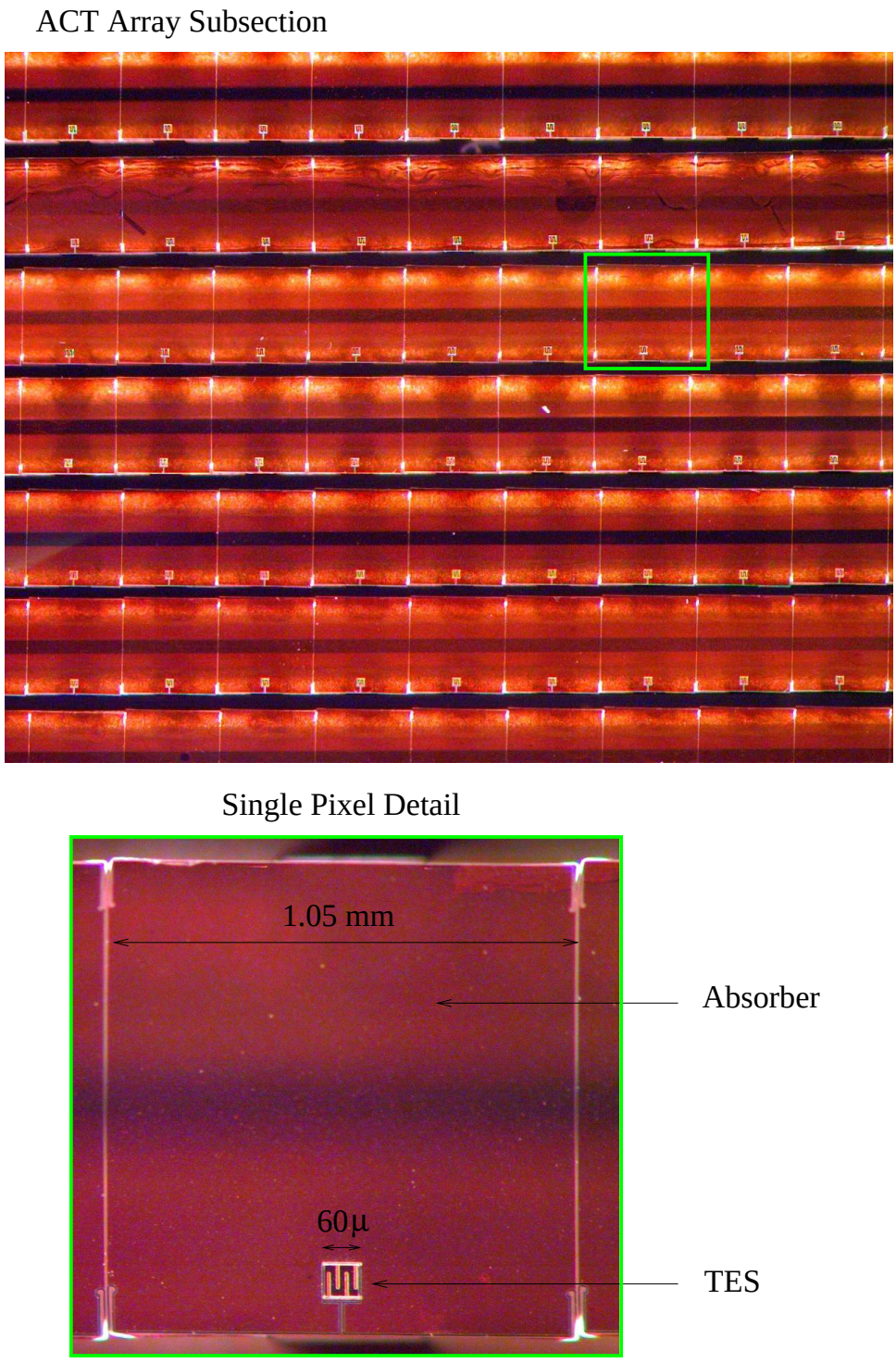


Figure 3.1: **ACT Bolometers.** ACT bolometers are arranged in a two dimensional array (top). Each bolometer pixel consists of a 1.05 x 1.05 mm square of ion-implanted silicon for absorbing radiation. The TES thermistor is positioned at the bottom-center of the pixel. Radiation is absorbed, and the pixel temperature increases. The TES resistance increases with temperature. A stiff voltage is applied across the TES such that resistance changes are measured by the corresponding changes in current through the TES. The pixels appear transparent because they are only 1.4 $\mu$m thick. Narrow legs extend behind the pixels and act as a connection to a cold thermal bath as well as a pathway for wiring. The array shown was assembled and photographed by Judy Lau of Princeton University.

other words, NETF increases the device bandwidth.

## 3.2 The TES as an Electro-thermal System

The simplest electro-thermal model of TES behavior is described by the two circuits shown in Figure 3.2. The thermal circuit consists of a lumped heat capacity C (TES film and absorber silicon) at temperature T isolated from a thermal bath at temperature $T_b < T$ by a weak link of the thermal conductance G(T). The bolometer is heated by the Joule power $P_J$ and absorbed radiation $P_\gamma$, and power $P_c$ is conducted away down the weak link. Not pictured is noise power $P_n$ which is small compared to the other sources. The electrical circuit consists of the TES MoAu film with resistance R in series with an inductor with inductance L. The inductor transduces the current I through the TES into a magnetic field which in turn is converted to a voltage by a series of superconducting quantum interference device (SQUID) amplifiers. Parallel with the TES and inductor is a shunt resistor of resistance $R_s$. The parallel circuit is fed a current $I_{DB}$ by a stiff current supply.

The equation describing the thermal circuit in Figure 3.2 is

$$C\frac{dT}{dt} = P_J + P_\gamma + P_n - P_c. \tag{3.1}$$

The Joule power $P_J$ is $I^2R$. Power from absorbed radiation $P_\gamma$ was computed in Chapters 1 and 2. Noise power will be described in Section 3.5. Thermal conduction $P_c$ is parametrized by

$$P_c = \int_{T_b}^{T} G(T)dT = K(T^n - T_b^n). \tag{3.2}$$

With phonons (which are the main conductor of heat in undoped silicon), the thermal conductivity may be parametrized $g \approx c_v c\ell/3$ where $c_v$ is the specific heat of the phonons, c is the lattice sound speed, and $\ell$ is the mean free path of phonons (e.g.,

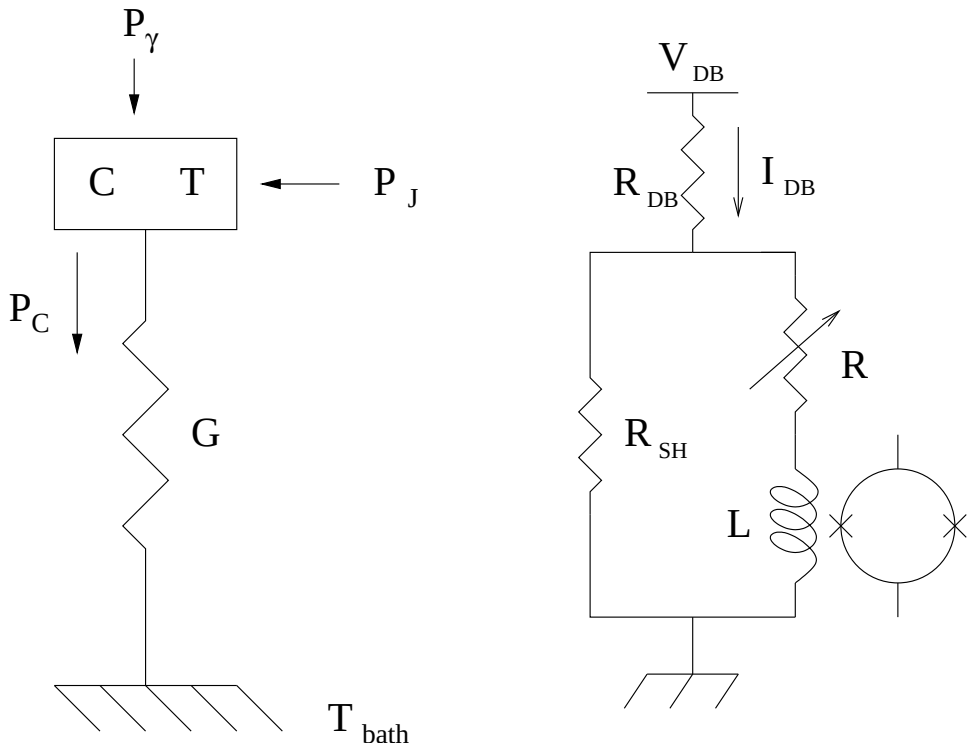


Figure 3.2: **Electro-thermal Circuit of a Bolometer.** The bolometer is an electro-thermal device. The thermal circuit (left) consists of the pixel with heat capacity C at temperature T connected by a weak thermal link G to a thermal bath at temperature $T_b < T$. Power is put into the pixel by absorbed radiation $P_\gamma$ and the Joule power $P_J$ for biasing the bolometer. The power $P_c$ is conducted from the pixel by the weak link G to the bath. The electrical circuit (right) consists of a voltage $V_{DB}$ which is transformed into a current $I_{DB}$ by a large resistor $R_{DB} \gg R_{SH}$, R. The current flows through a circuit with a shunt resistor $R_{SH}$ in parallel with the TES resistor R and the SQUID input inductor L. Physically, the TES resistor is on the pixel and the shunt resistor and SQUID are connected to the thermal bath. For $R \gg R_{SH}$, the TES resistor R is voltage biased. Fluctuations in TES resistance R result in fluctuations in current which are read out magnetically with the pick-up inductor L of the DC SQUID amplifier.

[1]).[3] At cryogenic temperatures, $\ell$ grows until it is limited by, for instance, the size of the sample. In the Debye Model of lattice oscillations, the sound speed is constant and the specific heat is proportional to $T^3$. Therefore, integrating the phonon thermal conductivity from T to $T_b$ gives a temperature exponent of n=4 for phonons at cryogenic temperatures in Equation 3.2. In fact, in this ballistic limit ($\ell$ not dependent on temperature), a direct comparison of phonon conduction can be drawn with the Stefan-Boltzmann Law for photons which has a $T^4$ dependence. The coefficient K in Equation 3.2 depends both on the material (e.g., through the lattice sound speed for phonons) and the geometry of the device (e.g., through the mean free path for phonons). The case of phonons is important for the ACT detectors. Four silicon legs, 1.4 $\mu$m thick and 5-20 $\mu$m wide, extend from the ACT pixel (Figure 3.1) to the cold bath. Figure 3.3 shows plots of measured thermal properties for the silicon legs of various widths.

The equation describing the electrical circuit in Figure 3.2 can be obtained by setting the voltage drop across the shunt resistance $R_s$ equal to the voltage drop across the TES resistance R in series with the inductance L:

$$L\frac{dI}{dt} + IR = (I_{DB} - I)R_s. \tag{3.3}$$

Equations 3.1 and 3.3 describe the dynamics of the TES parameters I, T, and R. If the shape of the transition R(I,T) were known, then it would be a straightforward exercise to solve the pair of ordinary differential equations. This is in general not the case (certainly not for the ACT detectors), and R(I,T) must be investigated experimentally to characterize the system. Figure 3.4 shows a schematic of a transition. The transition is characterized by a critical temperature $T_c$ and critical current $I_c$ above which the TES is in the normal state. In practice, the TES $I_c$ is well above

[3]Dimensionally G(T) $\sim$ g(T) $\times$ A / L where A is the cross-sectional area of the sample normal to both the power flow and the length L.

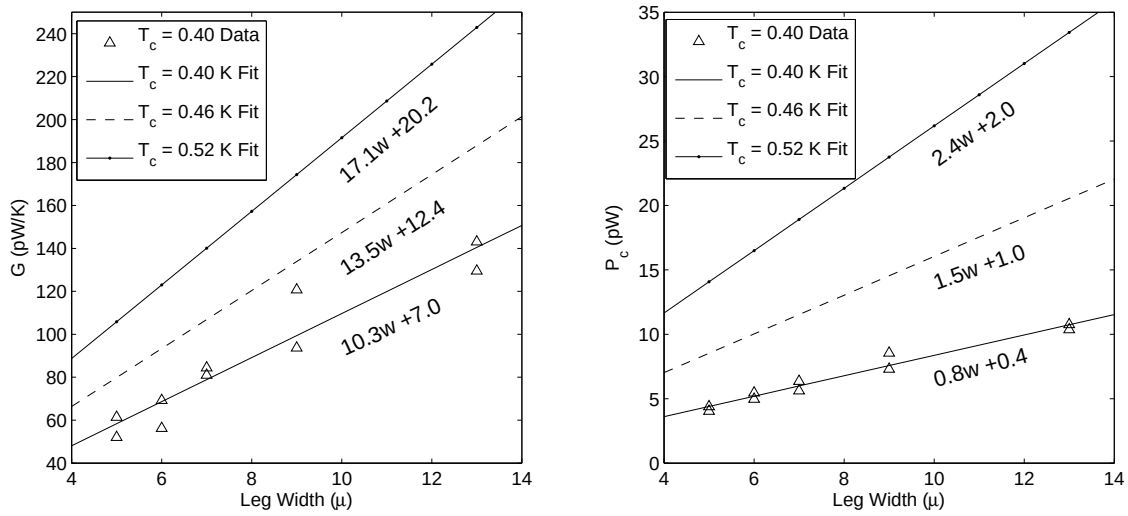


Figure 3.3: **Thermal Conduction of ACT Bolometers.** The thermal conductance G and conducted power $P_c$ are plotted for ACT bolometers with various leg widths. For each leg width two devices were tested. The tests give conductance parmeters n and K from Equation 3.2. The data from the tests are plotted for $T_c = 0.40$ K. Given the scaling relations in Equation 3.2, the results can be extrapolated to describe devices with any $T_c$. The best fit lines to the data are given for critical temperatures of 0.40 K, 0.46 K, and 0.52 K. The thermal conductance may be fit as a linear function of leg width, consistent with geometric scaling arguments. The conductance measurement does not constrain n and K very well, but device parameters such as G and $P_c$ are more robustly determined. The devices measured here show $n \sim 3$, but further work has resulted in conduction exponents closer to 4. Corresponding K coefficients can be solved from n and the G data. $T_b$ is taken as 0.30 K for the $P_c$ data. The results above were first published in [29]. A description of the thermal conduction measurements is given in Chapter 5.

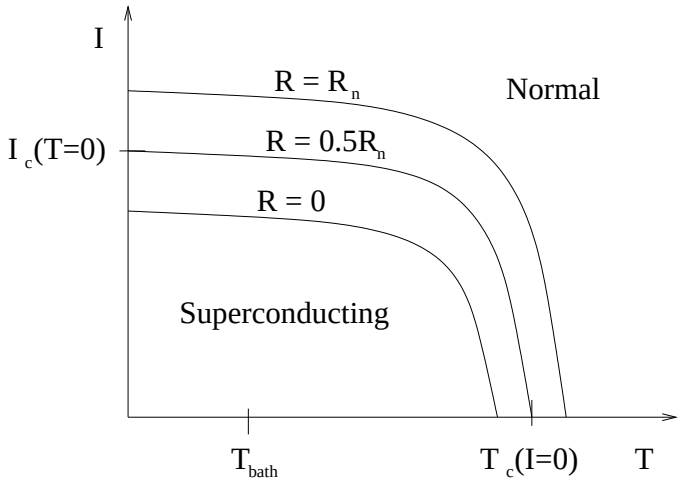


Figure 3.4: **Superconducting Transition Schematic.** The superconducting transition R(I,T) features a critical temperature $T_c$ and a critical current $I_c$ above which the TES is in the normal state. For ACT TESs, $T_c \approx 0.5$K, and $R_n \approx 0.02\ \Omega$, although these values depend on the fabrication which is not yet finalized. The $I_c$ of ACT devices is substantially higher than operating currents such that the resistance has significantly more dependence on T than on I. An illuminating set of transition diagrams, similar to the above diagram, can be found in [24].

the operating current such that the temperature dependence of the TES will be much more significant than the current dependence.

## 3.3 Equilibrium and Biasing the TES

At equilibrium (dT/dt=0), Equation 3.1 describing the thermal circuit becomes

$$I_o^2 R_o + P_{\gamma,o} = P_{c,o} = K(T_o^n - T_b^n), \tag{3.4}$$

where 'o' subscripts have been used to denote zero-order equilibrium values ('o' may be taken to stand for "operating point"). Equation 3.4 states that power flow into the bolometer on the left hand side must equal power flow out on the right hand side

at equilibrium. For the electrical circuit, dI/dt=0, and Equation 3.3 reduces to

$$I_o = \frac{I_{DB}}{1 + R_o/R_s}. \tag{3.5}$$

Equation 3.5 is simply the current divider equation. Analogous to the situation in Section 3.2, if the transition function R(I,T) were known, then a third equation would be available:

$$R_o = R(I, T). \tag{3.6}$$

Together, Equations 3.4, 3.5, and 3.6 could be solved to give $R_o$, $I_o$ and $T_o$ under various radiation loadings $P_{\gamma,o}$ expected at the telescope site (Table 2.5). Unfortunately, R(I,T) is unknown, and experiments must be conducted to map out the operating points $R_o$, $T_o$, and $I_o$ (Chapter 5). Figure 3.4 is a schematic of the general features R(I,T).

Although ignorance of R(I,T) makes the exact system of Equations 3.4, 3.5, and 3.6 unsolvable, two common approximations can make the system tractible and therefore provide insight into the operating points of the TES. The first assumption is that the conducted power $P_{c,o}$ in Equation 3.4 is constant across the transition. This is a good approximation if the transition is narrow in temperature so that $T_o$ may be taken to be a characteristic value $\sim T_c$. Also important to the assumption of constant $P_{c,o}$ is that $T_b^n \ll T_o^n$. The second approximation is that the current dependence of R is small, such that $R(I,T) \approx R(T)$. Under these assumptions, Equation 3.6 no longer constrains Equations 3.4 and 3.5 which can be solved for I and R given $P_{\gamma,o}$. If R(T) can be approximated by a suitable function (e.g., given some knowledge of $R_n$ and the temperature span of the transition), then $T_o$ can be estimated as well.

Let $I_{max}$ and $R_{min}$ be the solutions (taking the two assumptions described in the previous paragraph) of Equations 3.4 and 3.5 for $P_{\gamma,o} = 0$. Then the resistance $R_o$

can be expressed as

$$\frac{R_o}{R_{min}} = \frac{1}{2}\frac{(1+R_s/R_{min})^2}{1-P_{\gamma,o}/P_{c,o}} - \frac{R_s}{R_{min}} \pm \frac{1}{2}\sqrt{\left(\frac{2R_s}{R_{min}} - \frac{(1+R_s/R_{min})^2}{1-P_{\gamma,o}/P_{c,o}}\right)^2 - 4\left(\frac{R_s}{R_m}\right)^2}, \tag{3.7}$$

where the $\pm$ is a plus if $R_{min} > R_s$. Likewise, the current $I_o$ is

$$\frac{I_o}{I_{max}} = \frac{1}{2}\left(1+\frac{R_{min}}{R_s}\right) \pm \frac{1}{2}\sqrt{\left(1-\frac{R_{min}}{R_s}\right)^2 + 4\frac{P_{\gamma,o}}{P_{c,o}}\frac{R_{min}}{R_s}}, \tag{3.8}$$

where the $\pm$ is a minus if $R_{min} > R_s$. In the limit that $R_s \ll R_{min}$ (strong voltage bias), Equations 3.7 and 3.8 simplify to

$$\frac{R_o}{R_{min}} = 1/(1-P_{\gamma,o}/P_{c,o}) \tag{3.9}$$

and

$$\frac{I_o}{I_{max}} = 1 - P_{\gamma,o}/P_{c,o}. \tag{3.10}$$

According to Equations 3.9 and 3.10, the resistance tends to infinity and the current tends to zero as $P_{\gamma,o}$ approaches $P_{c,o}$. The resistance however stops increasing, and the current stops decreasing, once the device becomes normal with $R_o = R_n$. The photon loading corresponding to $R_o = R_n$ is called the saturation power $P_{\gamma,sat}$, because the device resistance no longer has a strong dependence on temperature, and therefore on incoming radiation, once $P_\gamma > P_{\gamma,sat}$. In terms of the formalism of Equations 3.7 and 3.8, the saturation power is

$$P_{\gamma,sat} = P_{c,o}\left[\frac{R_n}{R_{min}}\left(\frac{R_s+R_{min}}{R_s+R_n}\right)^2 - 1\right]. \tag{3.11}$$

Using Equations 3.7 and 3.8, Figure 3.5 shows how the operating current and resistance change as a function of $P_{\gamma,o}$ for TES designs featuring different leg widths and different critical currents. The values for the conducted power $P_{c,o}$ corresponding to the different device designs are given in Figure 3.3. The plots in Figure 3.5 also indicate the range of photon loading power to be expected for each band: 1-2 pW,

2-4 pW, and 4-12 pW for the 147 GHz, 215 GHz, and 278 GHz bands, respectively (Chapter 2, Table 2.5). Not surprisingly, the TES current and resistance vary over a smaller ranges as the thermal conductance between the pixel and cold bath is increased. In Section 3.4, it will be shown that the TES response to radiation (gain and bandwidth) are functions of the operating current and resistance. Therefore, to minimize the variation in TES response as the radiation load $P_\gamma$ changes, the bolometer can be designed to have a large conductance to the thermal bath. The large conduction, however, means the device will have a high level of noise due to thermal fluctuaitons between the pixel and the cold bath (Section 3.5).

A final corollary to the assumptions that $P_c, o$ is constant across the transition and the R is negligibly dependent on I, is that for a fixed $P_\gamma$, the product $I_o \times V_o$ (voltage across the TES resistance $R_o$) is a constant. In other words, the current-voltage relation of the TES is decribed by a hyperbola which asymptotes to the current and voltage axes and whose vertex is a function of Joule power ($P_{c,o}$ - $P_{\gamma,o}$). See Chapter 5 for examples of TES I-V characteristics.

## 3.4 Power-to-Current Conversion: Responsivity

A study of the bolometer response to radiation, or responsivity, begins with a linearization of Equations 3.1 and 3.3 for the thermo-electric system. Keeping only first-order terms and working in Fourier space, Equation 3.1 becomes

$$i\omega C\delta T = \delta P_\gamma + \delta P_J - G\delta T. \tag{3.12}$$

Similarly, the linearized electrical equation, Equation 3.3, is

$$i\omega L\delta I = -(R_s + R_o)\delta I - I_o\delta R. \tag{3.13}$$

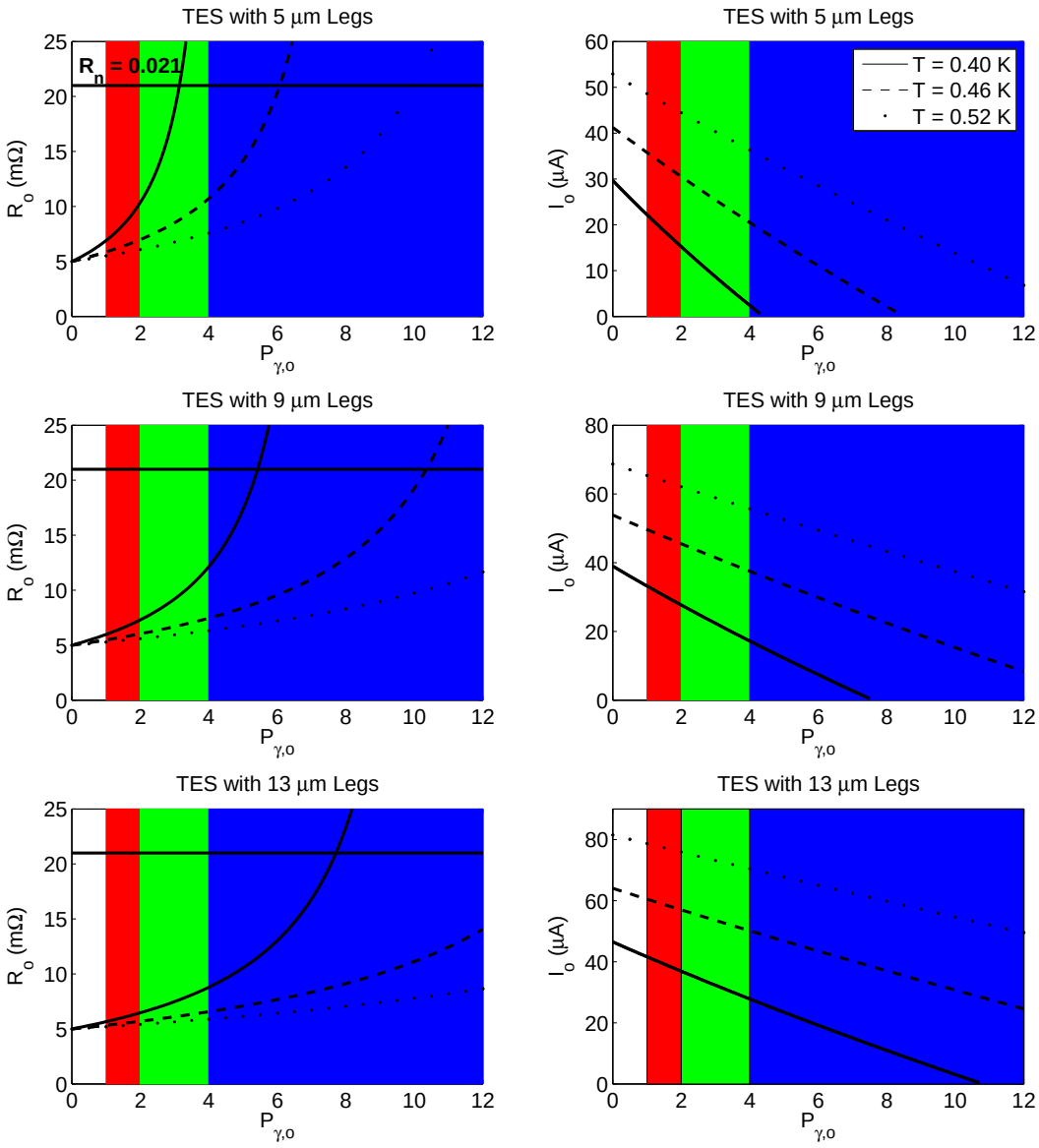


Figure 3.5: **Operating Points for an ACT Detector.** As the operating photon loading power $P_{\gamma,o}$ (x-axes) changes with atmospheric brightness, the detector moves through its operating states, designated in the graphs by $R_o$ and $I_o$ (y-axes). The red, green, and blue regions correspond to loading conditions expected in the ACT 147, 215, and 278 GHz bands, respectively (see Chapter 2). The solid, dashed, and dotted lines correspond to operating points of detectors with critical temperatures of 0.4 K, 0.46 K, and 0.52 K, respectively. Different graphs correspond to detectors with different width legs (5 $\mu$m, 9 $\mu$m, and 13 $\mu$m) connecting the pixel to the cold bath. The responsivity of the device depends on both $R_o$ and $I_o$ with the current $I_o$ playing a fundamental role in determining the bandwidth. Therefore, the variation in $R_o$ and $I_o$ for different detector types under the various loading conditions translate into gain and bandwidth variation. Also drawn in the graphs of $R_o$ versus $P_{\gamma,o}$ is a line corresponding to a device with normal resistance 21 m$\Omega$. The TES saturates (goes normal) at the loading $P_{\gamma,o}$, where the resistance curves meet the normal resistance line – this loading is called the saturation power ($P_{sat}$).

The fluctuation $\delta$R is expanded in terms of current and temperature as

$$\delta R = \frac{\partial R}{\partial T}\delta T + \frac{\partial R}{\partial I}\delta I = \frac{R_o}{T_o}\alpha\delta T + \frac{R_o}{I_o}\beta\delta I. \tag{3.14}$$

Since no functional form is known for R(I,T), $\delta R$ is expanded in terms of the logarithmic derivatives $\alpha$ and $\beta$ which are *a priori* unknown and must be determined by experiments. Equations 3.12, 3.13, and 3.14 comprise a complete system for computing $\delta R$, $\delta I$, and $\delta T$.

To capture the general sense in which the bolometer responds to light, Equation 3.12 may be rewritten

$$\frac{\delta T}{\delta P_\gamma} = \frac{\frac{1}{G}\frac{1}{1+i\omega\tau}}{1 - \frac{\delta P_J/\delta T}{G(1+i\omega\tau)}}, \tag{3.15}$$

where $\tau$ = C/G is the intrinsic thermal time constant of the thin silicon legs. The transfer function expressed in Equation 3.15 can be written in block diagram form as shown in Figure 3.6.[4] Fluctuations in thermal power on the pixel are converted into an initial change in temperature by the factor 1/G(1+i$\omega\tau$). The change in temperature results in a change in Joule power by the electro-thermal feedback (ETF) term $\delta P_J/\delta T$. The change in Joule power feeds back to the pixel as thermal power. The loop gain is

$$\mathcal{L} = \frac{\delta P_J/\delta T}{G(1+i\omega\tau)}. \tag{3.16}$$

Finally, the closed loop temperature output is converted to a current. Equations 3.13 and 3.14 can be solved for the temperature to current conversion:

$$\frac{\delta I}{\delta T} = -\frac{I_o R_o \alpha}{L T_o (i\omega + 1/\tau_{el})}, \tag{3.17}$$

where the electrical time constant $\tau_{el}$ is

$$\tau_{el} = \frac{L}{R_s + R_o(1+\beta)}. \tag{3.18}$$

[4] A treatment of the TES electro-thermal system in terms of block diagrams such as that in Figure 3.6 can be found in [15].

The electro-thermal feedback term is

$$\frac{\delta P_J}{\delta T} = \frac{\delta(I^2 R)}{\delta T} = \frac{P_{J,o}\alpha}{T_o}\left(1 - \frac{R_o(2+\beta)}{L(i\omega + 1/\tau_{el})}\right). \tag{3.19}$$

For the feedback loop in Figure 3.6 to be stable, the loop gain $\mathcal{L}$ must return the Joule power out of phase with the input radiation power. At low frequencies, below the intrinsic and electrical time scales, the loop gain becomes

$$\mathcal{L}(\omega \approx 0) = \frac{P_{J,o}\alpha}{GT_o}\left(\frac{R_s - R_o}{R_s + R_o(1+\beta)}\right). \tag{3.20}$$

It follows that, for the bolometer to be stable, it is necessary that $\mathrm{R}_o > \mathrm{R}_s$ such that the TES is voltage biased. If $\alpha$ were negative, as in the case of semiconductor bolometers, then stability would be achieved with a current bias. Furthermore, if $\beta \approx 0$, then the low frequency current-biased loop gain becomes $\mathcal{L}_I = P_{J,o}\alpha/GT_o$. The term $\mathcal{L}_I$ is prevalent in the literature where it serves as a measure of the strength of ETF. A closer look reveals that $\mathcal{L}_I$ depends on the square of the operating current, the slope $\partial R/\partial T$, and 1/G. Whenever one of these parameters decreases, the electrothermal feedback is weakened. Like $\mathcal{L}_I$, another conceptually useful term which appears repeatedly in the TES response equations is the dynamic resistance at constant temperature:

$$\left.\frac{\partial V}{\partial I}(\omega = 0)\right|_T = R_o + \frac{\partial R}{\partial I}\delta I = R_o(1+\beta), \tag{3.21}$$

where the definition of $\beta$, implicit in Equation 3.14, has been used to obtain the final equality. The expression $\mathrm{R}_o(1+\beta)$ appears throughout the responsivity equations, especially in terms describing the TES electrical circuit where it is used as a measure of the the non-ohmic nature of the device.

Putting all the components in Figure 3.6 together, the responsivity is

$$\frac{\delta I}{\delta P_\gamma} = \frac{\delta T}{\delta P_\gamma}\frac{\delta I}{\delta T} = \frac{-1}{I_o R_o(1+\beta)}\left[1 + \frac{1}{1+\beta} + \frac{L}{R_o(1+\beta)}\frac{\tau}{\mathcal{L}_I}\left(i\omega + \frac{1}{\tau_{el}}\right)\left(i\omega + \frac{1-\mathcal{L}_I}{\tau}\right)\right]^{-1}. \tag{3.22}$$

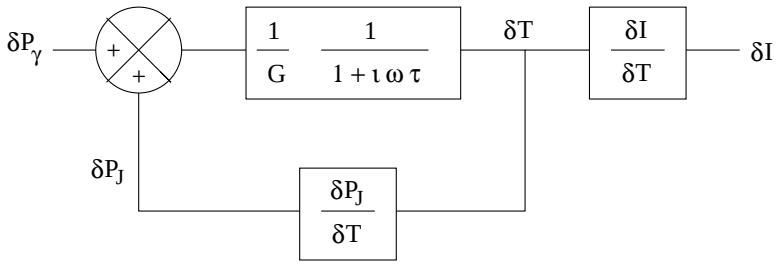


Figure 3.6: **TES Responsivity Diagram** When a fluctuation radiant power is absorbed by the bolometer, the initial temperature changes according to the intrinsic thermal conductance and time constants of the device silicon. The temperature fluctuation causes a change in the Joule power which feeds back in terms of thermal current into the bolometer. The resulting closed electro-thermal feedback (ETF) loop produces a temperature fluctuation which is ultimately converted into a measurable electrical current. As a result of ETF, the bolometer is stable and responds faster than its intrinsic time scales would predict. Note that, for the loop to be stable, it is necessary that $\delta \mathrm{P}_J/dT$ ¡ 0.

In the low frequency limit, the responsivity becomes

$$\frac{\delta I}{\delta P_\gamma}(\omega \approx 0) = \frac{-1}{I_o R_o(1+\beta)}\left[1 + \frac{1}{1+\beta} - \frac{\mathcal{L}_I - 1}{\mathcal{L}_I}\left((1 + \frac{R_s}{R_o(1+\beta)}\right)\right]^{-1}. \quad (3.23)$$

For strong electrothermal feedback, low $\beta$, and stiff voltage bias, the responsivity simplifies further to

$$\frac{\delta I}{\delta P_\gamma}(\omega \approx 0, \mathcal{L}_I \gg 1, \beta \approx 0, R_o \gg R_s) = \frac{-1}{I_o R_o}, \quad (3.24)$$

that is, the reciprocal of the equilibrium voltage bias. In practice, the main deviations of the low frequency responsivity from the simple expression in Equation 3.24 occur when either the operating resistance approaches the shunt resistance, or when the current in the device decreases to the point that $\mathcal{L}_I$ approaches unity (e.g., when $\mathrm{R}_o \approx \mathrm{R}_n$). Introducing the shorthand

$$\tau_I = \frac{\tau}{1 - \mathcal{L}_I}, \quad (3.25)$$

the full expression for responsivity in Equation 3.22 can be rewritten

$$\frac{\delta I}{\delta P_\gamma} = \frac{-1}{I_o R_o(1+\beta)}\left[\frac{L}{R_o(1+\beta)}\frac{\tau}{\mathcal{L}_I}\left((i\omega)^2 + i\omega\left(\frac{1}{\tau_{el}}+\frac{1}{\tau_I}\right)+\frac{1}{\tau_{el}\tau_I}+\frac{R_o\mathcal{L}_I}{L\tau}(2+\beta)\right)\right]^{-1} \tag{3.26}$$

which, after completing the square in i$\omega$, becomes

$$\frac{\delta I}{\delta P_\gamma} = \frac{-1}{I_o R_o(1+\beta)}\left[\frac{L}{R_o(1+\beta)}\frac{\tau}{\mathcal{L}_I}\left(i\omega+\frac{1}{\tau_-}\right)\left(i\omega+\frac{1}{\tau_+}\right)\right]^{-1}. \tag{3.27}$$

The time constants $\tau_+$ and $\tau_-$, corresponding to the poles in the responsivity, are therefore

$$\frac{1}{\tau_\pm} = \frac{1}{2\tau_I}+\frac{1}{2\tau_{el}} \pm \frac{1}{2}\sqrt{\left(\frac{1}{\tau_I}-\frac{1}{\tau_{el}}\right)^2 - 4\left(\frac{R_\circ}{L}\frac{\mathcal{L}}{\tau}(2+\beta)\right)}. \tag{3.28}$$

In general, TES bolometer design aims to produce electrothermal systems which are either over-damped or critically damped. This design goal is achieved if the determinant in Equation 3.28 is positive:

$$\left(\frac{1}{\tau_I}-\frac{1}{\tau_{el}}\right)^2 - 4\left(\frac{R_\circ}{L}\frac{\mathcal{L}}{\tau}(2+\beta)\right) \geq 0 \implies \text{Critically or Over}-\text{damped}. \tag{3.29}$$

Furthermore, it follows from Equations 3.27 and 3.28 that the response is safe from instability (i.e., electrothermal run-away) if

$$\tau_+ \geq \tau_- \implies \text{Stability}. \tag{3.30}$$

In the limit that $\mathrm{L/R}_o \ll \tau/\mathcal{L}_I$, the time constants become

$$\begin{aligned}
\tau_+ &\rightarrow \tau_{el}, \\
&\textit{and} \\
1/\tau_- &\rightarrow \tfrac{1}{2\tau_I}+\tfrac{1}{2\tau_{el}}-\tfrac{1}{2\tau_{el}}\left\{1+\tfrac{1}{2}\left[\tfrac{\tau_{el}^2}{\tau_I^2}-\tfrac{2\tau_{el}}{\tau_I}-4\tau_{el}^2\tfrac{R_\circ}{L}\tfrac{\mathcal{L}}{\tau}(2+\beta)\right]\right\} \\
&\textit{s.t.} \\
\tau_- &\rightarrow \tau\left[1+\mathcal{L}\tfrac{R_\circ-R_s}{R_s+R_\circ(1+\beta)}\right]^{-1}.
\end{aligned} \tag{3.31}$$

It follows that $\tau_+$ corresponds to the electrical response of a stable system, and $\tau_-$ corresponds to the thermal response. In the limit of low $\beta$ and stiff voltage bias, the

thermal-related time constant $\tau_-$ becomes

$$\tau_- \rightarrow \frac{\tau}{1+\mathcal{L}_I}. \tag{3.32}$$

It follows that, in this common limit of device behavior, the intrinsic thermal response time C/G of the detector is decreased by the electrothermal feedback factor $\mathcal{L}_I$.

Figure 3.7 shows the responsivity for TES pixel 1 of ACT chip X.3-2 (see Chapter 4 for pixel naming conventions). Different colored curves in the plot correspond to responsivities at operating points with different ($I_o$, $R_o$) but nearly the same $P_J$. The solid lines in the graph show the responsivity from Equation 3.22, given parameters from model fits to TES current noise spectra and complex impedance described in Chapter 5. The fits to noise and impedance data reveal that, at frequencies higher than $\sim$ 10 Hz, the electrothermal response of the device cannot be explained by the lumped thermal model shown in Figure 3.2. The graphic in Figure 3.7 illustrates a model featuring a pixel body with a distributed thermal network. The pixel is still separated from a cold bath by a weak thermal link $G_o$, but now the pixel is comprised of several distinct heat capacities connected through on-pixel thermal links which are generally much more conductive than $G_o$. Such a model is needed to explain the response of the TES to fluctuations about its operating point as indicated by noise and complex impedance measurements. In a distributed thermal network, the TES resistor is not necessarily thermally lumped with the part of the pixel which absorbs photons. In the graphic of Figure 3.7, light is absorbed in a part of the pixel (labeled ABS for 'absorber') which is distinct from the TES. It follows that, above some frequency, changes in the absorber temperature due to radiation fluctuations $\delta P_\gamma$ may not thermalize to produce the same changes in the TES temperature. Therefore, above some frequency, the responsivity of the distributed thermal model should fall below the responsivity of the lumped thermal model. In the graph in Figure 3.7, the dashed lines correspond to the responsivities in the distributed thermal model which

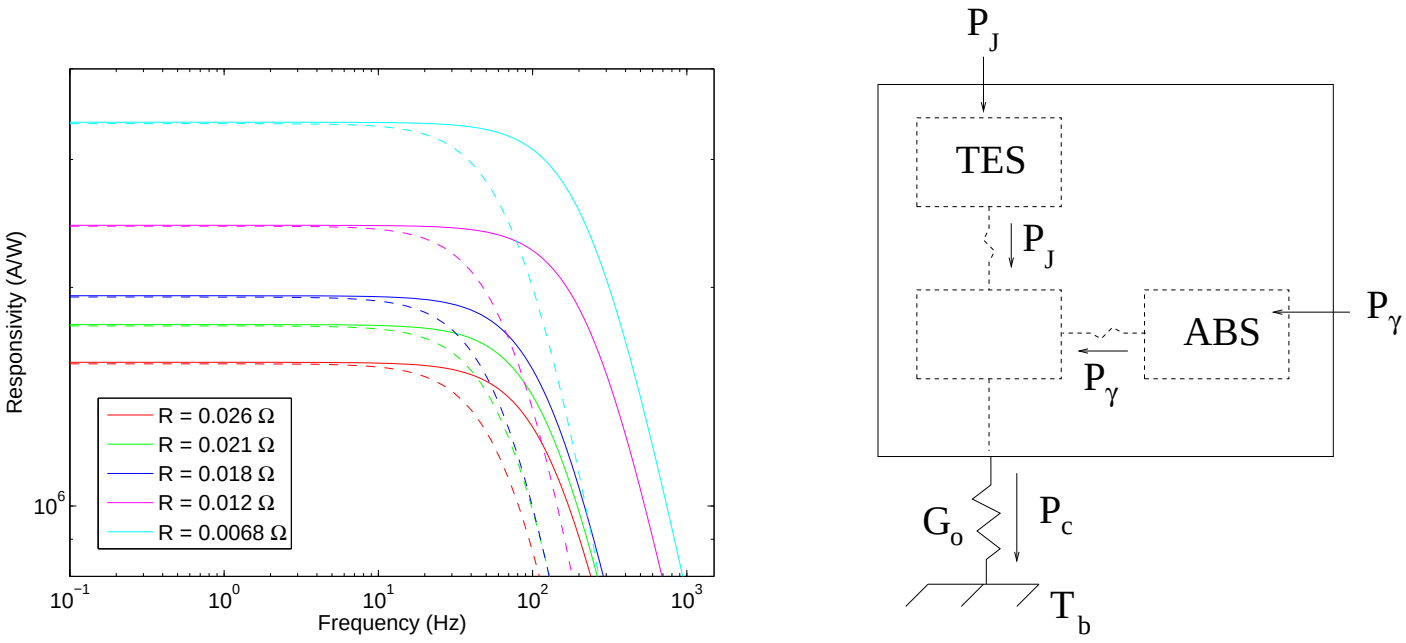


Figure 3.7: **TES Responsivities.** The graph (left) shows TES responsivities for pixel 1 of chip X.3-2 (see Chapter 4 for TES naming conventions). The different curves correspond to different TES operating points ($I_o$,$R_o$) but nearly the same $P_J \approx 15$ pW. The solid lines correspond to the response of a bolometer described by Equation 3.22 with $\alpha$, $\beta$, C, G, and other parameters obtained through fits to TES current noise and complex impedance data (see Chapter 5 on device characterization). The noise and impedance fits reveal that a more complex thermal circuit than that shown in Figure 3.2 is needed to characterize the response of the system to fluctuations about the operating points. The figure (right) shows an example of a distributed thermal circuit to contrast with the lumped thermal circuit of Figure 3.2. Because photon power $P_\gamma$ is absorbed into a part of the pixel body (labelled ABS for 'absorber') that is not thermally lumped with the TES film, the responsivity of the device will be reduced for frequencies high enough that the temperature fluctuation does not thermalize across the pixel. The dashed lines in the graph show the responsivity for the distributed thermal model which fits the noise and impedance data. The responsivity for the distributed thermal model deviates from the lumped thermal model at frequencies above 10 Hz. At low frequencies, the two models' responsivities match because fluctuations are slow enough that the distributed pixel thermalizes. As a final note, the responsivities shown in the plot are not significantly influenced by the electrical TES bias circuit because the R/L characteristic frequency of the circuit lies around 5-10 kHz, well above the thermal response bandwidth of the device.

follow the lumped thermal responsivities well at low frequencies where the pixel is able to thermalize properly. At frequencies beginning around 10 Hz, however, the TES begins to fail to thermalize with the radiation absorbing element of the pixel, and the distributed responsivity falls below the responsivity for a thermally lumped bolometer.

## 3.5 Noise: Sensitivity

Within the responsivity bandwidth, the dominant sources of noise are the thermal fluctuations associated with the background radiation (photons) absorbed by the pixel, and the thermal link (phonons) between the bath and the pixel. Noise for a bolometer is usually quoted in terms of Noise Equivalent Power (NEP): noise refered to thermal power fluctuation on the pixel. Since the phonon and photon noise sources originate as a thermal power fluctuation on the pixel, they are naturally expressed in terms of NEP.

The noise power spectrum of both photons and phonons is white. The magnitude of the NEP due to fluctuations in the photon load is given in terms of linear spectral power ($W/Hz^{1/2}$) as

$$NEP_{\gamma} = \sqrt{2P_{\gamma}h\nu}, \tag{3.33}$$

where $P_{\gamma}$ is the background loading (Table 2.5), h is Planck's constant, and $\nu$ is the frequency of radiation. The magnitude of the NEP due to phonons in the thermal link between the bath and pixel is (again in $W/Hz^{1/2}$)

$$NEP_{ph} \sim \sqrt{4kG_oT_o^2}, \tag{3.34}$$

where k is Boltzmann's constant, $G_o$ is the thermal link between the pixel and the bath (using the naming convention from Figure 3.7), and $T_o$ is the operating temperature of the pixel. The subscript 'ph' is for phonons.

Figure 3.8 shows the NEP for pixel number 1 on ACT TES chip X.3-2 (X.3-2.01). The left graph shows noise $\mathrm{NEP}_{det}$ due solely to sources in the detector. The different colored curves correspond to the same set of operating points ($\mathrm{I}_o$,$\mathrm{R}_o$) at which the X.3-2.01 responsivity was reported in Figure 3.7. The curves are models fit to noise spectrum data collected at the corresponding operating points (see Chapter 5). Within the responsivity bandwidth below $\sim$ 10 Hz, the NEP is dominated by the white phonon noise spectrum (black horizontal line). At higher frequencies the NEP rises due to other sources of detector NEP. The right graph in Figure 3.8 shows the NEP contribution from both the detector and the background radiation. Total NEP is given by

$$NEP_{tot} = \sqrt{NEP_{det}^2 + NEP_{\gamma}^2}. \tag{3.35}$$

The radiation loading plotted in Figure 3.8 corresponds to median opacities on winter evenings at the observing site (Table 2.5). Under such conditions, the $\mathrm{NEP}_{tot}$ for the 147 GHz and 215 GHz ACT observing bands is dominated by the detector noise. Only in the 278 GHz band does the contribution $\mathrm{NEP}_{\gamma}$ of the photons account for most of the noise in the response band. One caveat, however, is that the saturation power of TES X.3-2.01 may be too low for operation in the 278 GHz band, depending on the choice of the current bias $\mathrm{I}_{DB}$. If the saturation power were high enough to work in the 278 GHz band, then the thermal conductance between the pixel and the bath would need to be higher, and the phonon noise would increase.

In the 10 Hz bandwidth in which the responsivity and the noise spectrum of detector X.3-2.01 is flat, the total NEPs are $3.5\times10^{-17}$, $4.0\times10^{-17}$, and $6.0\times10^{-17}$ $\mathrm{W/Hz^{1/2}}$ for the 147, 215, and 278 GHz bands, respectively. The resulting RMS noise power is obtained by multiplying the NEP by the square root of the response bandwidth to give $11.1\times10^{-17}$, $12.6\times10^{-17}$, and $19.0\times10^{-17}$ W for the three bands in order of inceasing frequency. A detector with 10 Hz bandwidth has an effective

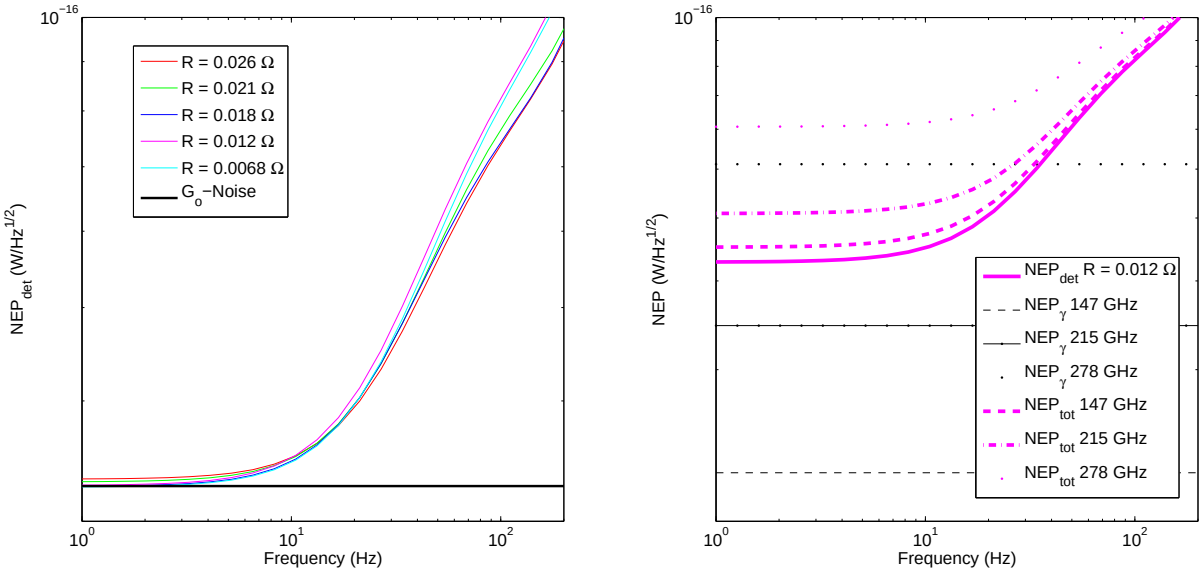


Figure 3.8: **Noise Equivalent Power.** The left graph shows model detector noise curves that have been fit to noise data from pixel 1 of TES X.3-2 (see Chapter 5), for which the critical temperature is 0.535 K and the thermal conductance to the bath is 126 pW/K. The $\mathrm{NEP}_{det}$ shown at left is therefore only from the detector; no radiation noise $\mathrm{NEP}_{\gamma}$ is included. The colors of the curves correspond to different TES operating points ($\mathrm{I}_o$, $\mathrm{R}_o$) ($\mathrm{P}_J \sim 15$ pW) which are the same as those for which the responsivities were quoted in Figure 3.7. Within the response band of the detector, below 10 Hz, the noise is dominated by the thermal fluctuations between the pixel and the cold bath (horizontal black line). In the right graph, both detector and photon loading NEPs are plotted. In all but the 278 GHz ACT observing band, the detector noise dominates total NEP. The background loading the $\mathrm{NEP}_{\gamma}$ plotted on the right corresponds to median opacities on winter nights at the ACT site (Table 2.5). As shown in the graphs, both the detector noise power and the radiation noise power have a white NEP spectrum.

sampling rate of 0.05 s, such that, in one second, the noise power is sampled 20 times. Therefore, integrating the detector response over one second reduces the RMS noise power by a factor of $0.05^{1/2}$ giving a detector sensitivities of $2.5\times10^{-17}$, $2.8\times10^{-17}$, and $4.2\times10^{-17}$ W-sec$^{1/2}$ in the 147, 215, and 278 GHz bands, respectively, for winter evenings with median atmospheric opacities.

## 3.6 Discussion

With the sensitivities of the detectors in each band determined, it is possible to evaluate ACT's ability to resolve the fluctuations in the CMB. The sensitivities were found in Section 3.5 to be $2.5\times10^{-17}$, $2.8\times10^{-17}$ , and $4.2\times10^{-17}$ W-sec$^{1/2}$ for the 147, 215, and 278 GHz ACT bands. Figure 3.9 is a plot of the sensitivity of a single ACT pixel after a year ($3.14 \times 10^7$ seconds) of observing a 200 square degree field. Solid lines in the plot show the detector signal power level for the anisotropies (Chapter 2). The sensitivities were computed assuming the detector time is divided evenly over the observing area. For instance, a square degree would be observed for $3.14 \times 10^7$ / 200 seconds in the course of the year. The figure shows that in one year of integration time, a single pixel will be able to achieve a signal to noise of one for anisotropies between multipoles from 1000 to 1500 or equivalently degree scales from 0.18° to 0.12°. Given that there will be of order 1000 detector pixels per ACT band, the detector array sensitivity in each band will be approximately 30 times better than the sensitivity of a single pixel.

An unexpected result of the ACT detector research is that the pixels do not behave as a lumped thermal element connected to the cold bath as in Figure 3.2. The distributed thermal nature of the ACT detector pixel has significant consequences for the bandwidth of the pixel and, less importantly, the out of band noise. Figure 3.7 shows how the distributed nature of the ACT pixels decreases the response bandwidth

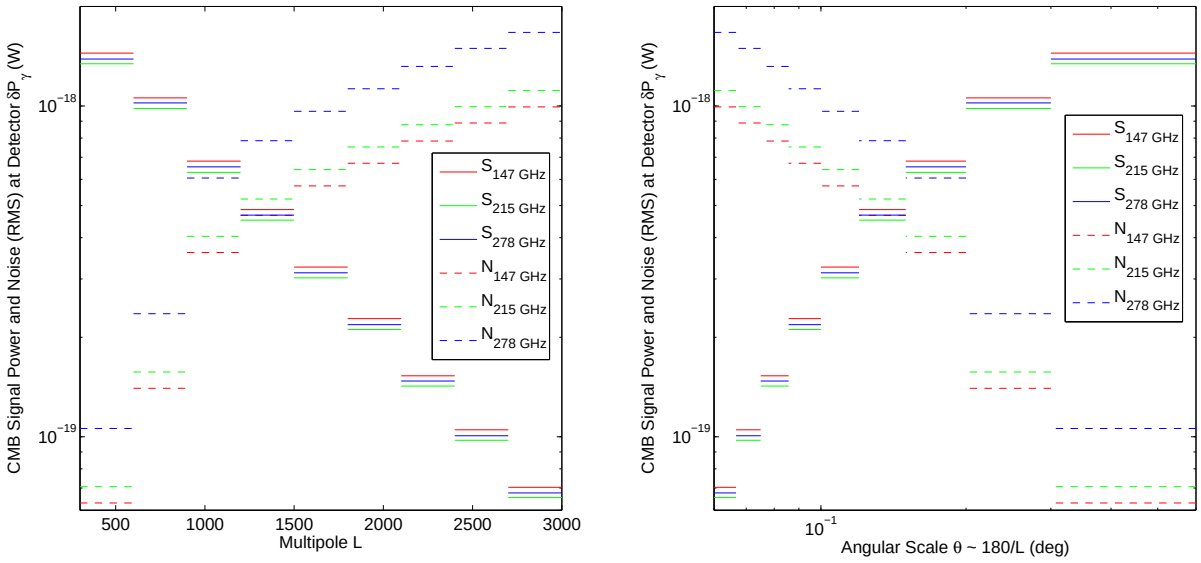


Figure 3.9: **Signal and Noise after One Year of Observations.** The detector signal power, as calculated in Chapter 2, is given by the solid red, green, and blue bars for various angular scales of anisotropy in the 147, 215, and 278 GHz ACT bands, respectively. Shown in dashed bars, are the corresponding sensitivities of a single ACT pixel to the anisotropies after $3.14 \times 10^7$ seconds ($\sim$ 1 year) of integration on 200 square degrees of sky. The left graph shows the anisotropy in multipole space while the right plot gives the characteristic angular scales of the anisotropies. As computed in Section 3.5, the unintegrated sensitivities are $2.5{\times}10^{-17}$ W-sec$^{1/2}$, $2.8{\times}10^{-17}$ W-sec$^{1/2}$, and $4.2{\times}10^{-17}$ W-sec$^{1/2}$ for the 147, 215, and 278 GHz ACT bands. The integrated sensitivities are effectively increased by a factor of 30 when one considers that each band has on order 1000 detectors observing simultaneously.

of the detectors to almost one-half of the bandwidth that the detector would have if all the heat capacity measured on its pixel were thermally lumped. One significant consequence of the unexpected low bandwidth of the ACT detectors is that the scan strategy described in Section 2.2 may need to be altered. In the next chapter, a discussion of the ACT detector fabrication illuminates the ways in which the heat capacity of the pixel may be distributed. The detector tests which have legitimized the notion of a distributed thermal circuit in ACT detectors are reviewed in Chapter 5.

## 3.7 Acknowledgments

The bolometer model used to describe the ACT TESs in this section is well established. In particular, the author has found the seminal works of Mark Lindeman and Kent Irwin illuminating. A representative set of references is [24, 19, 25, 15]. The responsivity and NEP model curves for X.3-2.01 are provided courtesy of Rolando Dunner.

# Chapter 4

# Detector Fabrication

## 4.1 Introduction: TES Pop-Up Devices

This chapter is a review of TES detector fabrication, emphasizing the key attributes required for ACT detector characterization. The overall process involves depositing an absorber; depositing and patterning the TES, wiring and other metals; and finally silicon micromachining to cut the thin pixels – Pop-up Devices – out of the thick silicon substrate. The fabrication is carried out at NASA Goddard Space Flight Center under the direction of James Chervenak and Christine Allen. Figure 4.1 provides an overview of the chips and their salient features.

The ACT TES chips are made from a silicon-on-insulator (SOI) wafer, twelve chips at a time. Figure 4.2 shows the chip layout on a wafer and the cross-section of an ACT wafer. ACT SOI wafers feature three layers. A thin (1.4 $\mu$m) layer of silicon is separated by an oxide (4000 Å) from a thick silicon layer. The total wafer thickness is 450 $\mu$m. Fabrication of TES chips takes place in four general steps. First, a radiation absorbing layer of ions is implanted in the device layer real estate that will ultimately be occupied by the pixels. Next, the superconducting MoAu bilayer is deposited across the device wafer. The third step involves patterning the bilayer into discrete

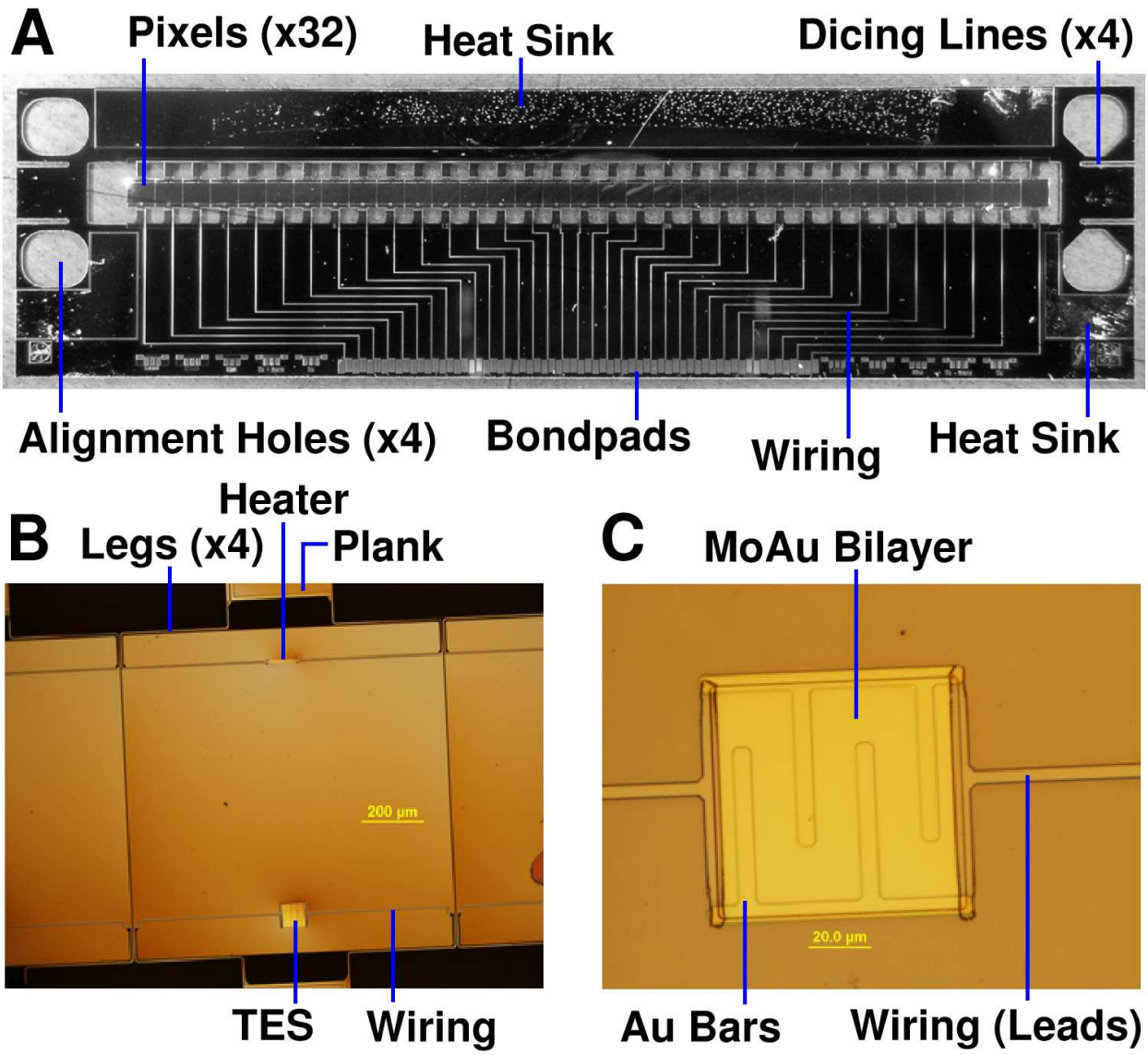


Figure 4.1: **TES Chip with Details.** A TES chip (A) has 32 TES-bearing pixels suspended in a central rectangular window. A $33^{rd}$ pixel without TES is included at far right as a wiring path for the optional heater. Wiring runs to each TES from wirebond pads at the edge of the chip. Three gold heat sinks provide thermal anchoring. Alignment holes and dicing lines facilitate folding the chip into its Pop-up Device configuration. Each pixel (B) is made of thin (1.4 $\mu$m) silicon which is implanted with ions to facilitate absorption of radiation. Planks launch from the thick chip frame on either side of the pixel. From each plank two narrow (5-20 $\mu$m) legs extend to the corners of the pixel. The 1.05 mm x 1.05 mm pixel bears the TES and optional heater resistor (no longer used). Wiring (5 $\mu$m wide) runs from the planks across the legs to the on-pixel devices. The TES (C) body is made of a MoAu bilayer which superconducts below approximately 0.4-0.55 K, depending on the TES recipe. Gold bars are patterned atop the bilayer to alter the nature of the superconducting transition.

superconducting TES films associated with each pixel. Additional metallizations and patterning are performed to create the wiring, gold bars atop the TES, bond pads, and thermal sinks. The final step involves micromachining the silicon to create the thin pixels isolated from the frame of the chip by narrow silicon legs. The handle wafer is etched away from behind the pixel locations, leaving only the thin 1.4 $\mu$m membrane of device silicon. Finally, the device layer is patterned to form the pixels and suspension structures (planks and legs).

## 4.2 Absorber Implant

To make pixels that absorb radiation, the device wafer from which the pixels are fabricated must be made to have finite sheet resistance at the sub-Kelvin device temperature. From the factory, the device wafers are boron doped with resistivity of 14-22 $\Omega$-cm at room temperature. At low temperatures, however, such an impurity level is not high enough to prevent the silicon from capturing most of its charge carriers and becoming insulating. Additional surface doping is necessary to achieve the impurity level necessary to remain resistive at sub-Kelvin temperatures.

To achieve the necessary carrier density, the device layer is implanted with extra phosphorous ions to concentrations beyond the background doping. Figure 4.3 illustrates the implant process. A thin oxide is grown into the device layer, and aluminum is patterned on the wafer to mask all regions outside the pixel area. The wafer is then bombarded by an energy-calibrated beam of phosphorous ions. The ions do not penetrate silicon which is masked by aluminum. In the pixel regions, the phosphorous ions implant into the silicon and oxide to a depth and concentration proportional to the energy of the beam. After the ion implant, the aluminum layer is stripped and the wafer is heated (annealed) to redistribute the remaining phosphorous in the device layer and to heal the device layer lattice which has been damaged by sput-

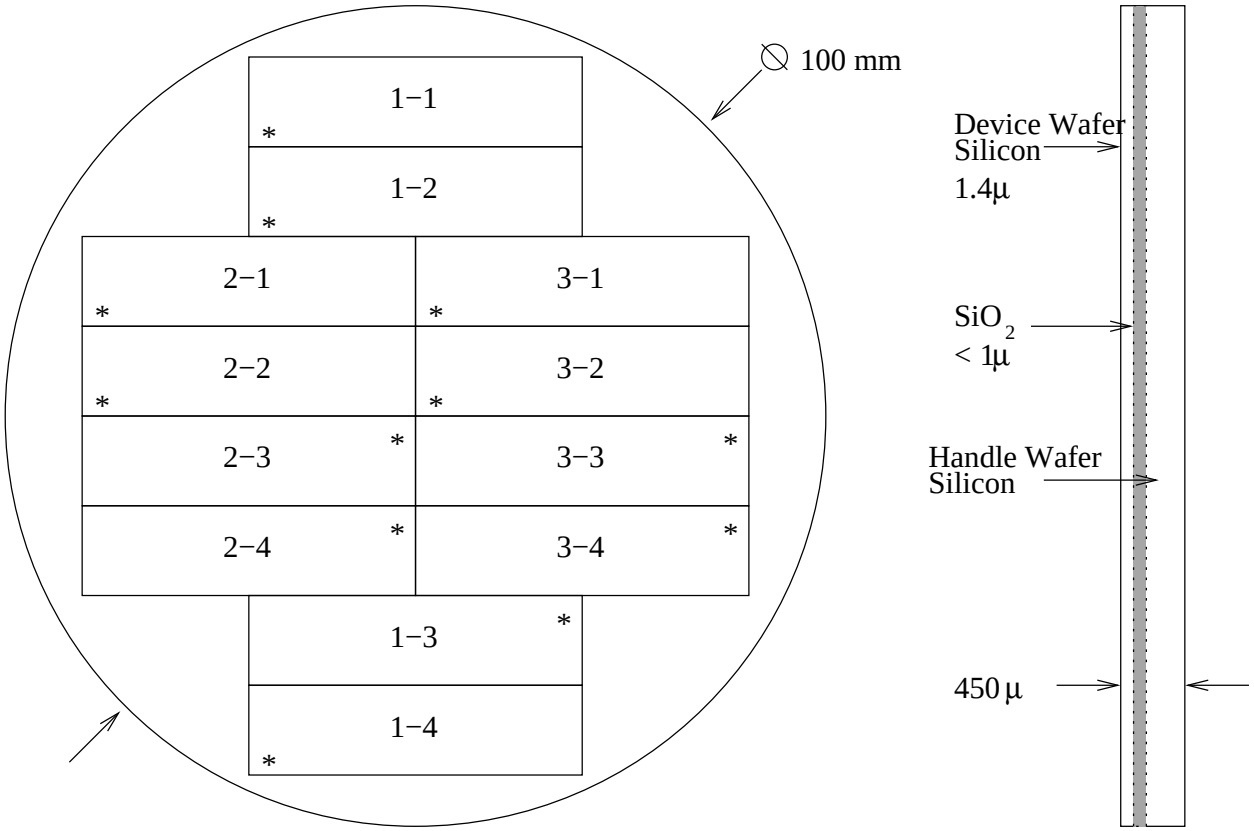


Figure 4.2: **Chip Layout on a SOI Wafer.** TES chips are made twelve at a time on 100 mm SOI wafers. The chips are numbered by the column and row in which they lie on the wafer. Chip 1-4 is a dummy chip for which the pixels are not micromachined. Stars mark the upper–right of the chip as pictured in Figure 4.1 (A). The silicon-on-insulator (SOI) wafers used in the fabrication consist of a thin layer of silicon (1.4 $\mu$m) called the device layer. The device layer is separated by an oxide from a thicker layer of silicon called the handle wafer. The oxide layer is 4000 Å thick, and the total wafer thickness is 450 $\mu$m.

tering during the implant. Finally, the device layer oxide is stripped, removing the fraction of the phosphorous that deposited in the oxide. The target absorber carrier concentration is near $4 \times 10^19$ cm$^{-3}$.

## 4.3 TES Bilayer

The ACT TES is made by depositing a layer of gold atop a layer of molybdenum [8]. The thin film of sputtered TES molybdenum has a critical temperature $T_c$ of 1.1 K and is therefore a superconductor at the characteristic device bath temperature of 300 mK. Contact between the normal gold and the superconducting molybdenum results in the Superconducting Proximity Effect (SPE). SPE involves the diffusion of Cooper pairs from the superconductor to the normal metal and diffusion of electronic excitations from the normal metal to the superconductor. Through the SPE, the Mo/Au bilayer behaves as a superconductor with a $T_c$ lower than that of molybdenum alone. Gold is chosen as a normal metal for its high electrical and thermal conductivity. High electrical conductivity is desirable to achieve a low normal state resistance and therefore a low operating resistance. The high thermal conductivity of the gold layer allows the TES to thermalize quickly and therefore behave as a simple lumped thermal element. One measure of gold's suitability is its Residual Resistance Ratio (RRR) – which is the ratio of the metal's room temperature resistance to its resistance at some colder temperature. From 300 K to 4 K, the MoAu films for ACT have been measured to have a RRR around six [8]. The RRR of the bilayer is primarily due to the gold because molybdenum has a sheet resistance six to ten times that of gold. Molybdenum is a good superconductor to match with gold because it does not diffuse into the gold to form performance degrading intermetallics. Finally, the gold has the benefit that it is resistant to corrosion. The external gold layer obviates the need for an extra passivation film to protect the TES. A passivation film can prove a

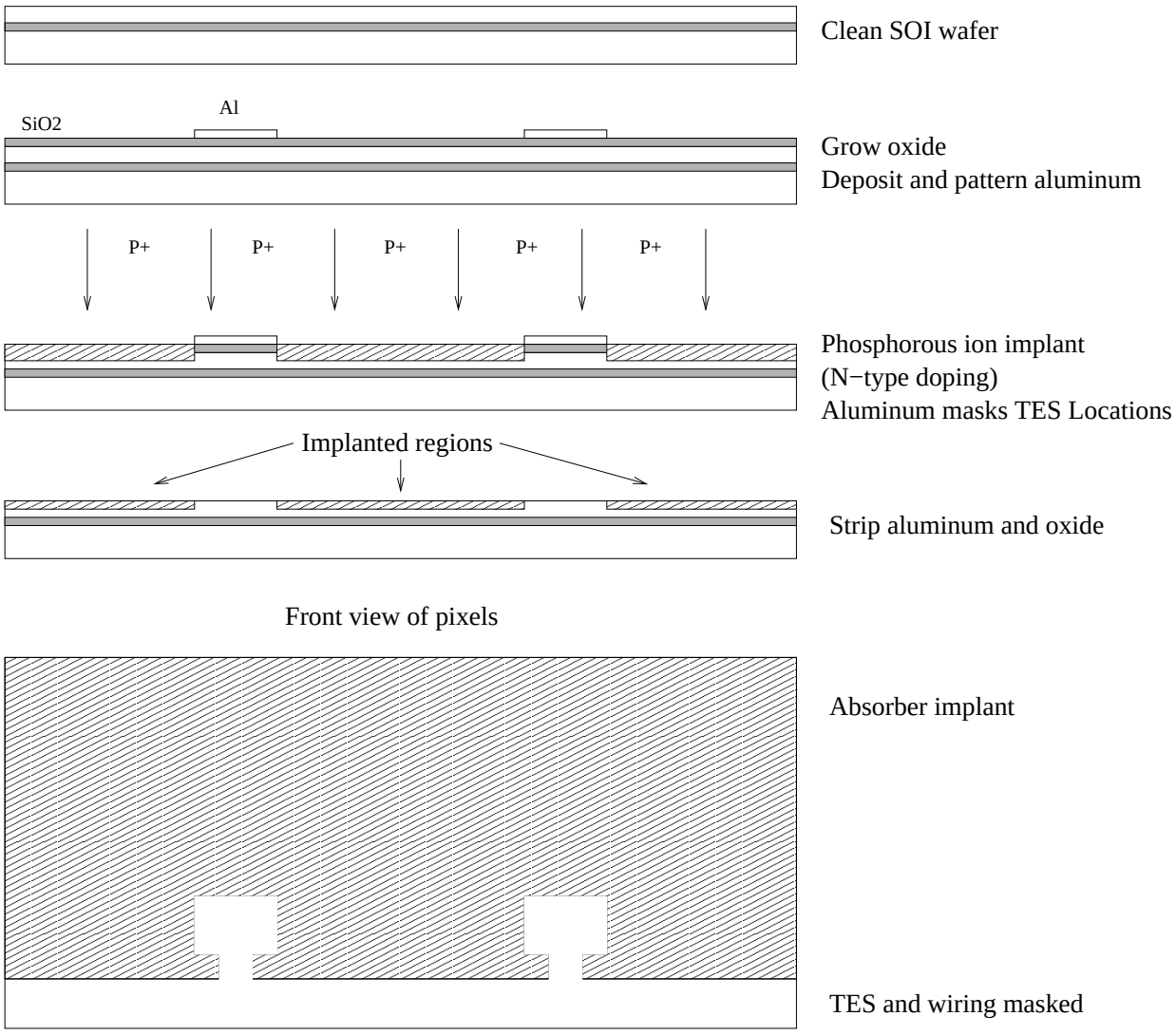


Figure 4.3: **Absorber ion implant.** To absorb photons, the pixels must have a sheet resistance of $\sim$ 100 $\Omega$/sq. at sub-Kelvin temperatures. Phosphorous doping above the manufacturer provided level is necessary to achieve the absorber sheet resistance. Additional doping is accomplished by bombarding the device wafer with a phosphorous ion beam of calibrated energy. Phosphorous deposits in silicon and a thin layer of oxide that is not masked by aluminum (an area limited to the pixel area not occupied by the TES or wiring). The aluminum and oxide are then stripped away, leaving only the implant that imbedded in the silicon. Specification of the beam energy, and therefore the penetration depth of the phosphorous into the oxide+silicon, and specification of the oxide determine the amount of phosphorous that remains in the silicon after the strip. The target carrier concentrations for the absorbers are $\sim 4 \times 10^{19}$ cm$^{-3}$. Chapter 2 describes how the target concentrations affect the absorption efficiency of the detectors.

poor mechanical match to the pixel, and bow the thin silicon out of the plane of the detector.

Because the molybdenum is shunted by the low resistivity gold in the normal state, the normal resistance of the device is approximately set by the thickness of the gold in the bilayer. Given a certain gold thickness, the thickness of the molybdenum can be chosen to give the proper critical temperature. The target normal resistance for the ACT detectors is 20 mΩ. Two gold thicknesses have been developed to realize this normal resistance. The first recipe prescribes a 2000 Å thick gold layer for an 8-9 mΩ per square sheet resistance. This recipe requires the detector to be two squares long. The second recipe has a higher sheet resistance of 20 mΩ per square with a gold thickness of 1400 Å. TESs with the thinner gold therefore are one square. Figure 4.4 shows the critical temperature as a function of molybdenum thickness for the two gold recipes.

In practice, the molybdenum and gold of the bilayer are not deposited with uniform thickness across the wafer. In general, both metal films will be thinner towards the edge of the wafer. In the case of molybdenum, the thinning produces devices with lower critical temperature toward the edge of the wafer. Figure 4.5 shows critical temperatures as a function of distance from the wafer center as measured for TES chip X.3-2. In the case of gold, the edge thinning will be primarily reflected by an increase in normal resistance for devices away from the wafer center.

## 4.4 TES Patterning and Other Metallization

Once the bilayer is deposited, then it is necessary to pattern the MoAu into discrete TESs, one on each pixel. Figure 4.6 illustrates the process which begins with patterning a mask of photoresist (PR) over the TES areas. With the TES locations protected by PR, an ion mill is used to sputter away the gold elsewhere on the wafer

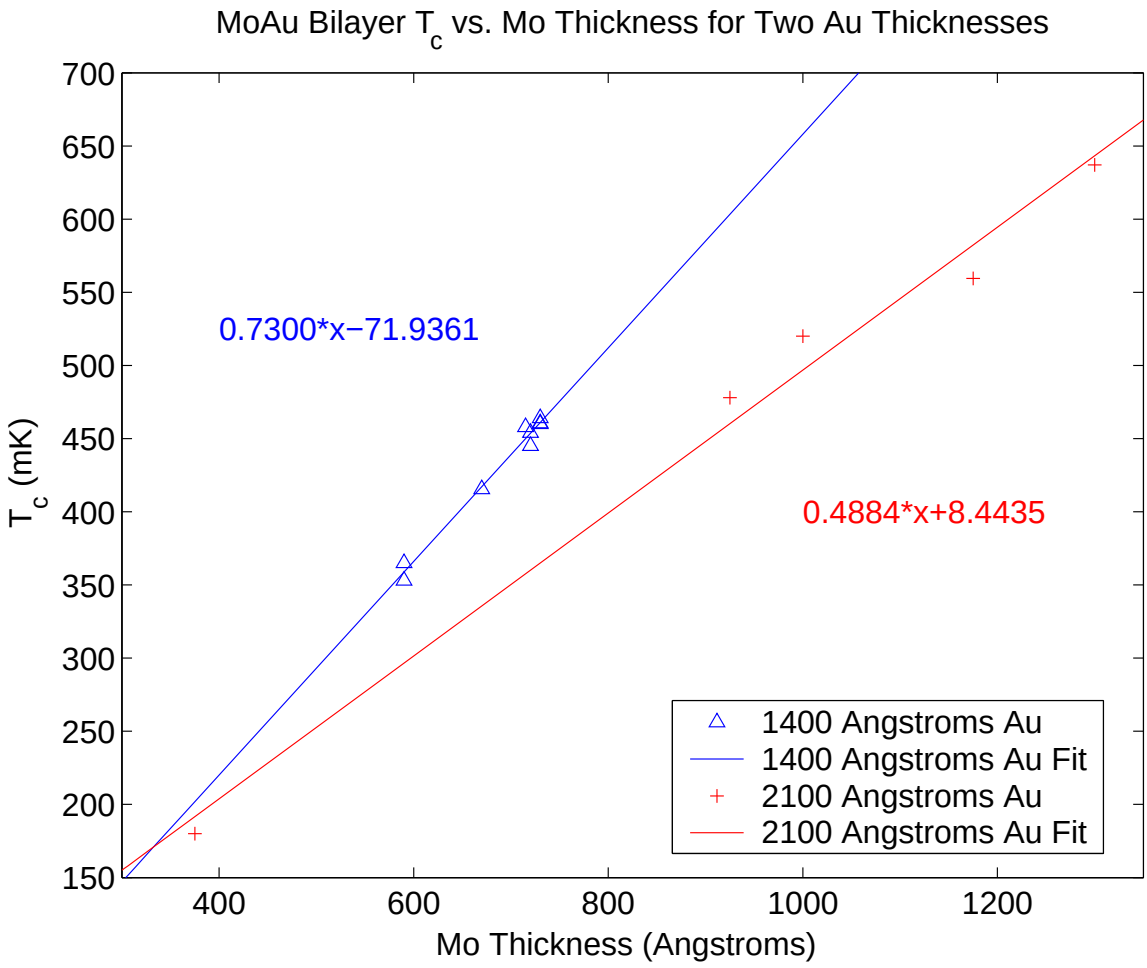


Figure 4.4: **$T_c$ vs. Molybdenum Thickness.** The MoAu bilayer is made with sputtered molybdenum and electron-beam evaporated gold. Through the Superconducting Proximity Effect, the MoAu bilayer acts as a single superconductor with normal resistance $R_n$ and critical temperature $T_c$ that depend on the thicknesses of the two metal layers. Because the gold has lower normal resistance than the molybdenum, the gold thickness approximately determines $R_n$ of the bilayer. Once the gold thickness is chosen to fix $R_n$, then the molybdenum thickness is varied to produce the desired $T_c$. Critical temperatures corresponding to two types of MoAu bilayer are plotted as a function of molybdenum thickness above. The first type (blue) has 1400 Å thick gold and a 21 mΩ/sq normal sheet resistance. The second type (red) has 2100 Å thick Au and 9 mΩ/sq sheet resistance. The fit formulae give $T_c$ in Kelvin for x in Å. The data in the graph were taken at NASA GSFC and provided courtesy of James Chervenak.

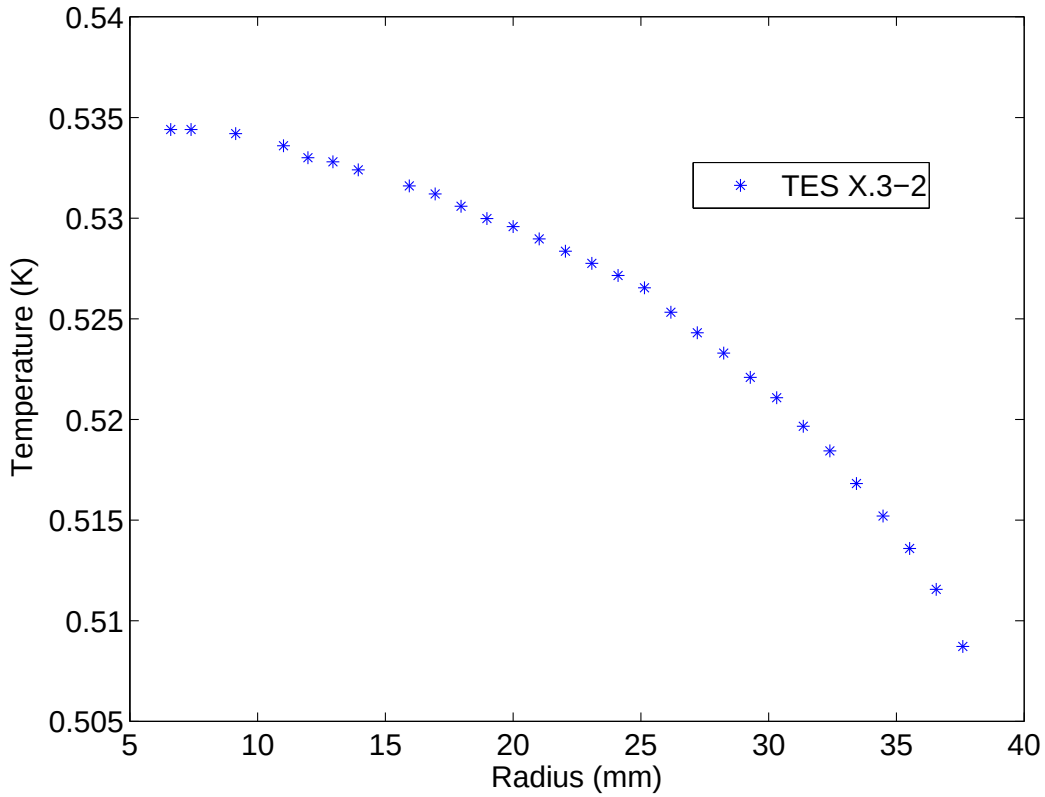


Figure 4.5: **$T_c$ vs. Distance from Wafer Center.** Bolometers are fabricated on a 100 mm diameter wafer. The molybdenum of the MoAu bilayer is thicker in the center of the wafer, resulting in devices characterized by lower $T_c$s towards the wafer edge. The radius plotted along the X-axis is the distance to the TES from the center of the wafer as drawn in Figure 4.2. The Y-axis is the transition temperature of the device.

until the molybdenum layer is reached. Then a Mo-Nb-Mo trilayer is deposited across the pixel with corresponding thicknesses of 500-200-200 Å. This trilayer along with the molybdenum remaining from the original bilayer deposition and etch (which is not beneath gold) will comprise the wiring to each TES. A layer of PR is patterned over the wiring locations and the absorber. All exposed trilayer plus the original molybdenum from the bilayer not protected by gold is then etched away. The gold of the TES film acts as an etch stop that protects the molybdenum beneath. The absorber is protected with PR in this step because the wiring etch may attack the absorber once the trilayer and bilayer molybdenum are etched away. To remove the trilayer and bilayer molybdenum from the absorber region, everything but the absorber is masked with PR, and an absorber friendly etch is used to clear the metals off the absorber.

At this point the absorber, TES bilayer, and wiring are all deposited and patterned. The next step is to pattern an extra gold layer on the top of the TES. Figure 4.7 is a guide to this part of the fabrication. Until this point, all patterning has been accomplished by first depositing the metal, then masking certain regions with PR, then etching all metal that is not protected by the PR mask. Instead of the mask-then-etch technique, the next step is performed by a process called lift-off. With lift-off, PR is first deposited in all areas where metal is *not* wanted. The metal is then deposited over the wafer. Finally, the PR is stripped such that all metal which resides atop PR is lifted off. The gold lift-off pattern forms fingers which extend onto the TES film in a direction transverse to the current. Additional gold runs along the boundaries of the TES parallel to the current flow and normal to the fingers. The thickness of the gold bars is 2500 Å. By the proximity effect, the critical temperature of the molybdenum beneath the gold bars is suppressed to the extent that the molybdenum in the gold bar regions remains normal at the operating temperature of

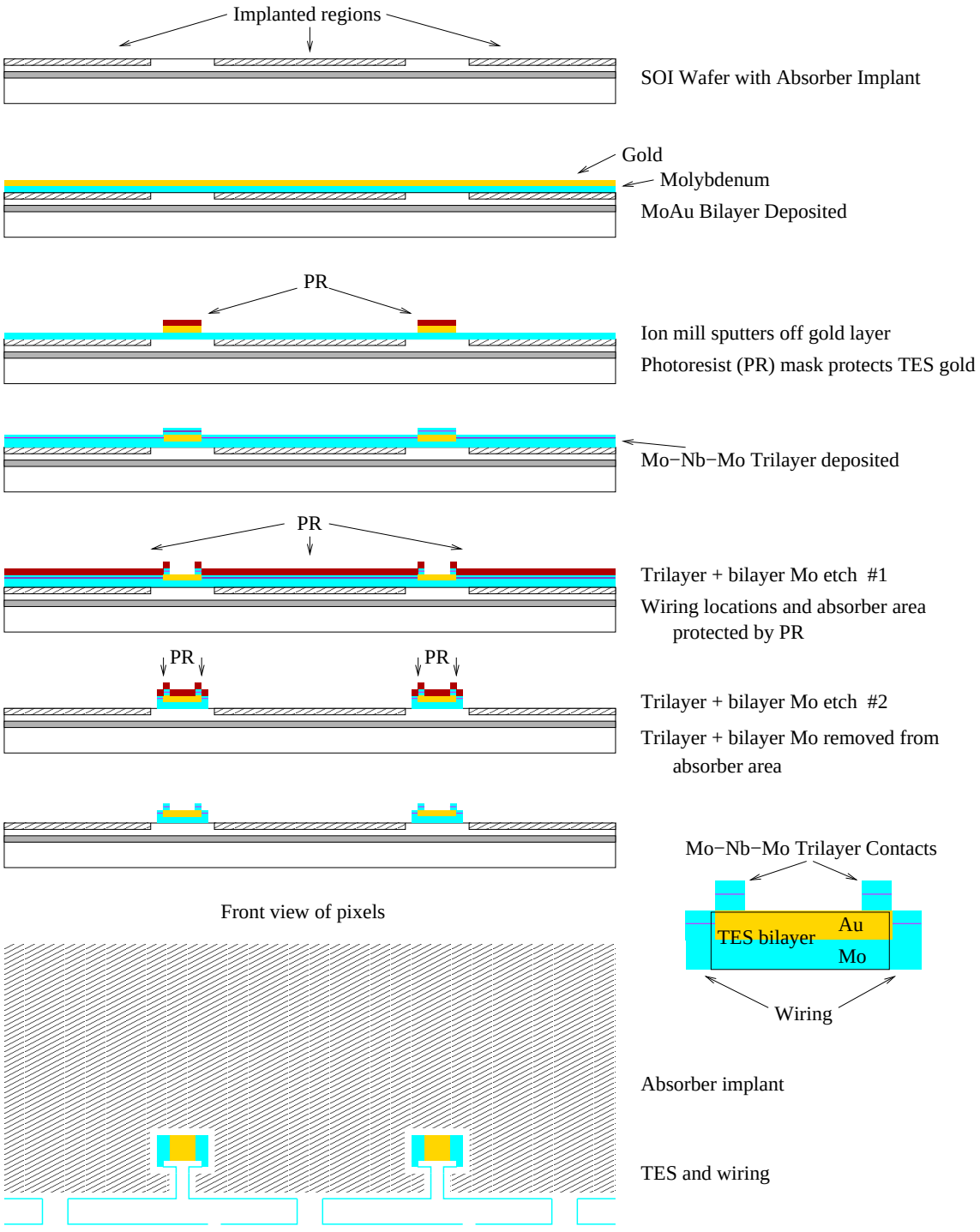


Figure 4.6: **Patterning of the TES and Wiring.** After the absorber implant, the MoAu bilayer is deposited. Using an ion mill, the gold is then sputtered off with PR masking regions above each TES film. Next, a Mo-Nb-Mo wiring layer is deposited (thickness: 500-200-200 Å). Together with the original molybdenum from the bilayer, the Mo-Nb-Mo trilayer is etched to form the TES leads. An area of the trilayer is left overlapping the edge of the TES bilayer to form contacts. The step in the trilayer at the edge of the MoAu results in unreliable connectivity, however, and so follows the necessity of including the continuous bilayer molybdenum in the leads. Because the lead etch is harmful to the absorber, PR protects the absorber area when the wiring is defined. Then, all areas but the absorber are masked and the wiring layers are removed from the absorber with an etchant that does not attack the implanted silicon.

the device. For this reason, the gold pattern is sometimes referred to as a "meander" since the supercurrent of the bilayer is forced on a path which meanders across the TES, avoiding the normal regions beneath the gold bars. The extra gold serves to condition the shape of the transition. The gold bars covering the TES boundaries parallel to current flow ensure that any overetch of the bilayer gold during the ion mill step does not increase the critical temperature of the bilayer along the TES edge [16]. A bilayer film with spatially nonuniform $T_c$ is characterized by corresponding nonuniformities in the slope (dR/dT) of the TES transition. The presence of the transverse gold bars decreases the slope of the transition and therefore decreases the electro-thermal feedback of the detector. Decreasing the transition slope has been found to mitigate noise at high frequencies that is otherwise unexplained [43]. For this reason, the gold bars are often referred to as noise mitigation (NM) features.

Additional lift-off steps deposit large-area gold pads on the chip frame which may be used to thermally sink the chip to the larger cryogenic cold bath. Aluminum is also lifted-off to form bond pads by which to connect the TES wiring to bias lines.

The lift-off process is attractive for its simplicity. It involves PR patterning, metal deposition, and PR strip (usually innocuous acetone). On the other hand, the metal patterning involved in shaping the TES and wiring requires a final etch step which may be complicated to perfect and also may cause damage to other parts of the device (e.g., the thin absorber). The disadvantage to lift-off is that it introduces intermediate steps between the depositions of two adjacent metal layers. These intermediate steps compromise the intimate contact necessary, for instance, between the molybdenum and gold of the TES bilayer.

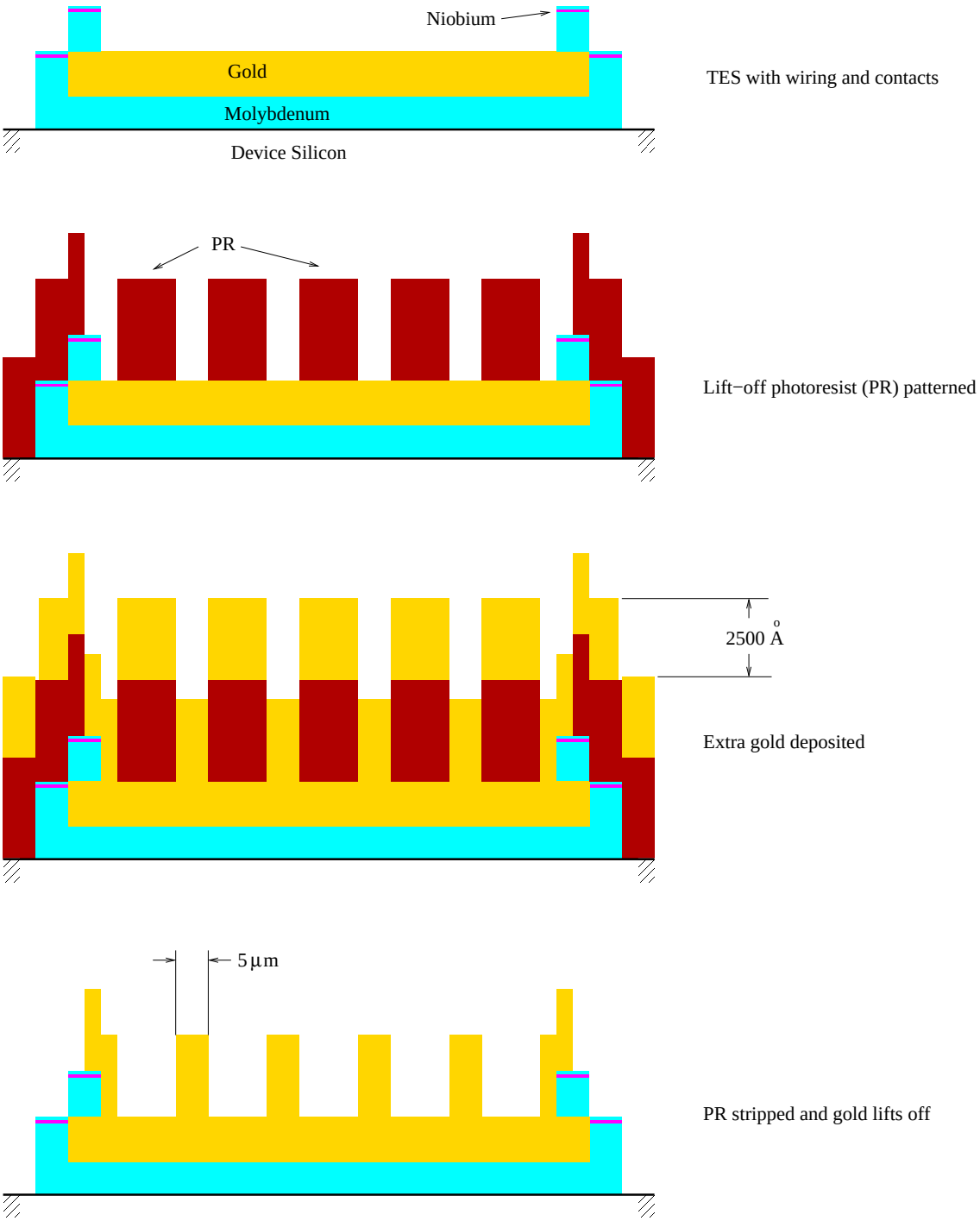


Figure 4.7: **Lift-off of TES Gold Bars.** For lift-off processes, PR is deposited in the negative image of what the final metal pattern will be. Metal is then deposited onto the wafer. The PR is then stripped, lifting off any metal which fell on the PR mask. For the TES, lift-off is used to deposit 2500 extra angstroms of gold in a bar pattern across the TES. Other TES chip features patterned by lift-off include gold pads for thermal sinking of the chip, aluminum pads for wirebonding to the TES wiring, and optionally an AuPd heater resistor on each pixel. Horizontal and vertical dimensioning is to approximate scale (1400 Å Au bilayer recipe), but the vertical-to-horizonal scaling is uncharacteristically large.

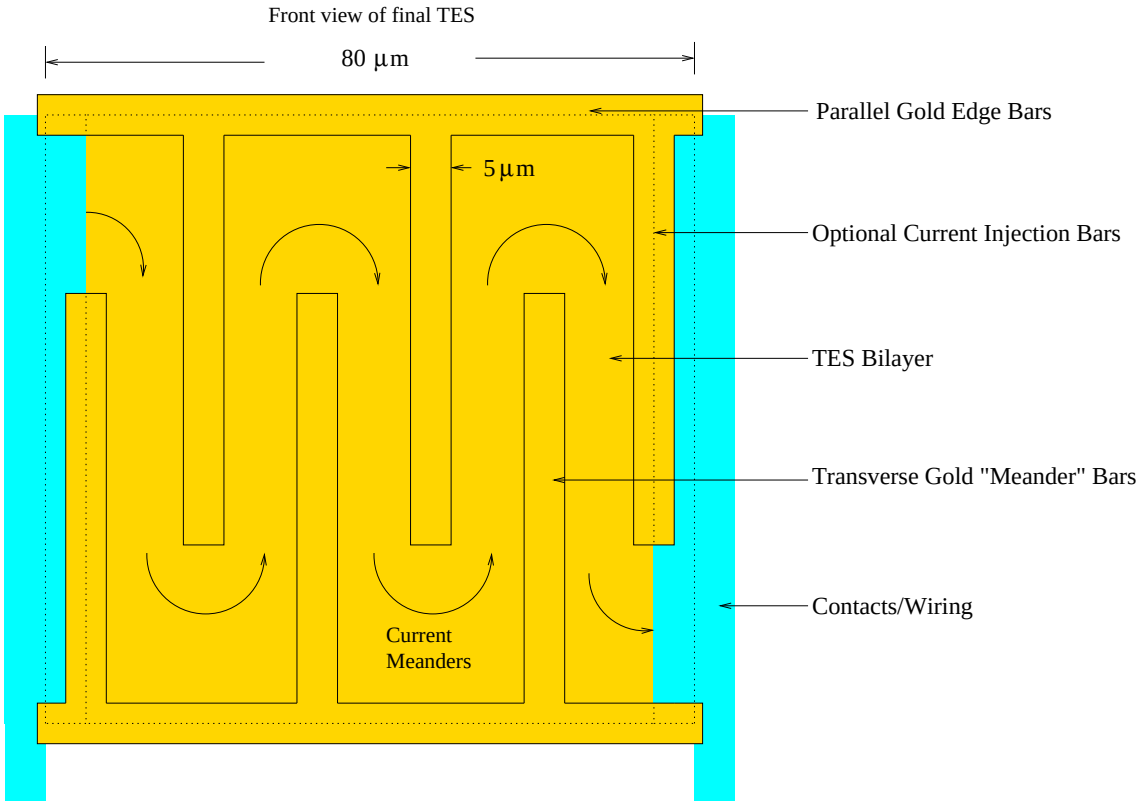


Figure 4.8: **Final TES Configuration** The final TES features one or more squares of TES MoAu bilayer. The wiring to the TES consists in the continuous layer of molybdenum from the bilayer below an additional Mo-Nb-Mo trilayer. The trilayer overlaps the MoAu bilayer at either edge of the TES, forming the contacts. Additional gold is patterned in the shape of bars atop the bilayer and contacts. Bars that run along the edge of the TES (parallel to unimpeded current flow) ensure that a gold overetch does not leave the boundaries of the TES with critical temperatures higher than the bulk bilayer. Additional bars running transverse to the unimpeded current flow cause regions of the TES below the bars to remain normal by the Superconducting Proximity Effect. Thus, the supercurrent must meander among the normal regions. Introduction of the transverse gold bars has been shown to reduce the slope (dR/dT) of the transition and so decrease the electrothermal feedback of the device. Decreasing the transition slope has been found to mitigate unexplained noise in the TES [43]. Optionally, transverse bars can be put over a section of the contacts (current injection bars). As drawn, the TES is of the one-square, 1400 Å gold bilayer recipe.

## 4.5 Micromachining – Pixel Definition in Monolithic Pop-up Array Structure

The final fabrication steps consist in removing the handle wafer silicon from behind the pixels and patterning the device layer silicon to form the pixels and pixel support structures. Such etching and otherwise patterning silicon for mechanical purposes is known as micromachining. Figure 4.9 illustrates the process. The first step is to remove the device layer from between each of the chips (this step is not shown in Figure 4.9. See Figure 4.2 for the chip layout.). The next step involves masking all the pixels and pixel support structures with PR on the device wafer. This step is called the "front etch". The wafer is then turned upside down and a Deep Reactive Ion Etch removes handle wafer beneath the pixels down to the SOI oxide layer (the etch stop). This step is called the "backetch". After the handle wafer is removed from behind the pixels, the exposed SOI oxide is stripped off with hydrofluoric acid. The remaining device layer, only 1.4 $\mu$m thick, is often called the pixel membrane. Because the device layer was initially removed from between the chips on the wafer, the backetch frees one chip from the next such that the remaining processing can be done on a chip-by-chip basis. In the end, the front etch mask is used to protect the pixels while an etch removes the device layer silicon from around the pixels. The pixels are left, suspended by narrow silicon legs from membrane planks which extend from the rigid handle wafer supported frame. This final step is called the "punch-through" because the etch punches through the membrane where ever the front etch mask does not protect the device layer. The space that remains between each pixel is 5 $\mu$m such that the center-to-center pixel spacing is 1.055 mm. Application of the front etch mask before the backetch is necessary because patterning PR on the thin membrane could potentially rupture the device layer. At this point, all that remains

is to remove the front etch PR, and the chip is finished.

## 4.6 Acknowledgements

The TES chip fabrication as summarized here is described in the ACT detector review documents [4, 5, 7]. The treatment benefitted from many useful correspondences with James Chervenak. Thomas Stevenson calculated the absorber implant profiles, and Edward Wollack oversaw and analyzed the surface impedance test using a Fourier Transform Spectrometer. Suzanne Staggs computed the appropriate target impedances for the ACT absorbers. Early work on the Pop-up Detector micromachining was done by Harvey Moseley, Christine Allen and colleagues, and is documented in [23].

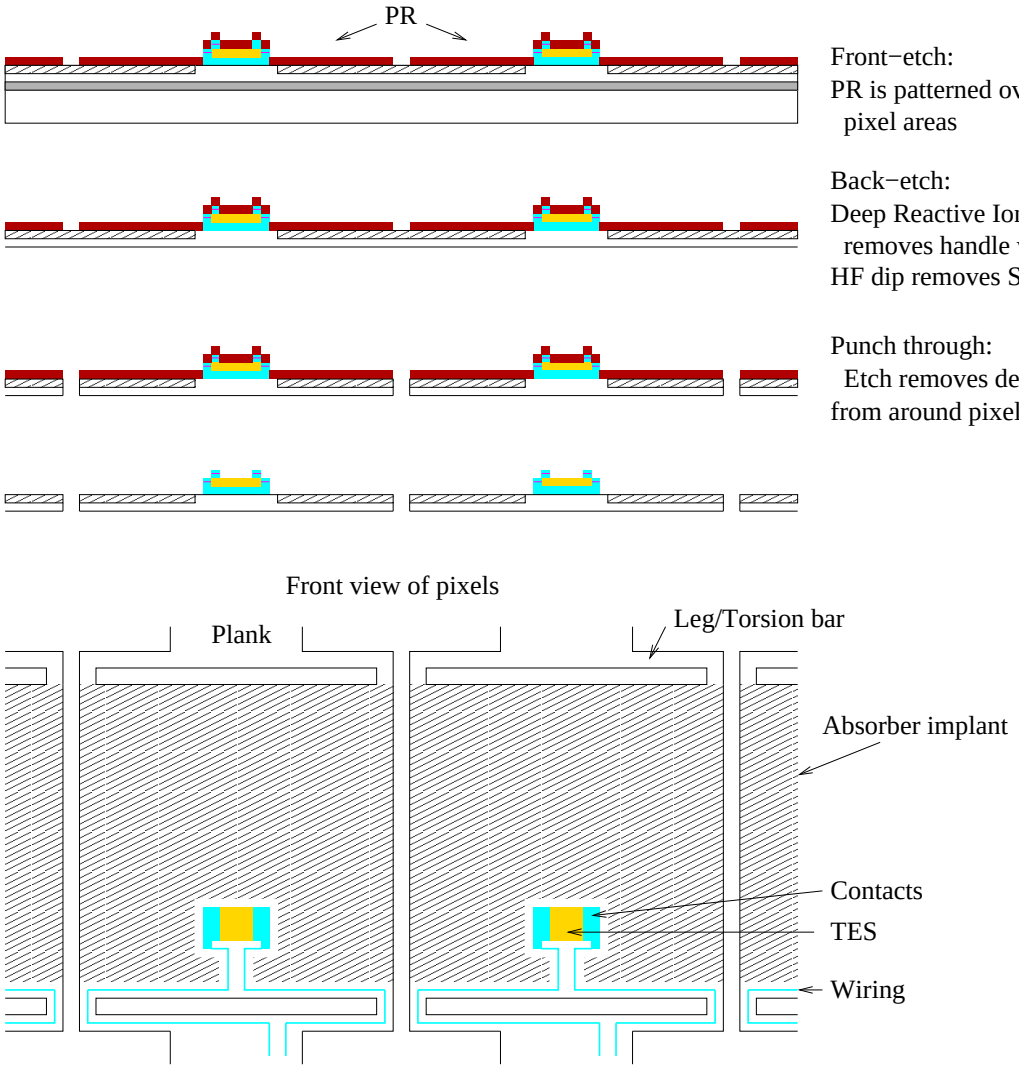


Figure 4.9: **Silicon Micromachining** In the final fabrication steps each pixel is defined as a 1.05 mm square of 1.4 $\mu$m thin device membrane silicon supported by narrow legs extending from membrane planks to the rigid handle wafer of the chip frame. The process begins by patterning a front-etch mask for each pixel on the device layer. Next, the back of the wafer is etched such that both the thick handle wafer silicon and oxide are removed. A Deep Reactive Ion Etch removes the handle wafer, but stops at the oxide. The oxide is removed by hydrofluoric acid. Finally a punch-through etch removes the device silicon from around the pixel bodies and support structures (i.e. legs and planks). The spacing between adjacent pixels is 5 $\mu$m for a 1.055 mm pixel-to-pixel spacing. The TES is 80 $\times$ 75 $\mu$m, 0.5 % of the total pixel area. Drawings are not to scale.

# Chapter 5

# Detector Characterization

## 5.1 Introduction: Tests and Derived Parameters

ACT pixels are integrated onto a silicon chip with thirty-two bolometers per chip. As such, the ACT TESs are tested thirty-two at a time. Figure 5.1 shows the layout of an ACT TES chip. Pixels are numbered zero to thirty-one beginning at the right side of the chip (and excluding the initial heater wiring pixel). The tests described in this section were conducted in a cryostat called the Super Rapid Dip Probe (SRDP) which is the primary testbed for ACT detectors. The SRDP uses a $^3$He adsorption refrigeration system to cool the TES thermal bath to 0.300 K from room temperature in three hours. Custom electronics and software have been assembled to run the SRDP detector tests. The TES tests can be divided into two types: DC tests characterizing the zeroth order circuit parameters ($T_c$,L, $R_s$, $R_n$, $G_o$), and AC tests establishing characteristics of the bolometer that primarily affect the detector response to fluctuations ($\alpha$, $\beta$, heat capacities, small thermal conductances, etc.). The basic detector circuits with parameters to be derived from experiments are reviewed in Figure 5.1. All tests in the SRDP to date have been conducted under conditions where $P_\gamma \approx 0$.

General knowledge of the SQUID amplifier circuitry is beneficial in understanding

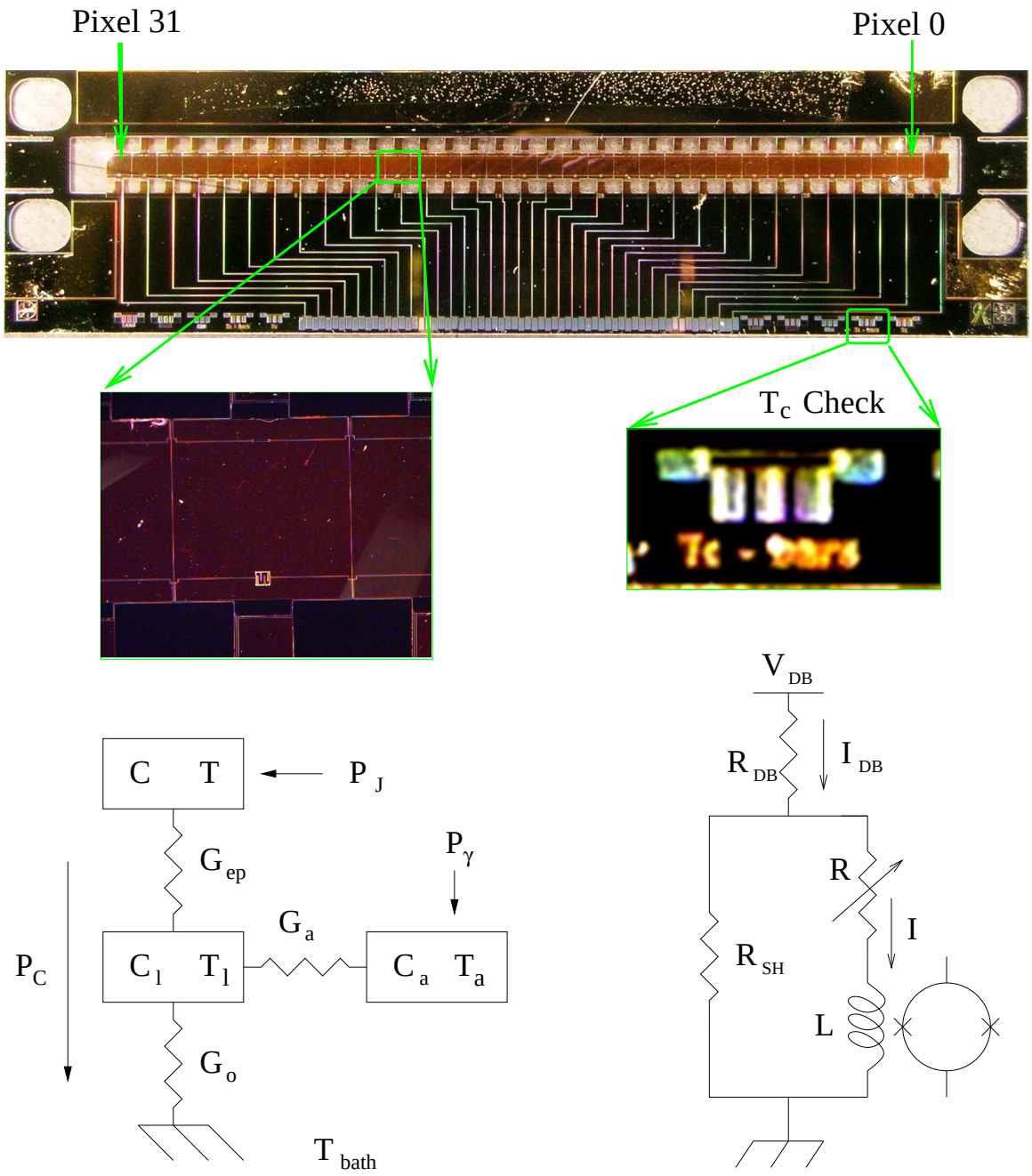


Figure 5.1: **The ACT TES Chip.** The pixels are suspended in the center of the chip and numbered zero to thirty-one from right to left. Each TES chip is tested independently prior to integration into the detector array. Therefore, ACT TESs are tested thirty-two at a time. An additional TES is printed on the frame of the chip for a cross-check measurement of the TES critical temperature (see Section 5.3). Chapter 4 contains more information on the ACT TES chip. The thermal circuit at bottom left details the distributed thermal model used to fit the noise spectrum and complex impedance measurements (Section 5.7). In the thermal circuit, the top block represents the MoAu TES which is loaded by the Joule power of the TES bias voltage. The right-most block is the ion-implant of the pixel absorber which couples to the radiation load power. The middle block is the pixel lattice which joins the absorber and TES to one another and to the cold bath through the thin silicon legs. The legs are the dominant thermal impedance of the circuit, isolating the pixel from the cold bath. In the bottom right is the complementary TES electrical circuit with voltage biasing shunt resistor ($R_s$) in parallel with the TES (R) and magnetic flux

the subtleties of the device characterization. In Section 5.2, the basic SQUID amplifier is described, detailing the open and closed flux-locked loop measurement modes. Once the SQUID readout is established, device characterization begins with the DC tests. First, the resistance dependence of the Johnson current noise spectrum at low frequencies is used to locate the zero-current ($I_o$=0) critical temperature of the device. The zero-current $T_c$ can be cross-checked employing a four-lead resistance measurement to find the temperature at which an on-chip-frame TES film transitions. Measurements of $T_c$ are described in Section 5.3. Next, a measurement is made of the mutual inductance relating the detector bias supply current ($I_{DB}$) to the magnetic flux transduced in the SQUID for two cases: when the TES is 1) superconducting and 2) normal. This open flux-locked loop measurement with TES superconducting (normal) yields the resistance ratios $R_p/R_s$ ($R_p$+$R_n/R_s$) where $R_p$ is a parasitic resistance in series with the TES (Section 5.4). A third measurement determines the resistances $R_s + R_p$ ($R_s + R_p + R_n$) from the Johnson noise current level when the TES is superconducting (normal). In the same measurement of Johnson noise, the roll-off in the spectrum indicates the inductance L, and the noise floor of the measurement is interpreted as being the SQUID noise level $I_{amp}$. Measurements of the TES current-voltage ($I_o$-$V_o$) relation at various bath temperatures $T_b$ then provide a value for $G_o$ and equilibrium points $R_o(T_o,I_o)$ (Section 5.6). Once the basic electrical and thermal circuit parameters are established, the small signal behavior of the TES can be studied at the equilibria $R_o(T_o,I_o)$. Measurements of the TES current noise spectrum and complex impedance may be fit by models to constrain values for $\alpha$, $\beta$, C, $C_l$, $C_a$, $G_k$, and $G_a$ (Section 5.7). Table 5.1 is a summary of the device tests with corresponding device parameter yields.

| Measurement | Detector Parameters Characterized |
|---|---|
| $T_c$ Check | Johnson Noise Change: $T_c$ at $I_o$=0<br>4-Lead Measurement: $T_c$ for off-pixel TES |
| Mutual Inductance<br>Detector Bias to SQUID | TES Superconducting: $R_p/R_s$<br>TES Normal: $(R_p + R_n)/R_s$ |
| Johnson Noise<br>Current Spectrum | TES Superconducting: $R_s + R_p$, $L/(R_s + R_p)$, $I_{amp}$<br>TES Normal: $R_s + R_p + R_n$, $L/(R_s + R_p + R_n)$, $I_{amp}$ |
| $I_o$-$V_o$ Curves | TES Normal: $(R_p + R_n)/R_s$<br>TES on Transition: n, K, $T_o$, $G_o$, $R_o(I_o,T_o)$ |
| Complex Impedance<br>and Noise Spectrum | L, $(R_p + R_n)/R_s$<br>Characterization of TES Responsivity and Sensitivity<br>Model Dependent $\alpha$, $\beta$, Cs, Gs |

Table 5.1: **Summary of Detector Tests and Derived Parameters.** The measurements can be divided into two categories: DC and AC tests. The DC tests consist in The $T_c$ checks, mutual inductance measurements, Johnson noise spectra, and $I_o$-$V_o$ curves which determine either electrical bias circuit parameters or equilibrium operating parameters. The AC tests consist in the complex impedance measurements and noise spectra that measure the response of the bolometers to fluctuations about equilibrium. Model fits of the AC test data, given equilibrium parameters constrained by the DC tests, yield values for first-order parameters such as $\alpha$ and $\beta$.

## 5.2 SQUID Amplifier: Open and Closed Loop Measurements

The output of the (DC) SQUID amplifier is a voltage that is approximately a sinusoidal function of the magnetic flux through the SQUID junction loop (see e.g., [42]). The period of the SQUID voltage is the magnetic flux quantum $\phi_0 = \mathrm{h}/2\mathrm{e} = 2.07 \times 10^{-15}$ Wb, where h is Planck's constant and e is the charge of an electron. A fluctuation in TES current $\delta I$ produces a fluctuation in SQUID flux $\delta\phi = \mathrm{M}_{in}\ \delta I$, where $\mathrm{M}_{in}$ is a constant equal to the mutual inductance of the TES input coil. In order to keep the system response linear, it is important that the resulting change in SQUID voltage be a linear function of flux. In order to linearize the periodic response of the SQUID, a flux-locked loop (FLL) is used. Figure 5.2 illustrates the operation of the FLL. The voltage output of the SQUID is preamplified by a factor $\mathrm{G}_1$ to give a voltage $\mathrm{V}_{SQ}$. The voltage $\mathrm{V}_{SQ}$ is input to a differencing amplifier of which the other input is wired to a fixed voltage $\mathrm{V}_{SET}$. The output of the differencing amplifier drives a second coil, the feedback coil, for coupling magnetic flux to the SQUID. Therefore, with the FLL, a fluctuation in current on the input results in a fluctuation on the feedback coil, which cancels the flux from the input. Cancellation is perfect in the limit that differencing amplifier's gain is infinite. In this limit the input current can be obtained from the feedback current as

$$|\delta I| = \frac{M_{fb}}{M_{in}} |\delta I_{FB}|. \tag{5.1}$$

For the ACT SQUID amplifiers $\mathrm{M}_{fb}/\mathrm{M}_{in}$ is close to fifteen. Equation 5.1 relates $\delta I$ to $\delta I_{FB}$ and not I to $\mathrm{I}_{FB}$ because the FLL has many stable operating points, one for each period of the $\mathrm{V}(\phi)$ response of the SQUID. For example, if $\mathrm{I}_{FB}(\phi)$ is a stable operating feedback current corresponding to a locked SQUID flux $\phi$, then the current $\mathrm{I}_{FB}(\phi + \phi_o)$ also corresponds to a stable operating point.

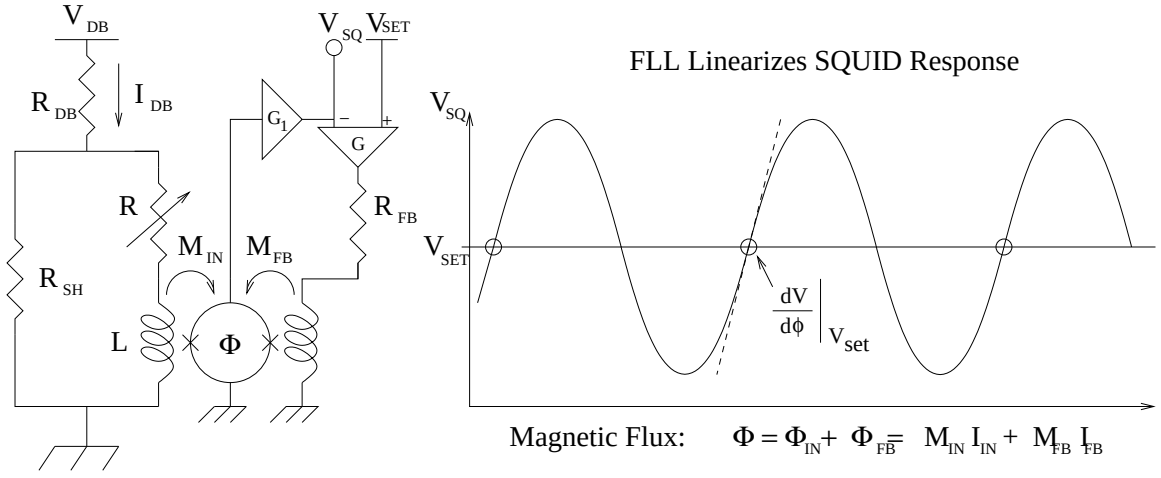


Figure 5.2: **SQUID Flux-Locked Loop.** The open loop voltage response of the SQUID amplifier has sinusoidal dependence on the magnetic flux coupled to the junction loop by the input inductor L. In the flux locked configuration, the output of the SQUID is preamplified ($G_1$) and fed into a differencing amplifier (G). The differencing amplifier output is then transduced back to the SQUID as a feedback flux which, in the limit of high gain G, cancels any fluctuations in flux from the input. Therefore, in a high gain system, the total flux $\Phi$ into the SQUID does not change and the output of the SQUID $V_{SQ}$ is kept in the linear regime at $V_{SET}$. Input current fluctuations are reflected in the feedback current as $\delta I_{IN} = M_{FB}\delta I_{FB} \; / \; M_{IN}$. An important note is that the FLL is stable on any positive slope of the SQUID voltage response, corresponding to a multiplicity of FLL setpoints shown in circles. If follows that the SQUID current measurement is only a relative measurement of device current. Section 5.6 describes a way to calibrate the SQUIDs such that the absolute value of the current may be derived.

It follows from Equation 5.2, that an ideal FLL linearizes the response of the SQUID amplifiers. In other words, the high gain FLL linearizes the SQUID by constraining the amplifier state to a point $V_{SQ} \approx V_{SET}$ such that the slope $dV/d\phi$ of the SQUID response is constant. An alternative amplifier mode is to run open loop. Open loop operation involves disconnecting the feedback coil and reading the SQUID output as $V_{SQ}$. In this mode, the input current fluctuations are interpreted as

$$|\delta I| = \left| \left( \frac{dV_{SQ}}{dI} \right)^{-1} dV_{SQ} \right|. \tag{5.2}$$

It follows that, for accurate operation, the input fluctuations (and input equilibrium state drift) must be small in open loop mode or the factor $dV_{SQ}/dI$ is not a constant.

## 5.3 Critical Temperature

The critical temperature of the on-pixel TES films may be made for zero detector current ($I_o = 0$) by using the Johnson current noise in the detector circuit. The Johnson current spectrum level in the bias loop with loop resistance $R_\ell$ at temperature t is

$$I_J = \sqrt{\frac{4kT}{R_\ell}}, \tag{5.3}$$

where k is Boltzmann's constant. Therefore, Johnson noise in the detector bias loop of Figure 5.1 changes with the total loop resistance as the TES changes from superconducting to normal. Figure 5.5 shows the device current spectra for the superconducting and normal case. At 0.300 K, the TES is superconducting. In this case, the only resistance in the loop is the shunt resistance plus any parasitic/stray resistance that may be present due to nonideal circuitry. The bath temperature is then raised from 0.300 K. Because there is no device current (no Joule power), the pixel should rise at the same temperature as the bath. The Johnson noise initial rises slowly due to the $T^{1/2}$ dependence of the fluctuations. Then, at the critical temperature, the

loop resistance increases to $R_s + R_p + R_n$, and the noise level drops by a factor approximately equal to the square root of the ratio of the TES normal resistance to shunt resistance ($20^{1/2}$ or higher). The abrupt noise level change signals that the current bath temperature (and thus pixel temperature) is the $T_c$ of the device under question. An important assumption of this measurement, and of all others that follow, is that the loading on the pixel due to stray radiation in the test cryostat is negligible (i.e. $P_\gamma \ll 1$ pW). The presence of radiation loading would bias the $T_c$ measurement described here to lower temperatures, since radiation would raise the actual pixel temperature above the bath temperature. Figure 5.3 shows critical temperatures measured using Johnson currents for pixels on ACT TES chip X.3-2.

To confirm that the on-pixel device $T_c$ measurements are not biased by radiation loading or other systematic effects, TES films are printed on the frame of the chip so as to be well thermally anchored to the bath. A four-lead resistance measurement may then be used to monitor the on-frame TES film resistance and locate at which bath (and therefore film) temperature the device transitions. The results of the four-lead $T_c$ check on chip X.3-2 was 0.543 K. This number is $\sim 2\%$ higher than Johnson noise derived $T_c$s (Figure 5.3) for nearby pixels (in the neighborhood of pixel number 0). The difference is consistent with a bias due to radiation loading. A second possible explanation of the difference in measured critical temperatures is that the mechanical stress on the TES film is different on the pixel membrane than on the chip frame. Bilayer $T_c$s can be changed with mechanical stress. Finally, a second TES, X.1-4 from the same wafer as X.3-2, was tested by Thomas Stevenson of NASA Goddard using a four-lead measurement. Only on-frame TES films were checked.

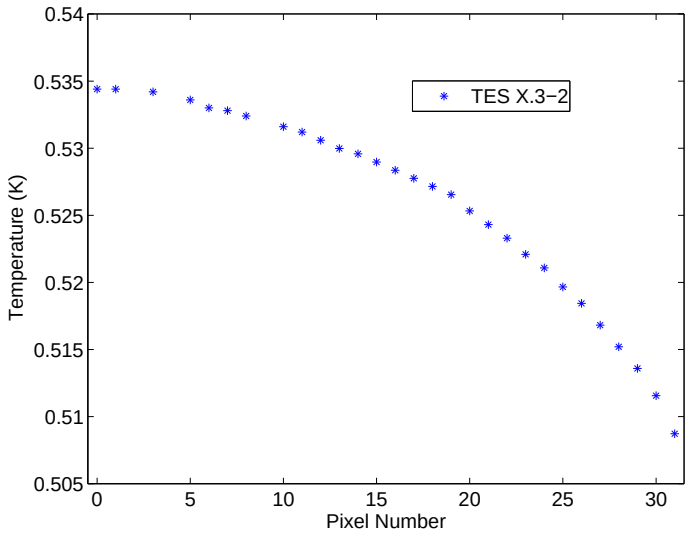


Figure 5.3: **Critical Temperature Measurements at Zero Current.** The critical temperature (y-axis) was measured for pixels on TES chip 3-2 of wafer X (X.3-2). The x-axis lists the pixel numbers. Pixels with missing data suffered a malfunction in the pixel itself or in the associated SQUID amplifier. To measure the critical temperature, the TES bias is turned off (zero current) so that the pixel would thermalize with the cold bath. The bath temperature is then raised while the Johnson current of the TES bias loop is monitored with the FLL SQUID amplifier. When the bath temperature reaches the critical temperature of the TES, the TES resistance increases from zero to the normal resistance. This causes a change in the Johnson noise spectrum, the level of which is inversely proportional to the square root of the total TES bias loop resistance. The bath temperature at which the Johnson noise current spectrum changes is taken to be the TES critical temperature. Figure 5.5 shows the difference between the bias loop Johnson noise levels corresponding to normal and superconducting TESs. The decrease in $T_c$ with pixel number is a result of the higher-numbered pixels being closer to the edge of the wafer where the molybdenum of the TES MoAu bilayer is thinner (see Figure 4.5).

## 5.4 Mutual Inductance (SQUID Period) Measurements

The TES bias circuit is a current divider: the bias supply current $I_{DB}$ splits such that $I_o$ passes through the TES, any parasitic resistance, and the SQUID inductor, and $I_s = I_{DB}$ - $I_o$ passes across the shunt resistor. The current $I_{DB}$ should divide such that

$$I_o = \frac{I_{DB}}{1 + (R_p + R)/R_s}, \tag{5.4}$$

where $R = R_n$ ($R = 0$) when the TES is normal (superconducting). Figure 5.4 shows the current divider circuit. Also shown in the figure is the dark SQUID circuit. Each SQUID amplifier/multiplexer chip has a thirty-third SQUID channel, the input of which is wired directly to a current source. In this way, a direct measurement of the input mutual inductance $M_{in} = \Delta I_o/\phi_o$ can be made. The mutual inductance is simply the period (in Amperes) corresponding to one period of the SQUID V-$\phi$ response curve. Defining a bias current supply mutual inductance $M_{DB} = \Delta I_{DB}/\phi_o$, Equation 5.4 can be rewritten

$$M_{DB} = \frac{M_{IN}}{1 + (R_p + R)/R_s}. \tag{5.5}$$

If parasitic resistances are zero, one should measure $M_{DB} = M_{IN}$ in the superconducting state. All measurements of $M_{DB}$ in ACT detector bias circuits have equaled $M_{IN}$ to within the limits of systematic errors of the test setup ($\sim 10\ \mu\Omega$). The reason that parasitics would not be expected in the ACT bias circuit is that all metals in the circuit are superconducting at the device temperatures. An example measurement of $M_{IN}$ and $M_{DB}$ (TES superconducting and normal), in the form of SQUID V-$\phi$ response periods, is shown in Figure 5.4 for a TES.X.3-2 pixel. The input mutual inductance is a characteristic $\sim 6\ \mu A/\phi_o$ which is indistinguishable from $M_{DB}$ in the case for which the TES is superconducting. Given $R_p = 0$, the measurement of

$M_{DB}$ in the normal case gives $R_n/R_s \approx 60$. The result $R_p$=0 simplifies the analysis of the bolometers. The absence of parasitic resistance significantly improves device operation when the shunt resistance is small, as in the case of the ACT 0.65 mΩ shunts.

## 5.5 Johnson Noise Current Spectrum

The Johnson noise current spectrum in the detector loop is a useful diagnostic for determining the electrical circuit parameters ($R_s$, $R_n$, L) and the SQUID amplifier noise level $I_{amp}$. In the superconducting and normal states of the TES, the current noise in the device bias loop is dominated by Johnson noise. In Section 5.3 it was explained how the Johnson noise can be used to find the device critical temperature. The $T_c$ measurement is possible because the Johnson current noise spectrum level is given by $(4kT/R_\ell)^{1/2}$ which changes abruptly with the bias loop resistance $R_\ell$ at the superconducting transition. A single pole with 3dB frequency $R_\ell$ rolls off the Johnson current noise until it drops below the SQUID amplifier noise floor $I_{amp}$. Therefore, assuming the system temperature T is known, $R_s$, $R_n$, L, and $I_{amp}$ can be constrained by fitting a model to the bias loop current noise spectrum, first with the TES superconducting, then with the TES normal. The model for the fit is shown in Figure 5.5

$$I(\nu) = \sqrt{\left(\frac{4kT/R_\ell}{1 + i2\pi f L/R_\ell}\right)^2 + I_{amp}^2}, \tag{5.6}$$

where f is the frequency and $R_\ell = R_s + R_p$ when the TES is superconducting, and $R_\ell = R_s + R_p + R_n$ when the TES is normal. In Section 5.4 it was shown that the parasitic resistance $R_p$ is small compared to the shunt resistance. It follows that the fit to Johnson noise can be interpreted straightforwardly as giving $R_s$ and $R_n$ without confusion from parasitics. If parasitics did exist at a non-negligible level, however, the

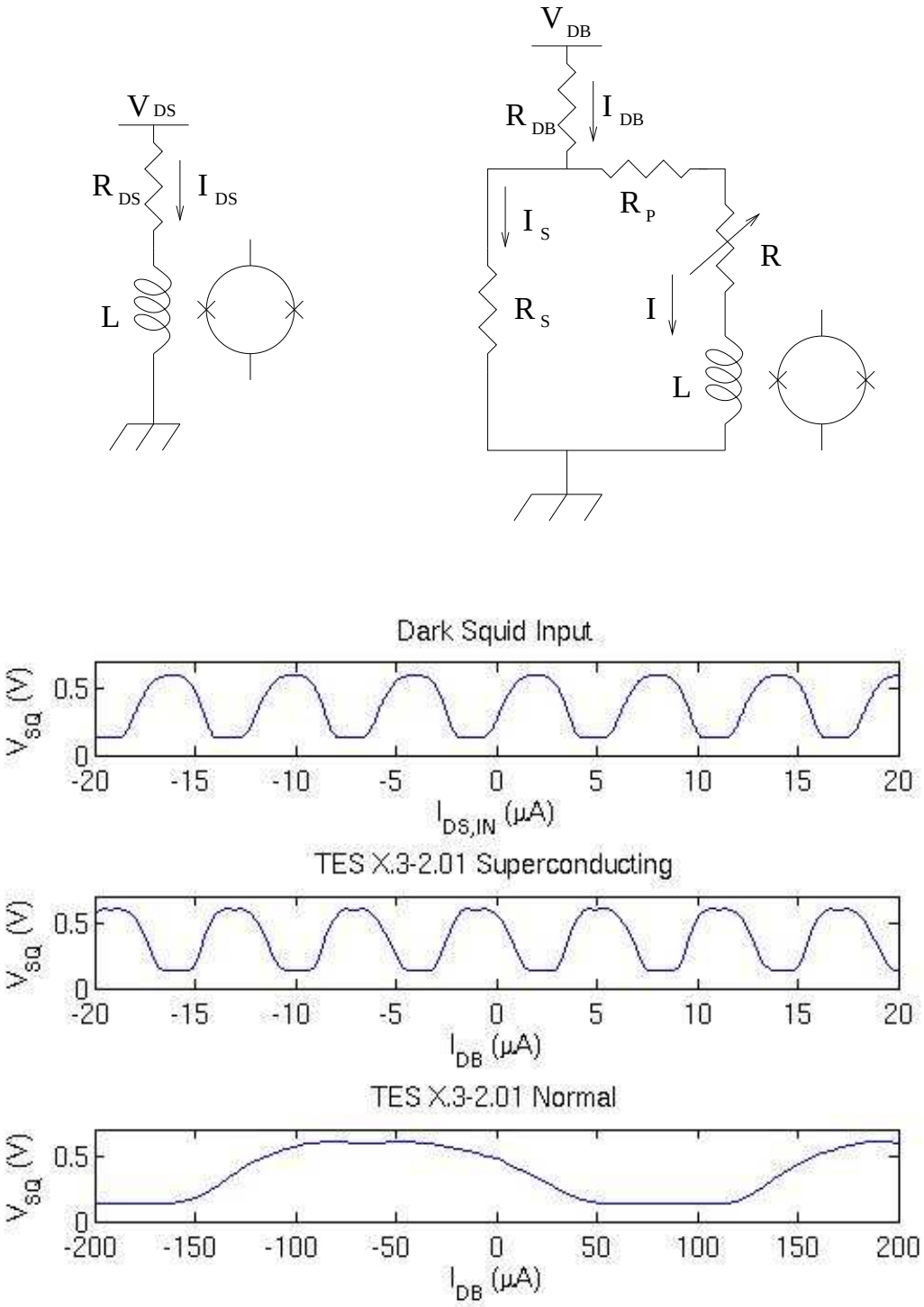


Figure 5.4: **Mutual Inductance Measurement.** The mutual inductance of the input coil L to the SQUID amplifier as measured by the SQUID period versus $I_{DS}$ (top graph) can be obtained with the dark SQUID circuit (upper left schematic). In the bias circuit (upper right schematic) with the TES superconducting, the period of the SQUID response with respect to $I_{DB}$ (middle graph) is the same as for the dark SQUID, indicating the parasitic resistance $R_p$ in the bias circuit is zero. Finally, a measurement of the SQUID period versus $I_{DB}$ with a normal TES yields $R_n/R_s$.

noise measurements described here along with the mutual inductance measurements described in Section 5.4 could be used to disentangle $R_s$, $R_p$, and $R_n$. Figure 5.5 shows an example of a Johnson noise measurement for TES pixel X.3-2.01 along with models fit to the data.

## 5.6 $I_o$-$V_o$ Curve Measurements

Characterization of the current-voltage relation of the TES is useful for three primary reasons. First, the thermal conduction $G_o(T)$ of the thin silicon legs can be measured. Second, the saturation power of the detectors can be computed given a bias current $I_{DB}$. And thirdly, the derived equilibrium points $R_o(I_o,T_o)$ are essential for interpreting the device response to fluctuations. The shape of the TES $I_o$-$V_o$ curve can be divided into three parts: the normal branch, the transition, and the superconducting branch. Each part is considered in turn below, followed by a practical guide to acquiring $I_o$-$V_o$ curves and finally the interpretation of the data.

When the TES is normal, the device is a simple resistor. Therefore, the current-voltage relation is a line passing through zero current/voltage with a slope equal to the normal resistance. Figure 5.6 shows a family of IV curves for pixel X.3-2.01 in which the right most section of the curves follows the linear $I_o$-$V_o$ relation for a normal resistance $R_n = 0.032\ \Omega$.

As the voltage $V_o$ is lowered, the temperature of the pixel T decreases with the Joule heating $V_o^2/R_n$. When T reaches $T_c$, the device enters the superconducting transition. As $V_o$ is decreased further, the temperature continues to drop and the resistance falls with the sharp slope dR/dT of the transition. As discussed in Section 3.3, the power conducted by the $G_o$ thermal link when the device is on transition is approximately constant assuming $T_c \gg n\Delta T$ ($n \approx 4$), $\beta \ll 1$, and $T_b^n \ll T_c^n$ where $\Delta T$ is the temperature span of the transition. All of these are reasonable assumptions

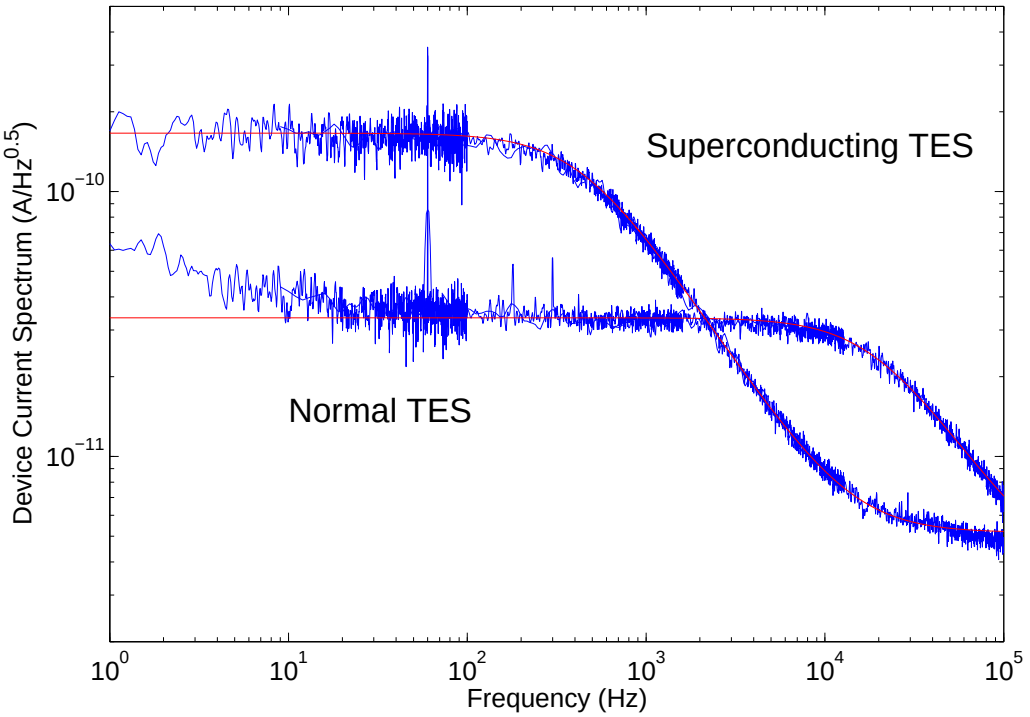


Figure 5.5: **Johnson Noise Current Spectrum Measurement of a TES.** The current spectrum due to Johnson noise in the TES bias loop (left) is white with a level $(4k_bT/R_\ell)^{0.5}$, where T is the temperature of the bias loop and $R_\ell$ is the total resistance of the bias loop. The Johnson noise current spectrum rolls off with a single pole with 3dB frequency $R_\ell/2\pi L$. The SQUID amplifier noise, in units of equivalent detector loop current, adds in quadrature with the Johnson noise. The SQUID noise spectrum is white with a $\sim 4$ pA/Hz$^{0.5}$ level. The data presented is for pixel 1 of TES X.3-2. The superconducting (normal) data were taken at T = 0.316 K (T = 0.567 K). For the superconducting (normal) data, $R_\ell = 0.00063\ \Omega$ (0.0284 Ω), L = 234 nH (237 nH), $I_{amp} = 5.2$ pA/Hz$^{0.5}$ (3.45 pA/Hz$^{0.5}$). As discussed in Section 5.4, $R_p \ll R_s$ so that $R_\ell \approx R_s$ ($R_s + R_n$) with the TES superconducting (normal).

under normal operating conditions. For the device tests there is no radiation power to load the pixels so the Joule power must equal the conducted power:

$$P_{J,o} = I_o V_o = K(T^n - T_b^n). \tag{5.7}$$

It follows that the Joule power is nearly constant across the transition. Since $P_J = IV$, the current-voltage relation for the transition should resemble a hyperbola as shown by the transition region of the $I_o$-$V_o$ curves in Figure 5.6.

The final section of the TES $I_o$-$V_o$ curve corresponds to the point where the device falls off the transition into the superconducting state. As shown by the stability condition following from Equation 3.20, this occurs when $R = R_s$. At this point the voltage across the device goes to zero and the temperature drops to the bath temperature.

In practice, the quantities that are known and needed by the experimenter are the bias supply current $I_{DB}$, the SQUID FLL feedback current $I_{FB}$ (Section 5.2), and the shunt resistance $R_s$ (Section 5.5). As discussed in Section 5.2, the device current $I_o$ is a linear function of $I_{FB}$ in an ideal FLL:

$$I_o = \frac{M_{FB}}{M_{IN}} I_{FB} - I_{offset} \equiv I'_o - I_{offset}, \tag{5.8}$$

where $M_{FB}$ and $M_{IN}$ are the mutual inductances of the feedback and input SQUID coils and $I_{offset}$ is the arbitrary offset of the feedback current measurement resulting from the multiplicity of stable FLL states. It follows from Equation 5.8 that $\Delta I_o = \Delta I'_o$. Therefore, changes in the device voltage can be computed as

$$\Delta V_o = (\Delta I_{DB} - \Delta I'_o) R_s. \tag{5.9}$$

In the normal branch of the $I_o$-$V_o$ then the normal resistance may be computed as

$$R_n = \Delta V_{o,n} / \Delta I'_{o,n} = \left( \frac{\Delta I_{DB,n}}{\Delta I'_{o,n}} - 1 \right) R_s, \tag{5.10}$$

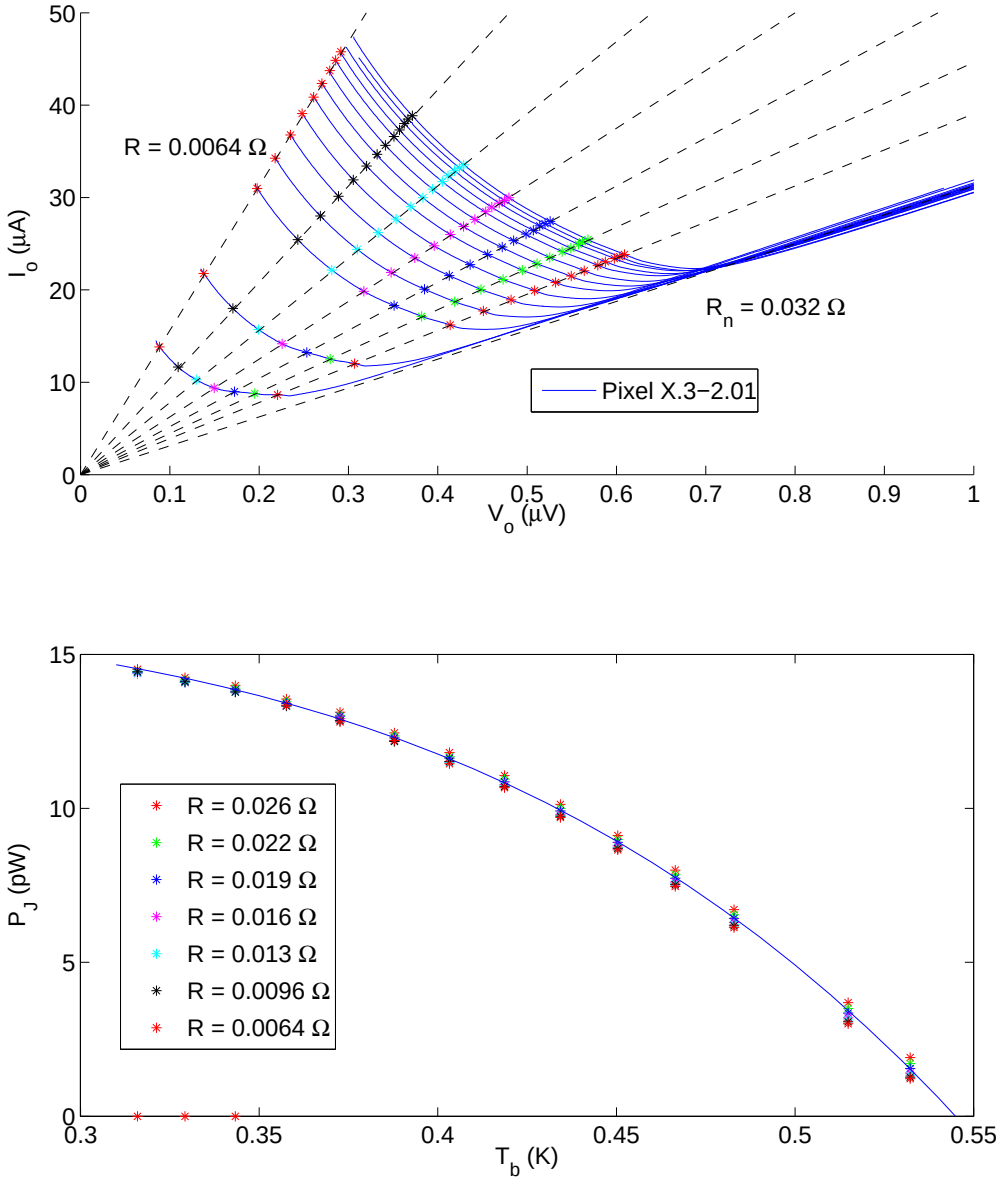


Figure 5.6: **$I_o$-$V_o$ Measurement.** The $I_o$-$V_o$ data graphed above is for pixel X.3-2.01 which has a $T_c$ of 0.535 K and 5 $\mu$m silicon legs between the bolometer and the cold bath. The top graph shows $I_o$-$V_o$ curves, taken at various bath temperatures $T_{b,m}$. The nearly hyperbolic relation between current and voltage in the upturned transition region is apparent. Dashed lines of constant resistance $R_n$ intersect the $I_o$-$V_o$ in the transition region, picking out operating points ($I_{o,m,n}$,$R_n$) (color-coded) on each $I_o$-$V_o$ curve. In the bottom plot, the Joule power as a function of $T_b$ for each resistance $R_n$, $P_{J,n}(T_{b,m})=I_{o,m,n}R_n$, is fit with a model giving a thermal conductance for the legs of $G_o$ = 126 pW/K. Responsivities derived from the model parameters of this table were used in Chapter 3 to illustrate the response bandwidths of ACT detectors.

where the 'n' subscript has been used to denote quantities recorded for the normal branch of the $I_o$-$V_o$ curve. With the normal resistance determined, the absolute value of the device voltage $V_{o,n}$ and current $I_{o,n}$ may be computed:

$$V_{o,n} = \frac{I_{DB,n} R_n}{1 + R_n/R_s}, \tag{5.11}$$

and

$$I_{o,n} = \frac{V_{o,n}}{R_n}. \tag{5.12}$$

Thus, on the normal branch, the value for $I_{offset} = I'_{o,n}$ - $I_{o,n}$ can be computed, and the absolute value of $I_o = I'_o + I_{offset}$ is then known throughout the entire $I_o$-$V_o$ curve. Written out in terms of measured quantities, the device current is

$$I_o = \frac{M_{FB}}{M_{IN}} I_{FB} - \left( \frac{M_{FB}}{M_{IN}} I_{FB,n} - \frac{I_{DB,n}}{1 + R_n/R_s} \right). \tag{5.13}$$

Once $I_o$ is known, $V_o$ for any point on the $I_o$-$V_o$ curve is simply

$$V_o = (I_{DB} - I_o) R_s. \tag{5.14}$$

The standard $I_o$-$V_o$ measurement consists of taking multiple $I_o$-$V_o$ curves at bath temperatures ranging from the base temperature ($\sim$ 0.300 K) up to just below the device's critical temperature. The measurement at the top of Figure 5.6 is exactly this. The $I_o$-$V_o$ curves share the same normal branch, but the hyperbolic curve of the transition region is closer to the $I_o$-$V_o$ origin for the data collected at higher $T_b$. This behavior is understood in the context of Equation 5.7 as the Joule power $I_o V_o$ decreases with higher bath temperature.

The first piece of information that may be derived from the $I_o$-$V_o$ measurement is the detector saturation power – the radiation loading which heats the TES into the normal state. The $I_o$-$V_o$ curve at the base temperature gives the operating Joule power in the absence of radiation loading. This Joule power equals the power $P_{c,o}$ that flows down the narrow silicon legs through the thermal conductance. Therefore,

Equation 3.11 can be used to calculate the saturation power. In Figure 5.6, the $I_o$-$V_o$ curve at $T_b = 0.315$ K indicates $P_{c,o} = 15$ pW. If the device resistance when no radiation loads the detector is chosen to be 6.4 m$\Omega$ (20% of $R_n$), then the saturation power is 13 pW.

Another result of the $I_o$-$V_o$ measurement is a determination of the conductivity $G_o$ of the narrow silicon legs connecting the pixel to the bath. With $I_o$-$V_o$ curves for several bath temperatures, the data can be rearranged to find $P_J$ as a function of $T_b$. This data can be fit with the model described by Equation 5.7 to estimate $T_c$, n, and K. The thermal conductance $G_o$ follows as $nKT_c^{n-1}$. Figure 3.3 shows $P_{c,o}$ and $G_o$ measurements for pixels of various leg widths. The bottom graph in Figure 5.6 shows the $P_J$ versus $T_b$ relation for pixel X.3-2.01 which has 5 $\mu$m wide legs. The model line through the data gives a $G_o$ of 127 pW/K.

A third product from the $I_o$-$V_o$ curves is collection of equilibrium points. Given a K and n from the $P_J(T_b)$ fit described in the previous paragraph, Equation 5.7 can be used to assign a temperature to each $I_o$-$V_o$ point. In this way, an estimation of the transition surface in the region of the points $R_o(I_o,T_o)$ can be obtained. This surface has proven, in practice, difficult to construct in a self-consistent way. Despite the difficulty in obtaining a more general description of the transition, measured equilibrium points $R_o$ and $I_o$, along with an estimated $T_o$, are established. From these well characterized operating points, the response of the bolometer to small fluctuations are studied as described in the next section.

## 5.7 Complex Impedance and Noise Measurements

Complex impedance and noise measurements begin with an $I_o$-$V_o$ curve (Section 5.6). The first graph in Figure 5.7 shows how the device voltage is swept and stopped at preselected operating points. At each operating point both complex impedance and

noise data are captured. The essential measurement concept is that impedance and noise should be taken at the same operating points for efficient comparison to detector models. To more fully explore the device response, multiple $I_o$-$V_o$ curves at different bath temperatures may be taken to obtain operating points at various Joule powers in addition to a range of resistances and currents.

The more straight forward of the two measurements is the noise data acquisition. At each preselected bias point along the $I_o$-$V_o$ curve, noise is acquired simply by taking the power spectrum of the feedback current and using the appropriate factors to convert the data to an equivalent device current spectrum. For the data presented in this work, noise spectra were acquired with an HP 35670A Dynamic Signal Analyzer. The second graph in Figure 5.7 shows the noise spectra at each operating point selected in the corresponding $I_o$-$V_o$ curve. The level of the current spectrum increases with the responsivity as the device voltage drops. Therefore, the noise spectra show the device speeding up as the current, and therefore the TES electrothermal feedback loop gain, increases. As the detector speeds up, increased interaction of the various thermal systems causes the excess noise at intermediate frequencies to rise. The apparent "clumping" of different noise spectra may be related to abnomalities observed in the transition of detector X.3-2.01.

The complex impedance measurement takes place at the same operating points as the noise measurement. In terms of measureable quantities, the impedance is defined

$$Z(\omega) = \frac{\delta I_{DB}(\omega) R_s}{\delta I_o(\omega)} \tag{5.15}$$

where $\delta I_{DB}(\omega)$ is the current spectrum of an AC signal on the detector bias current supply, and $\delta I_o(\omega)$ is the spectrum of the device current response. The measurement is set up as in Figure 5.8. The voltage noise source of the HP 35670A Dynamic Signal Analyzer is converted to a current by the external detector bias resistor $R_{EDB}$. This current with spectrum $\delta I_{DB}(\omega)$ is coupled onto the detector supply current $I_{DB}$

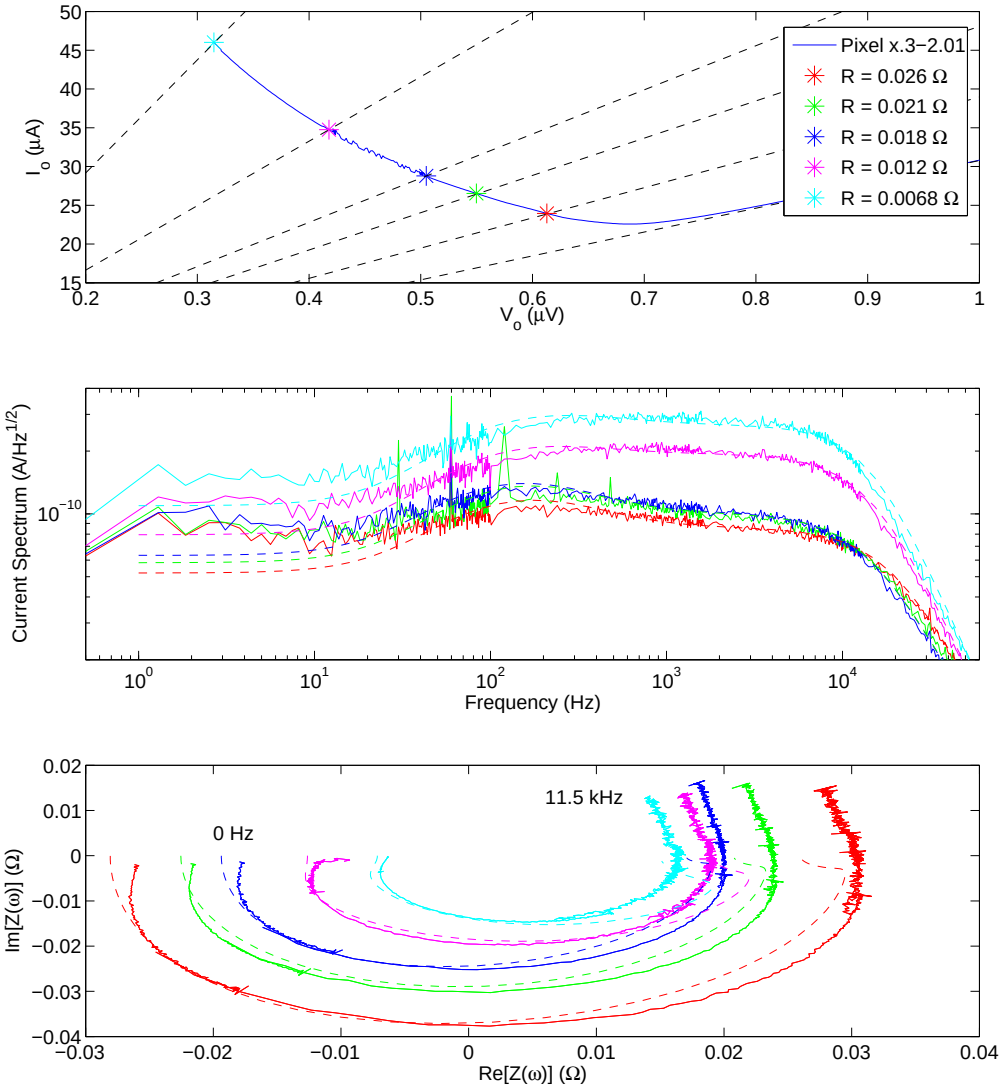


Figure 5.7: **Noise and Complex Impedance Measurements.** Noise spectra (middle) and complex impedance (bottom) data were obtained at five different operating points on the transition of ACT pixel X.3-2.01. The operating points are color-coded and correspond to the starred points along the $I_o$-$V_o$ curve at top. The data are taken at a bath temperature of $T_b$ where the pixel has $\sim 15$ pW of conducted power to the bath. All tests were done under dark $P_\gamma$=0 conditions. Both the complex and the noise data display evidence of a distributed thermal circuit on the pixel. Model fits are plotted as dashed lines and color-coded to match the corresponding data. The model used for the fit is illustrated in Figure 5.1, and the parameter results of the fits are given in Table 5.7. The model curves for noise plotted in the middle graph were used to illustrate detector sensitivities in Chapter 3.

| Parameter | $R_o/R_n$ | | | | |
|---|---|---|---|---|---|
| | 78% | 64% | 53% | 37% | 21% |
| $I_o$ ($\mu$A) | 24.322 | 26.829 | 28.857 | 34.717 | 46.044 |
| $V_o$ ($\mu$V) | 0.617 | 0.555 | 0.506 | 0.423 | 0.316 |
| $R_o$ (m$\Omega$) | 25.376 | 20.690 | 17.533 | 12.194 | 6.861 |
| $T_o$ (K) | 0.538 | 0.537 | 0.535 | 0.535 | 0.534 |
| $T_l$ (K) | 0.537 | 0.536 | 0.534 | 0.535 | 0.533 |
| $T_a$ (K) | 0.537 | 0.536 | 0.534 | 0.535 | 0.533 |
| $T_b$ (K) | 0.309 | 0.308 | 0.308 | 0.307 | 0.306 |
| $\alpha$ | 92.560 | 108.111 | 91.479 | 338.143 | 354.160 |
| $\beta$ | 0.023 | 0.002 | -0.031 | 0.553 | 1.184 |
| $C_o$ (pJ/K) | 1.505 | 1.887 | 1.634 | 2.148 | 1.439 |
| $C_l$ (pJ/K) | 0.222 | 0.384 | 0.273 | 0.566 | 0.275 |
| $C_a$ (pJ/K) | 1.190 | 1.329 | 1.254 | 1.186 | 1.236 |
| $G_{ep}$ (pW/K) | 2.77e+04 | 3.17e+04 | 3.03e+04 | 4.92e+04 | 2.9e+04 |
| $G_a$ (pW/K) | 788.572 | 935.042 | 743.373 | 611.172 | 755.850 |
| $G_o$ (pW/K) | 128.954 | 128.092 | 126.340 | 126.825 | 125.877 |

Table 5.2: **Model Fit Parameters for Noise and Complex Impedance Data.** This table shows the model parameters describing the circuit in Figure 5.1 as fit to the X.3-2.01 data in Figure 5.7. The data are listed for the five operating points shown in the $I_o$-$V_o$ curve at the top of Figure 5.1 and listed at the top of the table. As expected, the temperatures of the absorber, lattice and TES are nearly the same because the the on-pixel thermal conductivities $G_{ep}$ and $G_a$ are much larger than the thermal conductivity of the narrow silicon legs $G_o$. The heat capacities $C_o$, $C_l$, and $C_a$ are reasonable for the TES electron, the pixel phonons, and the absorber electrons, respectively. The jump in $\alpha$ between the 17 m$\Omega$ and 12 m$\Omega$ operating pionts is consistent with the "clumping" of the data in Figure 5.1, and indicates that the transition of the MoAu bilayer is not smooth. At low frequencies ($\leq$ 10 Hz), the bolometer acts as a lumped thermal mass with heat capacity $C_o$ + $C_l$ + $C_a$ and a thermal link to the bath of $G_o$. The model fit parameters for X.3-2.01 are provided by Rolando Dunner.

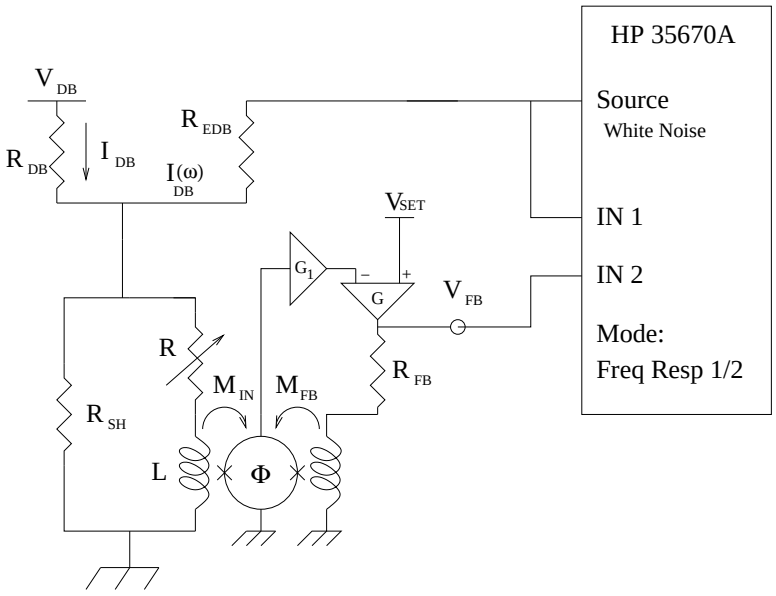


Figure 5.8: **Apparatus for Complex Impedance Measurements.**

at a current summing junction before being injected into the TES bias circuit. For the measurements presented in this work, the HP source was set to produce a white noise spectrum. Into the spectrum analyzer are put both the source noise and the corresponding fluctuations in device current readout through the feedback voltage. The analyzer then performs an optimal averaging of the ratio of the two signals to obtain the complex impedance. The bottom graph in Figure 5.7 shows the resulting impedance measurements at the preselected operating points.

## 5.8 Acknowledgments

The SRDP testbed was designed and assembled by Norman Jarosik. Rolando Dunner has made significant contributions to device characterization at Princeton, and proveded the model data The TES characterization described in this chapter roughly follows the prescription in [25]. The SRDP testbed was designed and assembled by

Norman Jarosik. Adam Hincks has written the latest version of the SRDP control software. Rolando Dunner has made significant contributions to the flux-locked loop hardware design. Actual device testing in the SRDP has been carried out by Rolando Dunner, Adam Hincks, Anson Hook, Yue Zhao, and others. Michael Niemack has performed similar device tests for ACT TESs in the ACT telescope prototype cryostat CCAM. Randy Doriese, Barry Zink, Harvey Moseley, James Chervenak, Dominic Benford, and Johannes Staguhn also provided advice.

# References


[1] N. W. Ashcroft and N. D. Mermon. *Solid State Physics*. Thomson Learning, 1976.

[2] C. L. Bennet et al. 4-year COBE DMR Cosmic Microwave Background observations: Maps and basic results. *ApJL*, 464:L1, 1996.

[3] C. L. Bennet et al. First year Wilkinson Microwave Anisotropy Probe (WMAP) observations: Preliminary maps and basic results. *ApJS*, 148:63, 2003.

[4] J. A. Chervenak. Preliminary Design Review of ACT detector arrays. Internal ACT PDR1 Document, 2004.

[5] J. A. Chervenak. Component fabrication for camera 1 of MBAC for ACT. Internal ACT PDR2 Document, 2005.

[6] J. A. Chervenak. Personal Communication, 2006.

[7] J. A. Chervenak. Design review of bolometer arrays for ACT. Internal ACT CDR Document, 2006.

[8] J. A. Chervenak et al. Fabrication of transition edge sensor X-ray microcalorimeters for Constellation-X. *Nucl. Instr. and Meth. A*, 520:460, 2004.

[9] R. H. Dicke et al. Cosmic black-body radiation. *ApJ*, 142:414, 1965.

[10] D. J. Fixsen et al. Calibrator design for the COBE Far Infrared Absolute Spectrophotometer. *ApJ*, 512:511, 1999.

[11] D. J. Fixsen et al. The temperature of the Cosmic Microwave Background at 10 GHz. *ApJ*, 612:86, 2004.

[12] J. W. Fowler. ACT sky coverage Study. Internal ACT Memo, Oct. 2004.

[13] J. W. Fowler. ACT filter passbands. Internal ACT Memo, 2006.

[14] J. W. Fowler, W. B. Doriese, T. A. Marriage, H. T. Tran, , et al. Cosmic microwave background observations with a compact heterogenious 150 GHz interferometer in Chile. *ApJS*, 156:1, 2005.

[15] M. Galeazzi and D. McCammon. Microcalorimeter and bolometer model. *J. Appl. Phys.*, 93:4856, 2003.

[16] G. C. Hilton et al. Microfabricated transition-edge X-ray detectors. *IEEE Trans. Appl. Supercond.*, 11:739, 2001.

[17] G. Hinshaw et al. First year Wilkinson Microwave Anisotropy Probe (WMAP) observations: the angular power spectrum. *ApJS*, 148:135, 2003.

[18] G. Hinshaw et al. Three-Year Wilkinson Microwave Anisotropy Probe (WMAP) observations: Temperature results. submitted, 2006.

[19] K. D. Irwin and G. C. Hilton. Transition Edge Sensors. In *Cryogenic Particle Detection*. Springer, 2005.

[20] C. L. Kuo et al. High resolution observations of the CMB power spectrum with ACBAR. *ApJ*, 600:32, 2004.

[21] J. W. Lamb. Miscellaneous data on material for millimeter and submillimeter optics. *Int. J. Infrared and Millimeter Waves*, 17:1997, 1996.

[22] J. Lau et al. Millimeter-wave antireflection coating for cryogenic silicon lenses. *Appl. Opt.*, 45:3746, 2006.

[23] M. J. Li et al. Fabrication of Pop-up Detector arrays on Si wafers. In *SPIE Proc. on Micromachining and Microfabrication*, number 3874 in Proc. of SPIE, page 422, 1999.

[24] M. A. Lindeman. *Microcalorimetry and the Transition-Edge Sensor*. PhD thesis, University of California at Davis, 2000.

[25] M. A. Lindeman et al. Impedance measurements and modeling of a transition-edge-sensor calorimeter. *Rev. Sci. Inst.*, 75:1283, 2004.

[26] J. Lindhard, M. Scharff, and H. E. Schiott. Range concepts and heavy ion ranges. (notes on atomic collisions, ii). *Mat. Fys. Medd. Dan Vid. Selsk.*, 33:1, 1963.

[27] Z.-Y. Liu. 225 GHz atmospheric receiver – user's manual. ALMA Memo 41, 1987.

[28] T. A. Marriage. Radiation loading for an ACT bolometer. Internal ACT Memo, Apr. 2004.

[29] T. A. Marriage, J. A. Chervenak, and W. B. Doriese. Testing and assembly of the detectors for the Millimeter Bolometer Array Camera on ACT. *Nucl. Inst. Meth. Phys. A*, 559:551, 2006.

[30] B. S. Mason et al. The anisotropy of the microwave background to l = 3500: Deep field observations with the Cosmic Background Imager. *ApJ*, 591:540, 2003.

[31] A. D. Miller et al. A measurement of the angular power spectrum of the CMB from l - 100 to 400. *ApJL*, 524:1, 1999.

[32] L. A. Page et al. First year Wilkinson Microwave Anisotropy Probe (WMAP) observations: Interpretations of the TT and TE power spectrum peaks. *ApJS*, 148:233, 2003.

[33] J. R. Pardo et al. Atmospheric transmission at microwaves (ATM): an improved model for millimeter/submillimeter applications. *IEEE TAP*, 49:1683, 2001.

[34] V. V. Parshin et al. Silicon as an advanced window material for high power gyrotrons. *Int. J. Infrared and Millimeter Waves*, 16:864, 1995.

[35] A. A. Penzias and R. W. Wilson. A measurement of excess antenna temperature at 4080 Mc/s. *ApJ*, 142:419, 1965.

[36] W. H. Press et al. *Numerical Recipes in C*. Cambridge University Press, 1992.

[37] S. J. E. Radford. Site characterizations for mm/submm astronomy. In *ASP Conf. Ser.*, number 266, page 148, 2002.

[38] S. J. E. Radford et al. Atmospheric transparency at Chajnantor and Pampa la Bola. ALMA Memo 384, 2001.

[39] D. N. Spergel et al. Three-year Wilkinson Microwave Anisotropy Probe (WMAP) observations: Implications for cosmology. Submitted, 1965.

[40] S. T. Staggs et al. CMB radiation temperature at 10.7 GHz. *ApJL*, 473:L1, 1996.

[41] E. T. Swartz. Charcoal-pumped $^3$He cryostats for storage Dewars. *Rev. Sci. Instrum.*, 58:881, 1987.

[42] M. Tinkham. *Introduction to Superconductivity.* Dover Publications, 2004.

[43] J. N. Ullom et al. Characterization and reduction of unexplained noise in superconducting transition-edge sensors. *Appl. Phys. Lett*, 84:4206, 2004.